# Final Report

In Situ Thermal Remediation of DNAPL Source Zones

SERDP Project ER-1458

December 2011

Richard Johnson
Paul Tratnyek
Orgeon Health & Science University

Brent Sleep Magdalena Krol **University of Toronto** 

This document has been cleared for public release



maintaining the data needed, and c including suggestions for reducing	lection of information is estimated to ompleting and reviewing the collect this burden, to Washington Headqu uld be aware that notwithstanding an DMB control number.	ion of information. Send comment arters Services, Directorate for Info	s regarding this burden estimate ormation Operations and Reports	or any other aspect of the s, 1215 Jefferson Davis	his collection of information, Highway, Suite 1204, Arlington		
1. REPORT DATE DEC 2011  2. REPORT TYPE					3. DATES COVERED <b>00-00-2011 to 00-00-2011</b>		
4. TITLE AND SUBTITLE				5a. CONTRACT NUMBER			
In Situ Thermal Ro	emediation of DNAI	PL Source Zones	5b. GRANT NUMBER				
				5c. PROGRAM ELEMENT NUMBER			
6. AUTHOR(S)				5d. PROJECT NUMBER			
				5e. TASK NUMBER			
				5f. WORK UNIT NUMBER			
					8. PERFORMING ORGANIZATION REPORT NUMBER		
9. SPONSORING/MONITORING AGENCY NAME(S) AND ADDRESS(ES)				10. SPONSOR/MONITOR'S ACRONYM(S)			
			11. SPONSOR/MONITOR'S REPORT NUMBER(S)				
12. DISTRIBUTION/AVAIL Approved for publ	ABILITY STATEMENT ic release; distributi	on unlimited					
13. SUPPLEMENTARY NO	OTES						
14. ABSTRACT							
15. SUBJECT TERMS							
16. SECURITY CLASSIFICATION OF:			17. LIMITATION OF ABSTRACT	18. NUMBER OF PAGES	19a. NAME OF RESPONSIBLE PERSON		
a. REPORT <b>unclassified</b>	b. ABSTRACT <b>unclassified</b>	c. THIS PAGE <b>unclassified</b>	Same as Report (SAR)	155			

**Report Documentation Page** 

Form Approved OMB No. 0704-0188

# **Disclaimer**

This report was prepared under contract to the Department of Defense Strategic Environmental Research and Development Program (SERDP). The publication of this report does not indicate endorsement by the Department of Defense, nor should the contents be construed as reflecting the official policy or position of the Department of Defense. Reference herein to any specific commercial product, process, or service by trade name, trademark, manufacturer, or otherwise, does not constitute or imply its endorsement or recommendation by the Department of Defense.

# **Table of Contents**

SECTION 1. INTRODUCTION	1
1.1. PROJECT JUSTIFICATION AND SCOPE	1
1.2. PROJECT OBJECTIVES	2
1.3. TECHNICAL APPROACH	2
1.3.1. Groundwater Flow and Transport during Low-Temperature ERH (LTERH)	2
1.3.2. LTERH in Heterogeneous Media	2
1.3.3. Bubble Formation during Low-Temperature ERH	2
1.3.4. Heterogeneous Azeotropic Boiling	3
1.3.5. Thermal Effects on In Situ Chemical Oxidation	3
SECTION 2. BACKGROUND	5
2.1. INTRODUCTION	5
2.2. DNAPL SOURCE ZONES	5
2.3. CURRENT THERMAL REMEDIATION APPROACHES	6
2.3.1. Methods of Heat Delivery	7
2.4. LOW-TEMPERATURE ERH (LTERH)	9
2.5. COMBINED REMEDIES	10
2.5.1. Thermal/Physical	10
2.5.2. Thermal/Biological	11
2.5.3. Thermal/Chemical	11
2.6. SUMMARY	12
SECTION 3. MATERIALS AND METHODS	13
3.1. LOW TEMPERATURE ERH, SUBSURFACE FLOW AND TRANSPORT IN	
HOMOGENEOUS MEDIA	
3.1.1. Model Theory	
3.1.2. Materials and Methods	
3.1.3. Numerical Approach	
3.2. INFLUENCE OF SOIL HETEROGENEITY ON ENERGY AND MASS TRANSPORT	
3.2.1. Large Tank Experiments	
3.3. BUBBLE FORMATION DURING LOW-TEMPERATURE ERH	
3.3.1 Bubble Formation Mechanics	
3.3.2. 2-D Laboratory Physical Model Experiment to Examine the Effects of Bubble Formation during Low-Temperature ERH	on 33
uurne LOW-151110514tui5 LIXII	T 7

3.4. HETEROGENEOUS AZEOTROPIC BOILING DURING LOW-TEMPERATURE ERH	33
3.4.1. Theory	33
3.4.2. Materials and Methods	34
3.5. THERMAL EFFECTS ON IN SITU CHEMICAL OXIDATION	36
3.5.1. Background	37
3.5.2. Materials and Methods	42
SECTION 4. RESULTS AND DISCUSSION	44
4.1. LOW-TEMPERATURE ERH, SUBSURFACE FLOW AND TRANSPORT IN HOMOGENEOUS MEDIA.	44
4.1.1. Voltage and Power Measurements	44
4.1.2. Temperature	45
4.1.3. Tracer Study	46
4.2. HEAT AND MASS TRANSPORT IN HETEROGENEOUS MEDIA	48
4.2.1. Heating Up-Gradient of the Target Zone	48
4.2.2. Heating Beneath the Target Zone	50
4.2.3. Dissolution from a DNAPL Source while Heating Upstream	52
4.2.4. Numerical Modeling of Voltage and Power in the Heterogeneous Tank	54
4.2.5. Simulation of Heating, Flow and Transport in Heterogeneous Media	56
4.2.6. Parameters Used to Characterize Heat and Mass Transport	57
4.2.7. Simulation Description	60
4.3. BUBBLE FORMATION DURING LOW-TEMPERATURE ERH	68
4.3.1. 2-D Experiments with Heating and Bubble Formation	68
4.3.2. Tracer Test Following Heating and Bubble Formation	74
4.3.3. Numerical Modeling of Bubble Movement	77
4.4. HETEROGENEOUS AZEOTROPIC BOILING	88
4.4.1. 1-D Experiments	88
4.4.2. 2-D Experimental Results	91
4.5. THERMAL EFFECTS ON IN SITU CHEMICAL OXIDATION	93
4.5.1. PCE Dechlorination Kinetics with Persulfate.	93
4.5.2. Persistence of Persulfate under Thermal Activation Conditions	108
SECTION 5. CONCLUSIONS AND IMPLICATIONS	122
SECTION 6 REFERENCES	126
ADDENDIV A DEED DEVIEWED DIDLICATIONS EDOM THIS WODE	120

# TABLE OF FIGURES

# SECTION 2 FIGURES

Figure 2. 1. Schematic representations of A) a large DNAPL spill (after SERDP/ESTCP, 2001); B)
residual and pooled DNAPL and C) DNAPL pools and associated diffusion source zones 6
Figure 2. 2. Schematic drawing of an ERH application designed to produce boiling conditions
Figure 2. 3. Schematic drawing of an in situ thermal diffusion system and associated fluids treatment
system (from Johnson et al., 2009)
Figure 2. 4. Schematic drawing of an in situ steam-enhanced heating system and associated fluids
handling system. (from Johnson et al., 2009).
Figure 2. 5. Schematic drawing of a low-temperature ERH system
SECTION 3 FIGURES
Figure 3. 1. Photograph of the physical model used for visualization experiments. During operation the
aluminum frame is fully enclosed with optically-black covers. The syringe pump in the
foreground is used for tracer injection
Figure 3. 2. Schematic drawing of the 2D visualization tank. The green circles are thermocouple
locations, the blue squares are electrode locations, the red Xs are injection and extraction20
Figure 3. 3. Photograph showing detail of the visualization tank
Figure 3. 4. Photograph and schematic drawings of the large physical model. a) photograph of the
physical model; b) schematic drawing of the temperature monitoring point array; c) locations of
the electrodes used in the up-gradient (solid red circles) and beneath (open black circles)
experiments; and d) array of voltage measurement locations
Figure 3. 5. Photograph of the large model during filling and showing the thermocouple array used for
temperature measurements
Figure 3. 6. Solubilities of nitrogen and carbon dioxide (mole fraction) in water as a function of
temperature
*
Figure 3. 7. Water vapor pressure as a function of temperature
Figure 3. 8. Plot showing regions in which water saturated with gas at atmospheric pressure will produce
bubbles as a function of temperature and pressure.
Figure 3. 9. Fraction of pore space occupied by gas as a function of temperature for carbon dioxide and
nitrogen initially at saturation concentrations, 20°C and atmospheric pressure32
Figure 3. 10. Vapor pressures of carbon tetrachloride (CT), TCE and PCE as a function of temperature. 34
Figure 3. 11. Schematic representation of the experimental apparatus used for the heterogeneous
azeotropic boiling experiments35
SECTION 4 FIGURES
Figure 4. 1. Experimental and modeled power results for LTERH in the visualization model44

Figure 4. 2. Comparison of experimental and modeled temperature distributions in the visualization experiment. Red circles indicate electrode positions. a) experiment at 1.5 hours; b) model at 1.5
hours; c) experiment at 3 hours; and d) model at 3 hours
Figure 4. 3. Comparison between tracer tests in the visualization tank and corresponding model results. a) photograph of tracer tests ~1.5 hrs after startup; b) model results at 1.5 hrs; c) photograph at 3 hours; d) model results at 3 hours, all for the isothermal experiment. For the 50°C heating experiment: e) processed image at 1.5 hrs; f) model results at 1.5 hrs; g) processed image at 3 hrs; h) model results at 3 hrs
Figure 4. 4. a) Electrode locations (solid black circles) and measured voltages; b) measured temperatures
under steady-state conditions; and c) composite photograph showing snapshots of tracer plume movements for heating up-gradient of the treatment zone
Figure 4. 5. a) Electrode locations (solid black circles) and measured voltages; b) measured temperatures under steady-state conditions; and c) composite photograph showing snapshots of tracer plume movements for heating beneath the treatment zone
Figure 4. 6. Photograph showing the PCE DNAPL source zone created in the heterogeneous tank and used for the dissolution experiment. The blue rectangle represents the approximate location of the perforated portion of the injection tube
Figure 4. 7. Effluent concentration and temperature program for the TCE dissolution experiment 53 Figure 4. 8. Steady-state temperature profiles at 50 and 75°C during the TCE dissolution experiment.  The pink rectangle in each figure corresponds to the approximate location of the TCE source 54
Figure 4. 9. Voltage distribution in the large tank: a) initial experimental voltage; b) initial modeled voltage; c) final experimental voltage; d) final modeled voltage
Figure 4. 10. Power consumption during heating of the large physical model. Blue points represent measured values, red points represent modeled values
Figure 4. 11. Temperature contours (20-80°C, scale on right of figure) and energy parameters used to quantify the movement of energy
Figure 4. 12. Initial TCE aqueous concentration (mg/L) in a vertical slice of the subsurface. The red circles represent electrodes
Figure 4. 13. Estimate of variance for the center of energy of the Borden aquifer
Figure 4. 15. Simulated concentration contours for Borden aquifer for four different soil permeability realizations after 50 days of heating to 80°C. Red circles represent electrode locations
Figure 4. 16. Simulated concentration contours for Swiss aquifer for four different soil permeability realizations after 50 days of heating to 80°C. Red circles represent electrode locations
Figure 4. 17. Permeability contours and streamlines for Swiss aquifer a) before heating; b) after 10 days of heating
Figure 4. 18. Simulated DNAPL distribution in the Swiss aquifer from Dekker and Abriola (2000) 67
Figure 4. 19. Temperature profiles from the experiment measured at $\sim$ 3 minute intervals during heating. Blue represents a temperature of 20°C and red is 50°C.
Figure 4. 20. Correlation between measured luminosity and measured water content for the visualization tank
Figure 4. 21. Luminosity images converted from RGB images taken at times corresponding to the temperature snapshots in Figure 4.19.

Figure 4. 22. Percent water saturation as a function of time for the heating case with CO <sub>2</sub> -saturated water
Figure 4. 23. Plots of relative permeability as a function of water saturation for the Brooks-Corey and
vanGenuchten equations
Figure 4. 24. False color images showing the tracer distribution at ~20 minute intervals
Figure 4. 25. False-color images of tracer distribution for the "no-bubbles" case discussed in Section 4.1.
Figure 4. 26. Gas clusters before and after: a) expansion; b) mobilization; and c) fragmentation. Hatched squares represent gas-occupied grid blocks, while white squares are fully water-saturated blocks.  Adapted from Wagner et al., (1997)
Figure 4. 27. Initial aqueous concentration (mg/L) in a vertical slice of the subsurface; purple circles
represent electrodes locations 84
Figure 4. 28 Temperature distributions for #25 Ottawa sand after 30 minutes of heating. Temperature
distributions for the #50 and #75 sands were similar
Figure 4. 29. Calculated total vapor pressures for 1,1,1-TCA with (red line) and without (blue line) the contribution of water
Figure 4. 30. Simulated gas saturations for different sands at 70, 80 and 90°C after 9 minutes of heating.
87
Figure 4. 31. 1-D heterogeneous azeotropic boiling experiment with an emplaced source. The blue line
represents the temperature and the pink line is the percent mass recovered89
Figure 4. 32. 1-D heterogeneous azeotropic boiling experiment with well-mixed source
Figure 4. 33. 2-D Heterogeneous azeotropic boiling experiment with a DNAPL source
Figure 4. 34. Pseudo-first-order disappearance of PCE at five temperatures. Experimental conditions:
unbuffered, 4.5 x 10 <sup>-5</sup> M PCE, and 4.5 x 10 <sup>-4</sup> M Na <sub>2</sub> S <sub>2</sub> O <sub>8</sub> . Regression on pooled data for triplicate
experiments at each temperature. The control was done without persulfate94
Figure 4. 35. Concentration over extended time periods, showing non-pseudo first-order behavior at
longer experimental times. Experimental conditions: Unbuffered DI water, 70°C, 10:1 molar ratio
of $Na_2S_2O_8$ and chlorinated ethenes, concentration of PCE = 0.0014 M, concentration of the other
chlorinated ethenes = 0.002 M
Figure 4. 36. Arrhenius plots for the chlorinated ethenes. Experimental conditions: un-buffered, 10:1
molar ratio of $Na_2S_2O_8$ to chlorinated ethenes. Initial concentrations are given in the legend96
Figure 4. 37. Correlation between $lnA$ , $E_A$ , $k_{obs}$ , and $E_{HOMO}$ for oxidation of the chlorinated ethenes by
heat-activated persulfate. $R^2$ are given in each panel. $E_{HOMO}$ were calculated with MOPAC using
CAChe, as described previously (Waldemer & Tratnyek, 2006).
Figure 4. 38. Effect of bicarbonate on the oxidation of PCE by persulfate. Experimental conditions: 30°C.
$4.5 \times 10^{-5} \text{ M PCE}$ , $4.5 \times 10^{-4} \text{ M Na}_2\text{S}_2\text{O}_8$ . Replicate analyses are shown for each sample. The
control did not contain persulfate or bicarbonate
Figure 4. 39. Effect of bicarbonate concentration on $k_{\rm obs}$ for PCE oxidation by persulfate activated at three
temperatures. Conditions: 4.5 x 10 <sup>-5</sup> M PCE, 4.5 x 10 <sup>-4</sup> M Na <sub>2</sub> S <sub>2</sub> O <sub>8</sub>
Figure 4. 40. Arrhenius plots of the oxidation of PCE by persulfate in the presence of various
concentrations of bicarbonate. Experimental conditions: 4.5 x 10 <sup>-5</sup> M PCE, 4.5 x 10 <sup>-4</sup> M Na <sub>2</sub> S <sub>2</sub> O <sub>8</sub> .
The data for 0 mg/L bicarbonate are the same as the data in Figure 4.36 in the text. Values for the
data shown here are in Table 4.6.

Figure 4. 41. Comparison of three degradation processes for PCE as a function of temperature. The	
hydrolysis band was calculated using Arrhenius parameters obtained from Jeffers et al. (1989).	
The bottom of the permanganate (pink) band corresponds to 100 mg/L (0.63 mM) permanganate	e
and the top of this band corresponds to 40 000 mg/L (253 mM), calculated using Arrhenius	
parameters obtained from Huang et al. (2001). The persulfate band (light blue) corresponds to	
Arrhenius parameters obtained from experiments with 0.45 mM Na <sub>2</sub> S <sub>2</sub> O <sub>8</sub> /0.045 mM PCE. The	
data points correspond to experimental data for varying concentrations of $S_2O_8^{2-}$ while keeping	
	_
the PCE concentration at 0.045 mM. The three concentrations represented by the data points are	3
4.5 mM, 45 mM, and 450 mM $Na_2S_2O_8$ . The dashed line (blue) shows the rate of reaction with	
PCE at the upper limit of this $S_2O_8^{2-}$ concentration range data extrapolated to higher temperature	
assuming Arrhenius behavior.	
Figure 4. 42.Comparison of three degradation processes as a function of temperature for TCE, <i>cis</i> -DCE	
and trans-DCE.	
Figure 4. 43. Kinetics of persulfate disappearance in unuffered, deionized water at 70°C. Initial persulfation	ate
concentrations are given in the legend. The curves are from fitting the data to first-order	
disappearance kinetics	08
Figure 4. 44. Comparison of persulfate disappearance and sulfate appearance in un-buffered, deionized	
water at 70°C. Initial persulfate concentration = 2100 mg/L (10 mM)	09
Figure 4. 45. Normalized sulfate concentration as a function of time for a series of bicarbonate	
concentrations. Experimental conditions: 70°C and an initial 5 mM persulfate concentration. Th	ıe
measured initial and final pH are given in the inset	10
Figure 4. 46. Sulfate appearance (from persulfate decomposition) in un-buffered, deionized water (DIW	(
at 30, 50, and 70°C. Initial persulfate concentration = 5 mM. Soil concentration = 1 g/mL of	
water1	11
Figure 4. 47. Arrhenius plot for the thermal decomposition of persulfate. Open symbols are the first-order	er
rate constants $k_0$ and $k_1$ (left axis) and filled symbols are the second-order rate constants $k_2$ and $k_3$	<i>k</i> 3
(right axis). The constants $k_0$ , $k_1$ , $k_2$ , and $k_3$ refer to the undifferentiated, neutral-, acid-, and base	<u>-</u>
initiated pathways, respectively. Squares are media other than deionized water (DIW) and	
buffered DIW. Lines are the results of fitting performed here on combinations of new and	
previously published data. The new data shown (black, labeled This Work) correspond to	
experiments shown in Figure 4.46.	12
Figure 4. 48.Calculated kinetics of persulfate decay in deionized water as a function of pH and	
temperature	14
Figure 4. 49. Persulfate disappearance in batch re-spike experiments at 70°C with soil concentration =	- '
0.67 g/ mL. Initial persulfate concentrations (mM) as labeled. Experimental data are shown as	
circles. Solid blue line represents simulation of the process using a combination of persulfate	
thermolysis and a second-order reaction between persulfate and the soil oxidant demand. The	
dashed line represents the modeled decay using only the thermolysis reaction and the dotted line	_
represents persulfate decay using only the second-order reaction.	
Figure 4. 50. Pseudo first-order disappearance rate constants ( $k_{\text{obs}}$ ) for persulfate in respike experiments	
(from fitting the experimental data shown in Figure 4.49). All data for batch experiments done a	aτ
$70^{\circ}$ C and soil concentration = 0.67 g/mL. Initial persulfate concentrations are given in the	10
legend1	18

Figure 4. 51. Calculated steady-state diffusion profiles for persulfate in saturated soil without soil oxidant demand. Inset: calculated persulfate concentration profiles vs. time after injection of persulfate stopped
LIST OF TABLES
SECTION 3 TABLES
Table 3. 1. Properties of the 2D Visualization and simulation parameters (sources: <sup>a</sup> Gori et al., 2001; <sup>b</sup> Lide, 2006; <sup>c</sup> Michaeli, 2003)
Table 3. 2. Measured concentrations of dissolved gas (cm3 per gram of water) from the California Ground-Water Ambient Monitoring and Assessment (GAMA) program (Kulongoski et al., 2006).
Table 3. 3. Antoine equation parameters for carbon tetrachloride, TCE and PCE (Yaws & H. Yang, 1989)
SECTION 4 TABLES
Table 4. 1. Aquifer properties and simulation parameters
Table 4. 2. Bubble formation simulation scenarios. (Source - Kueper, 1990)
Table 4. 3. System initial conditions and 1,1,1-TCA properties. Sources: <sup>a</sup> Markle et al., 2006; <sup>b</sup> Pankow & Johnson, 1996; <sup>c</sup> Lide, 2006; <sup>d</sup> Mumford et al., 2010
Table 4. 4. $k_{obs}$ and corresponding activation parameters for all 4 chlorinated ethenes
Table 4. 5. Arrhenius parameters for chlorinated ethenes
Table 4. 6. $k_{obs}$ and corresponding activation parameters for PCE with different concentrations of
bicarbonate
Table 4. 7. Kinetic parameters, diffusion coefficients and times to steady state diffusion profiles (days).
SECTION 5 TABLES
Table 5.1. Summary of opportunities and concerns regarding the coupling of LTERH with other in situ remediation processes

# **Acronyms and Abbreviations**

aq aqueous

ASTM American Society for Testing and Materials

Bgs below ground surface

Bo Bond number
BP boiling point
°C Celsius degrees

CHC chlorinated hydrocarbon CT carbon tetrachloride cis-DCE cis-1,2-dichlororethene trans-DCE trans-1,2-dichloroethene

DNAPL dense non-aqueous phase liquid

DoD Department of Defense ERH electrical resistance heating ETM electro-thermal model

GAMA Ground-Water Ambient Monitoring and Assessment (A California Program)

H hour

HOMO highest occupied molecular orbital

ISCO *in-situ* chemical oxidation ISCR *in-situ* chemical reduction

kg kilogram

mL

LTERH Low-temperature electrical resistance heating

mg milligrams

MIP macroscopic invasion percolation

mm millimeter
O.D. outside diameter
PCE tetrachloroethene
ppb parts per billion

ppm parts per million ppmV parts per million, volume basis

milliliter

r radius s second

SERDP Strategic Environmental Research Development Program

TCA trichloroethane TCE trichloroethene

USACE U.S. Army Corps of Engineers

USEPA U.S. Environmental Protection Agency

USGS U.S. Geological Survey

VC vinyl chloride

VOC volatile organic compound

**Symbols** 

A pre-exponential factor in Arrhenius equation

 $\alpha$  pressure coefficient

 $\beta$  viscosity temperature dependence parameter

c heat capacity C concentration

D diffusion coefficient

*E* energy

*E*<sub>A</sub> activation energy

g acceleration due to gravity

*h* hydraulic head

H dimensionless Henry's Law constant

*I* ionic strength

 $I_{\rm z}^e$  second moment of energy

k reaction rate constant or intrinsic permeability

 $k_{obs}$  observed reaction rate constant  $K_d$  soil-water distribution coefficient

 $K_H$  thermal conductivity

 $K_x$  hydraulic conductivity in x direction

J flux

L luminance

 $L_x$  simulation depth in x direction

M mass or metal

n porosity ( $\phi$  also used)  $\mu$  micro or viscosity

 $\Omega$  ohms P pressure

 $\phi$  phase angle or soil porosity

 $q_{in}$  groundwater flux R ideal gas law constant

 $\sigma$  density or electrical conductivity Q sinks or sources of electric charge

S saturation or solubility

t time

 $t_{1/2}$  reaction half-life T temperature

au viscosity temperature dependence parameter

U heat loss term

V voltage

 $\omega$  angular frequency

z elevation

# **Keywords**

Chlorinated solvent
Chlorinated hydrocarbon
DNAPL
Groundwater
In situ thermal
Remediation
Source zone

# Acknowledgements

The research described in this final report was supported by the U.S. Department of Defense through the Strategic Environmental Research and Development Program (SERDP). We wish to thank Dr. Andrea Leeson and the SERDP staff for their administrative assistance and support of the project.

A thermal remediation expert panel, assembled by SERDP, provided valuable insight and technical guidance during the course of the project. The expert panel consisted of the following members:

Dr. Michael Basel (Haley and Aldrich, Inc.)

Dr. Paul C. Johnson (Arizona State University)

Mr. Michael Marley (Xpert Design & Diagnostics LLC)

Dr. Paul D. Lundegard (UNOCAL)

Dr. Hans Stroo (HGL, Inc.)

This project benefited from interactions with investigators from two other SERDP projects that focused on thermal remediation: ER-1419 Investigation of Chemical Reactivity, Mass Recovery and Biological Activity During Thermal Treatment of DNAPL Source Zones (Dr. Kurt Pennell, PI) and ER-1423 Large-Scale Physical Models of Thermal Remediation of DNAPL Source Zones in Aquifers (Dr. Ralph Baker, PI).

# **Executive Summary**

**Objectives:** The objective of this project has been to examine how low-temperature electrical resistance heating (LTERH) can be used to enhance sub-surface remediation. In some cases the experiments conducted here were designed to evaluate processes that were enhanced directly as the result of heating (e.g., boiling). In others, heating was used as part of a "combined remedy" to facilitate some other process (e.g., chemical reaction).

**Technical Approach**: This report describes a series of laboratory experiments and numerical modeling activities designed to improve our understanding of the processes controlling heat and mass transport associated with the subsurface application of LTERH.

**Results:** Taken together, the results of this work indicate that that LTERH has significant potential to improve remediation of DNAPL source zones, especially those for which advective groundwater flow is limited. This is particularly the case for pools of DNAPL, which frequently occur at the tops of low-permeability media and which occur in topographic low points on those layers. Mass transfer is also limited in "diffusion zones" which were produced within low-permeability layers as the result of long-term contact with high-concentration sources (e.g., DNAPL pools). The ability to improve treatment in these zones is important because DNAPL source zones continue to control the timelines for site remediation and many Department of Defense sites.

**Benefits:** The experiments and modeling demonstrate several beneficial strategies that may prove useful in regard to source zone treatment, and four of them are briefly summarized here:

• LTERH can increase local groundwater flow and, in particular, can substantially increase buoyancy-driven vertical flow

Taking advantage of buoyant flow is of particular importance in heterogeneous systems containing both high and low-permeability zones. Our results indicate that vertical flow across high/low hydraulic conductivity interfaces can be dramatically increase by heating to temperatures well below the boiling point of water. This can result in order-of-magnitude increases in mass transfer out of the source zone and into zones where groundwater flow rates are much higher.

 Targeted heating to azeotropic boiling temperatures can dramatically increase vertical migration into zones of increased groundwater flow without causing off-gas collection issues.

The ability to deliver heat at specific depths and, in particular, to deliver heat preferentially to lower-permeability zones (because they typically have higher electrical conductivity and because advective flow does not carry heat away from those zones) allows diffusion sources and DNAPL pools to be targeted. The table below lists azeotrope temperatures for a number of chlorinated hydrocarbon solvents (Gmehling et al., 1977) that have historically been used as solvents and which frequently appear as groundwater contaminants.

Compound	Boiling Point (°C)	Azeotrope with Water (°C)
tetrachloroethene	121	88
trichloroethene	87	73
1,1,2-trichloroethane	114	86
carbon tetrachloride	77	67
chloroform	61	56
methylene chloride	40	39

# • LTERH can be used to optimize naturally-occurring processes (e.g., bioremediation, dissolution)

Because ERH can be used to produce temperatures anywhere from ambient to  $\sim 100^{\circ}$ C (unlike thermal diffusion and steam that rely on heat sources at  $> 100^{\circ}$ C), LTERH systems can be controlled to optimize a range of processes. At the same time, the lower temperatures reduce infrastructure and energy requirements, and as a result, the operation and maintenance costs for these systems can be very low.

However, particularly in the context of reductive dechlorination, it may be very difficult to find an elevated temperature that facilitates the complete dechlorination of CHCs to ethene. This is the case because the final, critical dechlorination step (vinyl chloride to ethene) is inhibited or eliminated at temperatures above  $\sim 35^{\circ}$ C (Lebron et al., 2011), and it will likely be difficult to heat source areas without exceeding that temperature, at least within portions of the source. Because vinyl chloride is an important contaminant, this can exacerbate the groundwater contamination problem.

# • Delivery of chemical oxidants/reductants to diffusion-limited source zones can be optimized by targeted LTERH

Diffusion-limited source zones typically require long remediation time frames because, by their nature, times required for diffusion of contaminants out of the source will be at least as long as they have existed as sources. For scenarios in which those timeframes are too long, it is possible to deliver reactants into the source by diffusion in order to degrade contaminants while they are still inside the source. Of course, delivery of reactants will also be controlled by diffusion. Here we examined the potential for a thermally-activated reactant (persulfate) to be delivered to a source zone at a temperature that maximized the depth to which the reactant would be effective. In practice, the optimization process is straightforward, because both the reaction rate and the diffusion process can be accurately modeled. One complicating factor in this regard is the consumption of reactant by the aquifer materials. However, as described in Section 4.5, our data suggest that laboratory experiments can be used to understand this process.

None of these strategies comes without complicating factors. Increased subsurface temperatures can lead to increased mobility of DNAPL. This has been observed in numerous physical model experiments, including the ones reported here. However, since most of the

applications discussed here involve subsurface temperatures that are well below 100°C, the problem is expected to be less severe than for higher-temperature thermal applications. The same may not be true for bubble formation and reduction in water permeability. This process can be predicted, at least in a conceptual sense, but additional work on this topic should be an important future research activity.

In an effort to place all of the processes discussed here into a context in which they are comparable, the table below outlines the temperature ranges over which each process is potentially relevant from a subsurface source zone remediation context. While numerous other processes could be included in the table (e.g., additional chemical oxidants and reductants), the table does suggest how subsurface heating might be used in conjunction with other activities to produce more-effective combined remedies.

TEMPERATURE	BIODEGRADATION	BUBBLE FORMATION	BUOYANCY EFFECTS	HETEROAZEOTROPIC BOILING	IN SITU CHEMICAL OXIDATION
(°C)	BIODEGRADATION	BUBBLE FURIVIATION	BOOTAINCT EFFECTS	PCE AND 1,1,2-TCA AZEOTROPES	OXIDATION
85				AZEOTROPES	
80		BUBBLE FORMATION LIKELY	BUOYANCY EFFECTS LIKELY	TCE AZEOTROPE	
75		OVER THIS RANGE	OVER THIS RANGE	CARBON TETRACHLORIDE	
70				AZEOTROPE	
65				CHLOROFORM AZEOTROPE	
60					
55					
50					
45				METHYLENE CHLORIDE AZEOTROPE	
40					RANGE FOR OPTIMUM REACTION AND
35	UPPER LIMIT FOR VINYL CHLORIDE				PERSISTENCE FOR PERSULFATE
30	DECHLORINATION (Lebron et al., 2011)				
25	, , , , , , , , , , , , , , , , , , , ,				
20					
15					
10					

All of the combined remedies listed in the table above have aspects that make them somewhat complicated to implement. These may include, for example, the need for an accurate conceptual model of aquifer structure and the location(s) of DNAPL sources. The most important of these factors are briefly outlined in the following table.

Process/ Bottom Line	Comments on Process	Lab Test/ Modeling/ Data	Comments on Lab Testing, Modeling and Data
Azeotropic boiling  Bottom Line: Mass removal of DNAPLs with low-boiling azeotropes (e.g., <70oC) can be significantly enhanced with LTERH.	Literature values can be used to determine if azeotropic boiling is practical. In general, if the azeotrope temperature is >85°C, it will be difficult to constrain the boiling zone to where the DNAPL is present. In addition, increasing temperature typically leads to decreased DNAPL viscosity, which can facilitate unintended migration of the DNAPL. So, these concerns should be evaluated based on the amount and distribution of the DNAPL present at the site and the site stratigraphy.	Modeling the heating process; Development of an accurate site conceptual model.	Vapor movement is very complicated to model but it should be possible to estimate the maximum extent of vapor movement based on temperature measurement and modeling. An accurate conceptual model of the site will be important for successful application of azeotropic boiling without an off-gas collection system.
Dissolution  Bottom Line: Generally has a minor effect.	Increases in solubility due to heating are generally not large (e.g., <2X). In this context, increased dissolution may come mostly from increased flow due to density and viscosity changes in the water.	Literature data on solubility.	Data are available for solubility as a function of temperature and, as a result, laboratory measurements are generally not required. The greatest uncertainty in the context of dissolution is the degree of contact between the flowing water and DNAPL. As a first approximation, however, it can be assumed that dissolved concentrations will increase in proportion to the increase in solubility.
Biodegradation  Bottom Line: Generally limited to <35oC. Difficult to implement with LTERH.	Biodegradation can increase rapidly when temperatures are raised from 10 to ~35°C. However, beyond this range biodegradation rates frequently drop rapidly. As a consequence, using LTERH to increase biodegradation rates will, in general, be more difficult than for abiotic reactions. Alternate heating approaches (e.g., hot water injection) may be better suited to thermal enhancement of biodegradation.		Difficult to implement with LTERH.

		Lab Test/ Modeling/	Comments on Lab Testing,
Process	Comments on Process	Data	Modeling and Data
Enhanced flow	Water viscosity and density decrease significantly with heating. As a consequence, heating localized around a source zone can	Modeling of heating and groundwater flow; Estimation of the role of entrapped vapor	Modeling of enhanced flow during heating can be successfully modeled with SEAWAT. Successful modeling will depend on accurate information on
<b>Bottom Line: Heating</b>	significantly increase local flow within the higher-		both the hydraulic conductivity structure of the
can enhance dissolution	permeability portions of the source. However, if		aquifer and the distribution of the DNAPL. In
from DNAPL pools. Not	diffusion-limited zones represent an important		some media, bubble formation can inhibit water
beneficial for diffusion	component of the source, the effects of		flow (e.g., when stratification entraps significant
sources.	increased temperature on flow may be minimal. (In addition, while diffusion coefficients increase with increasing temperature, those increases are also generally small).		volumes of vapor) and this can have an inhibitory effect on water flow. An accurate conceptual model for the site is important in this context.
In situ chemical	For many chemical reactions, including those	Laboratory reactant demand	Aquifer solids can vary significantly in their ability
reaction	commonly used for in situ remediation, reaction rates double with every 10°C increase in temperature. Unlike biodegradation, however,	measurements	to consume injected reactants. In addition, depending on the reactant, the rate at which the reactant is consumed can vary significantly with
<b>Bottom Line: Heating</b>	rates continue to increase even as boiling		temperature. As a consequence, laboratory
enhances rates but can	temperatures are approached. However, this		testing of reactant demand for the solids/reactant
shorten reactant lifetime.	increase in reaction rate may be accompanied by a decrease in reactant lifetime, which may limit its delivery in the subsurface.		combination is recommended. This is discussed in Section 4 of this report.

### **SECTION 1. INTRODUCTION**

### 1.1. PROJECT JUSTIFICATION AND SCOPE

Groundwater contamination from chlorinated hydrocarbon (CHC) solvents released into the subsurface continues to be a persistent environmental problem at many DoD sites. This is due in part to their wide-spread historical usage. However, it is also due to the physical and chemical characteristics of those solvents.

Chlorinated solvents are sparingly soluble in water, which means they can exist in the subsurface as a separate organic phase. (At the same time, the regulatory concentration limit for many of the chlorinated solvents is very low, meaning they must be addressed). That separate organic phase is more-dense than water, so most chlorinated solvents can be described as dense, non-aqueous-phase liquids (DNAPLs). The chlorinated solvents, as a group, are relatively resistant to biodegradation, and even when biodegradation does occur, the daughter products produced are also regulated as contaminants.

Over the last two decades a great deal has been learned about the behavior of chlorinated solvents in the subsurface. This is particularly the case with regard to "source zones" for those solvents. In this context, source zones are defined as regions of the subsurface where a DNAPL phase is or was present (National Research Council, 2005; Stroo et al., 2003). DNAPL sources can be further divided into residual zones and pools. Residual zones are produced when DNAPL moves down through a medium and leaves behind entrapped ganglia of DNAPL trapped as isolated "droplets" within pores. If the DNAPL reaches a layer through which it cannot penetrate, it can form a pool on top of that layer. Those pools are often located within "topographic low points" on that layer. As a consequence, they may have limited contact with flowing groundwater. Under normal groundwater flow conditions, transport into that zone is by molecular diffusion, and as a result, the pools in particular can be very long lived.

Part of the challenge of remediating chlorinated solvent sites is that few remediation technologies are well suited for addressing DNAPL pools. Of the available techniques, thermal approaches are probably the best because they do not rely on aqueous molecular diffusion, but rather can benefit from thermal diffusion as well as gas-phase flow brought about by volatilization of the water and the solvent. Both thermal diffusion and gas-phase flow are orders of magnitude more rapid than diffusion. "Traditional" thermal methods (e.g., heating to boiling temperatures with resistance heating, thermal diffusion and/or steam) remove contaminants by volatilization and steam distillation. However, this approach requires extensive infrastructure because of geotechnical concerns and the need to manage multiple fluid streams (vapor, water and potentially DNAPL)

In the low-temperature approach examined here, remediation infrastructure can be significantly reduced because heating is targeted at smaller zones with temperature kept below the boiling point of water. As a result, if desired, remediation operation can proceed without any fluids removal. The focus here is on electrical resistance heating (ERH) because it is one of the

few available technologies that can heat the subsurface without local boiling and without injection of fluids (i.e., other heating approaches involve boiling temperatures – thermal conduction heating and steam injection – or injection of hot water). As a consequence, the approach presented here both fills a unique niche and couples well with other remediation techniques (including in situ chemical and biological processes).

### 1.2. PROJECT OBJECTIVES

The primary objective of this project was to provide a comprehensive understanding of the processes that control fluid flow and mass transport during heating, including: 1) changes in groundwater flow due to buoyancy and viscosity changes of the water; 2) the interaction between heating and aquifer heterogeneity; 3) bubble formation; 4) heterogeneous (i.e., multi-phase) boiling; 5) the effect of heating on in situ chemical reactions.

#### 1.3. TECHNICAL APPROACH

# 1.3.1. Groundwater Flow and Transport during Low-Temperature ERH (LTERH)

Both physical model (i.e., "tank") experiments and numerical modeling studies were undertaken to examine the effects of localized heating on subsurface flow. The physical model experiments combined detailed temperature measurements and observation of tracer movement to understand how changes in density and viscosity of heated water affected flow. The physical model results were used to "calibrate" the coupled ERH/flow/transport numerical model that was developed as part of this project. The calibrated model was then used to examine a range of scenarios that could not be represented in the physical models.

### 1.3.2. LTERH in Heterogeneous Media

Two types of scenarios were examined. First a series of laboratory experiments were conducted in a layered system consisting of a low-k layer beneath a sand layer. Power consumption, voltage distributions and tracer movement were all recorded and again used to evaluate the coupled numerical model. Second, a suite of spatially-correlated random permeability fields were generated to assess how heterogeneity would affect ERH performance. The generated permeability fields were designed to represent two well-known field scenarios – CFB Borden (Woodbury & Sudicky, 1991) and Swiss sand and gravel system (Jussel et al., 1994)

### 1.3.3. Bubble Formation during Low-Temperature ERH

Bubble formation in the subsurface occurs when the sum of the vapor pressures of all volatile constituents reaches the in situ pressure. In the context of chlorinated solvent sites there are potentially three important groups of volatile constituents: the contaminant, dissolved gases, and water. Each of those can be of importance over different subsurface temperature ranges. For example, since many groundwaters are essentially saturated with nitrogen, and may have significant quantities of dissolved CO2 and CH4, and since solubilities of those gases decrease with increasing temperature, it frequently does not take much heating to exolve bubbles. For chlorinated solvents that boil below the boiling point of water (e.g., TCE, 1,1,1-trichloroethane (TCA), carbon tetrachloride(CT)), at high concentrations bubble formation can occur well below  $100^{\circ}$ C.

For dissolved constituents like atmospheric gases and contaminants, once bubble formation occurs most of the mass may distribute to the bubbles, and the lower dissolved concentration will lead to cessation of bubble formation. As a consequence, a relatively static condition can result in which bubbles persist but no new ones are formed. If the quantity of bubbles formed is sufficient to significantly reduce the water permeability of the medium, then water flow may slow to a stop in that area. Continued heating of that zone could lead to sustained bubble formation (i.e., boiling) and significantly-increased mass removal. As this description indicates, the choice of temperature can have a significant effect on groundwater flow and mass removal.

To evaluate this, 2-D experiments were conducted to visualize the bubble formation process. Those experiments were also used to directly observe the effects of bubble formation on groundwater flow. Numerical simulation of these experiments proved difficult, in part because the relationship between gas saturation and relative permeability is not well characterized for this system. As a consequence, in its current form, the model allows simulation of bubble formation from a single dissolved species and does not take into account the effect of bubble formation on water movement.

# 1.3.4. Heterogeneous Azeotropic Boiling

A series of 1-D and 2-D experiments were conducted to evaluate the relationship between temperature and volatilization. Primary issues here are: 1) can complete removal of DNAPL be accomplished at the azeotropic boiling point; and 2) if not, what temperatures are necessary for complete DNAPL removal.

### 1.3.5. Thermal Effects on In Situ Chemical Oxidation

Abiotic chemical reaction rates typically increase substantially with increasing temperature in a predictable fashion (e.g., following the Arrhenius equation). At the same time,

transport of the chemical oxidants, especially via diffusion into lower-permeability areas, is much less dependent on temperature. As a consequence, it is important to understand the balance between these two processes in order to maximize the efficient use of the oxidant. To examine this, a series of laboratory batch experiments was conducted using sodium persulfate to examine: 1) the rates of reaction with chlorinated solvents; and 2) the lifetime of the oxidant as a function of temperature. Those data were used with a numerical diffusion model to evaluate the relationship between temperature and the depth into a low-permeability layer to which oxidation can be effective.

# **SECTION 2. BACKGROUND**

#### 2.1. INTRODUCTION

The challenges posed during remediation of chlorinated solvent DNAPL sources have been widely addressed for more than two decades. Nevertheless, CHC contamination persists as one of the most problematic aspects for management of many contaminated DoD and other sites. Current remediation strategies for DNAPL sites tend to fall into three categories: 1) aggressive treatment (e.g., high-temperature heating); 2) maintenance (e.g., pump-and-treat) and 3) natural attenuation (e.g., microbiological). However, many sites fall into a fourth category – one in which the timeframe for cleanup is shorter than can be afforded by maintenance or natural attenuation, but for which high-temperature treatment is not warranted or feasible.

Currently, this fourth category is being addressed by a range of techniques, including air stripping, in situ chemical oxidation (or reduction) and enhanced bioremediation. However, these approaches are proving ineffective at many sites. In that context, "combined remedies" are increasingly being discussed as the preferred strategy. In many of those cases, increased subsurface temperatures can be a key element.

### 2.2. DNAPL SOURCE ZONES

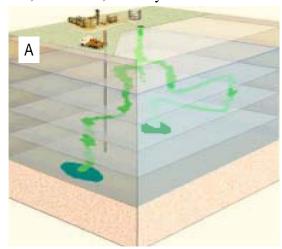
For many DNAPL releases, much of the mass is/was often associated with low-lying pools on top of low-permeability layers (Figure 2.1A, SERDP/ESTCP, 2001). Initially, groundwater will flow both through residual DNAPL zones and over the DNAPL pools (Figure 2.1B). However, the lifetime of the residual DNAPL is expected to only be a few years to perhaps a decade (Anderson, R. L. Johnson, & J. F. Pankow, 1992) and, as a result, for most large historical releases, if DNAPL persists it is likely that much of it will be in low-lying pools. As Figure 2.1C indicates, those pools can be associated with topographic low points in the surfaces of low-permeability layers, and as a result, they may present a very low profile to the flowing groundwater. Under those circumstances, dissolution will be controlled by molecular diffusion out of the pools, and the lifetimes of the pools can be very long (e.g., decades to centuries (Johnson & Pankow, 1992)). At the same time, diffusion from the DNAPL into the underlying clay can produce a "diffusion source" zone that can act as a long-term source even after the DNAPL pool is gone. As a result, both the DNAPL pools and the diffusion sources represent important targets for in situ treatment by chemical and/or enhanced biological processes.

To facilitate in situ treatment of DNAPL pool and diffusion sources, it is typically important to deliver reactants directly to those sources. However, as discussed above, contact between flowing groundwater and the DNAPL pools and diffusion sources associated with low-permeability layers is minimal due to their geometries and, as a result, delivery of reactant

solutions is typically very inefficient. (It is also possible that DNAPL could have entered the underlying low-permeability layer via cracks and other flow paths, and subsequently dissolved and diffused into the clay matrix. Reactant delivery in this case will be extremely difficult, and treatment of this mass will likely only occur as the result of diffusion.) As a consequence, it is not realistic to expect delivery of reactants to destroy all contaminants present in diffusion sources. However, using the approach described here, it may be possible to reduce the flux of those contaminants to the point that other processes will maintain groundwater concentrations below regulatory thresholds.

# 2.3. CURRENT THERMAL REMEDIATION APPROACHES

The current applications of in situ thermal remediation (ISTR) almost always involve heating to 100°C or above. Johnson et al. (2009) have recently summarized the state of the practice in an ESTCP report that provides an excellent summary of ISTR using thermal diffusion (TD), steam and electrical resistance heating (ERH). Their report indicates that, since 2000, nearly 60% of reported thermal remediation activities involved ERH, with the remaining 40% split between thermal conduction and some form of steam injection. (Total number of reported applications was 84). Essentially all of these have target temperatures of ~100°C and focused on the removal of multiple fluid phases. In addition, most were focused on physical removal



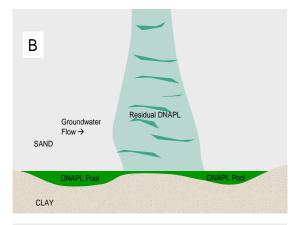




Figure 2. 1. Schematic representations of A) a large DNAPL spill (after SERDP/ESTCP, 2001); B) residual and pooled DNAPL and C) DNAPL pools and associated diffusion source zones.

(i.e., volatilization and steam distillation) rather than chemical or biological degradation.

# 2.3.1. Methods of Heat Delivery

The three methods of delivering heat to the subsurface will be summarized very briefly here. The primarily focus of this discussion will be on their applicability for treatment of DNAPL pools.

# 2.3.1.1. Electrical resistance heating

Figure 2.2 shows a conceptual representation of an ERH system. Typically, power can be provided by a conventional 440-480 volt, 3-phase connection (red lines on the figure). Each "leg" of the three phases is then delivered to an individual electrode, with the electrodes configured in a triagonal pattern.

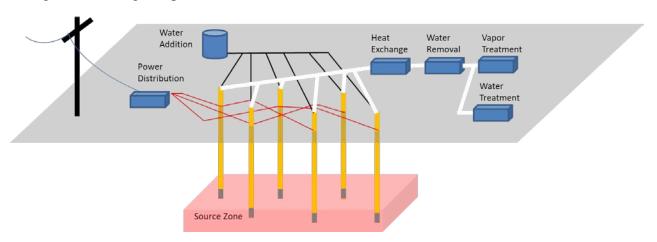


Figure 2. 2. Schematic drawing of an ERH application designed to produce boiling conditions

During ERH, heating and fluids recovery can be accomplished in the same borehole (white lines). In some cases, water may need to be added at the electrodes to prevent drying and loss of electrical conductivity (black lines). Temperature control is provided by the power applied to the electrodes, and can be actively monitored and controlled Power densities are greatest in the vicinity of the electrodes and, as a consequence, boiling occurs in that area and may need to be managed by the addition of water down the electrode/borehole.

The rate at which fluids (water, vapor NAPL) come from the extraction wells can vary significantly over the course of heating, and as a consequence the capacity of the treatment system must be sufficiently large.

For most geologic systems, electrical conductivity increases with decreasing hydraulic conductivity due the presence of more-conductive, fine-grained materials (e.g., clays). As a consequence, ERH can to some extent be targeted at low-permeability layers. This can

potentially facilitate heating of DNAPL pools located on top and/or within those zones. The combination of targeted heating and the ability to control temperature at below the boiling point of water make ERH the most flexible of the heating approaches discussed here.

# 2.3.1.2. Thermal diffusion

Thermal diffusion (aka thermal conduction) can utilize an array of wells similar to ERH in which heating and extraction can both be accomplished (Figure 2.3). In this case, however, heating takes place at an electrical element within the well and, as a result, the temperature of the well will be well above the boiling point of water (i.e., to maximize thermal diffusion away from the well). The treatment system for the extracted fluids will, in general, be similar both in size and function to the ERH system.

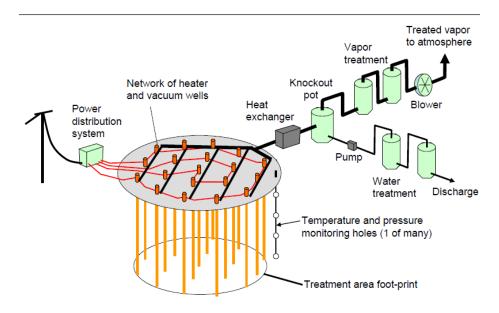


Figure 2. 3. Schematic drawing of an in situ thermal diffusion system and associated fluids treatment system (from Johnson et al., 2009)

Due to the high temperatures at the heater wells, coupling TD with other aqueous-based approaches can be problematic. However, TD does have an advantage over ERH in that it does not need water movement to deliver the heat. As a consequence, it can also be applied to unsaturated soils more easily than ERH.

# 2.3.1.3. Steam injection

As with TD, steam injection operates at or above 100°C. In principle, it can be applied either above or below the water table. Extraction treatment system required for steam injection is similar to those for TD and ERH (Figure 2.4). However, below the water table steam can show strong buoyancy behavior. In addition, movement of the steam will be highly controlled by variations in hydraulic conductivity in the medium. So, unlike TD and ERH, fluid (and heat)

delivery may limit applicability of the approach for treating DNAPL pools and low-permeability source zones.

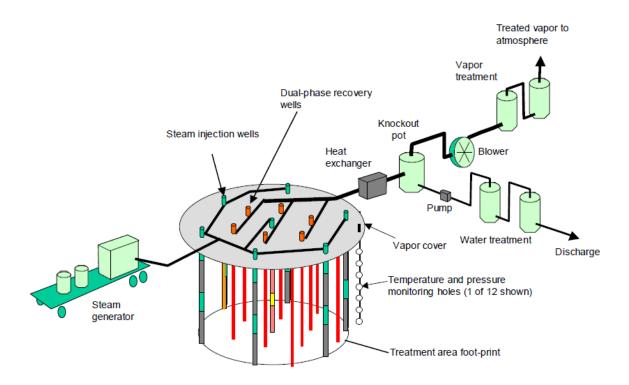


Figure 2. 4. Schematic drawing of an in situ steam-enhanced heating system and associated fluids handling system. (from Johnson et al., 2009).

# 2.4. LOW-TEMPERATURE ERH (LTERH)

Because ERH is currently the most-commonly-used heating approach for subsurface remediation, because it can be managed at sub-boiling temperatures, and since the focus here is primarily on DNAPL source zones below the water table, it was selected for the work discussed below. There are a number of important reasons why thermal operation below boiling can be important in the DNAPL source zone context. These can include: a) geotechnical concerns; b) optimization of coupled in situ processes; c) minimization of power requirements; and d) elimination of fluids recovery and treatment systems.

In the context of the schematic drawings above, a sketch of the simplified operational system for an LTERH system is shown in Figure 2.5. Because temperature are kept below boiling, extraction wells may not be necessary and an above-ground fluids treatment system may not be needed. (As with the other electrical heating systems, the electrode/heaters can also serve as injection/extraction as needed). The much-smaller power requirements for LTERH means

that smaller-diameter electrodes, which may be amenable to direct push installation, could be used. In addition, because at lower temperatures physical containment of DNAPLs is of less concern, targeted heating will be practical in many cases.

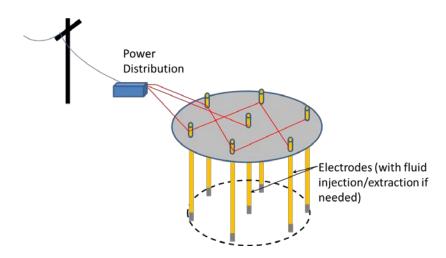


Figure 2. 5. Schematic drawing of a low-temperature ERH system.

# 2.5. COMBINED REMEDIES

In principle, thermal approaches can be combined with a variety of other remediation techniques (e.g., biological, chemical and/or physical) to yield improved performance.

# 2.5.1. Thermal/Physical

Combined thermal and physical approaches have historically been the most common. For example, "traditional" thermal approaches frequently must combine heating and vapor/liquid recovery to ensure contaminant containment. Combinations including steam and electrical resistance heating have also been employed (Heron, Carroll, & Nielsen, 2005). In addition to production of a vapor phase, enhanced dissolution due to increased groundwater flow velocity, increased solubility and buoyant flow area also possible.

# 2.5.2. Thermal/Biological

Most field investigations of the effects of heat on biological reactions have involved examination of microbial populations following the application of high-temperature thermal applications. For example, Richardson et al. (2002) examined both laboratory and field soils following extended steam treatment. They concluded that post-treatment activity was similar to pre-treatment activity for a range of bacteria and archaea. Friis et al. (2007) conducted laboratory studies to look at dechlorination after heating soils to 100°C and allowing them to cool slowly. Following temperature cycling they observed no vinyl chloride degradation, even when the system was amended with lactate. They also did not observe any Dehalococcoides (*Dhc*) activity following heating, even though *Dhc* had been present and active in the samples prior to heating. Similarly, Fletcher et al. (2011) reported that vinyl chloride-degrading cultures lost the ability to degrade VC when heated to temperatures of 35°C or higher. They also reported that heating the cells to >45°C resulted in permanent loss of the ability to convert VC to ethane. These data suggest improving microbial dechlorination activities with modest heating (such as might be accomplished by ERH) may be challenging – especially for the all-important vinyl chloride to ethene step.

# 2.5.3. Thermal/Chemical

Since abiotic reactions typically follow Arrhenius-type behavior, with increasing reaction rates for increasing temperatures, it would be expected that combined thermal/chemical reactions would easier to manage from a heating perspective. Pennell et al. (2009) examined the effects of temperature on reaction rates for a wide range of conditions. They concluded that, for most soils, simply heating the soil would not result in degradation rates of TCE or PCE that were sufficiently fast to be useful in a remediation context. They also examined the effects of heat combined with the addition of in situ chemical reactants, and concluded that chemical addition probably represented the best approach to increased degradation rates with modest heating. However, this approach necessitates the delivery of reactants in the subsurface which, depending upon the hydrogeologic conditions present, may represent a significant disadvantage because of challenges for effective delivery. Most of the experiments conducted by Pennell et al. were small scale batch-type tests. Thus, while the provided a great deal of insight into processes at the soil grain to molecular-scales, they generally did not address transport-scale issues. In contrast, the physical model experiments utilized in the work we are presenting here allow interactions between chemical and physical processes to be examined with a level of detail sufficient for use in evaluating numerical models

### 2.6. SUMMARY

The heating characteristics of ERH make it most appropriate for combining with other remediation approaches. The coupled physical processes that are the focus in the work described here are enhanced water flow, bubble formation, heterogeneous boiling. The combination of heating and in situ chemical oxidation are also examined, using persulfate as the model oxidant, are also examined. This project was carried out in conjunction with several other thermal projects (in particular, SERDP ER-1423 (Baker & Hiester, 2009) and SERDP ER-1419 (Pennell et al., 2009)) and was intended to complement those other approaches by focusing on ERH and processes occurring at the centimeters to meters scales and at less than  $100^{\circ}\text{C}$ .

### **SECTION 3. MATERIALS AND METHODS**

# 3.1. LOW TEMPERATURE ERH, SUBSURFACE FLOW AND TRANSPORT IN HOMOGENEOUS MEDIA

Electrical Resistance Heating (ERH) is most often applied as an in situ technology for the removal of volatile contaminants from groundwater. In this context the general strategy is to heat the subsurface to the boiling point of water to remove the contaminants by volatilization and steam stripping (Buettner & Daily, 1995; Davis, 1997; U.S.EPA, 2004). ERH is one of several thermal methods (also including thermal conduction, hot water and steam injection) that are currently in use at contaminated sites. As discussed below, in addition to the effects of boiling, elevated temperatures increase the vapor pressures, solubility, and diffusion coefficients of the contaminants while lowering viscosity, density, and sorption coefficients (Boulding & Ginn, 2004; Looney & Falta, 2002).

ERH has several advantages relative to the other methods, including that it: 1) can operate at a range of temperature; 2) couples well with other processes; 3) can be targeted at small areas; and 4) does not rely on fluid delivery. ERH most often utilizes and alternating electrical current (1-, 3- or 6-phase) and an array of electrodes (linear, triangular or hexagonal depending on the number of phases).

Historically, most ERH applications for nonaqueous-phase liquid (NAPL) removal raise the subsurface temperature to the boiling point of the water-NAPL immiscible mixture. In this case, the primary mass removal mechanisms are volatilization and/or steam distillation. In these cases, contaminant vapors and fluids are collected and treated on-site (Beyke & Fleming, 2005; Davis, 1998). Therefore, ERH requires significant infrastructure to both manage and treat the fluids, as well as to deliver the needed power to increase the subsurface temperatures to the boiling point. In addition, the high temperatures can result in unfavorable conditions for secondary remediation techniques, such as bioremediation and may also have geotechnical implications.

An alternative to conventional ERH is to operate it at sub-boiling. Lower temperatures require less power, by both decreasing heat loss and by avoiding the energy-intensive volatilization process. Lower temperatures will also require less infrastructure, because the collection of vapor and NAPL phases can be avoided. Heating to lower temperatures may also enhance microbial activity or promote abiotic degradation, further enhancing remediation (Costanza, 2005; Friis et al., 2006; Rossman et al. 2006; U.S.EPA, 2004). In addition, low temperature ERH may still take advantage of less aggressive mass removal, since boiling of immiscible mixtures occurs at a temperature below the boiling point of either water or the organic compound; sometimes referred to as the heteroazeotropic boiling point, as it relates to immiscible liquids (Kiva et al., 2003).

At temperatures below the heteroazeotropic boiling point there are still a number of processes that can be important from an in situ remediation process. Changes in density brought about by heating can lead to significant buoyancy effects, especially in high-hydraulic conductivity aquifers. Decreasing viscosity with increasing temperature can also increase

advective flow within the heated zone. In addition, bubble formation due to the combined effects of dissolved contaminants, atmospheric gases and the vapor pressure of water can have significant effects on the remediation process. While all of these can be important for low-temperature ERH, most have not been examined using a numerical model that explicitly couples the ERH process with groundwater flow and contaminant transport.

To date, ERH literature has focused on high temperature applications (Buettner & Daily, 1995; Carrigan & Nitao, 2000; Hiebert et al., 1989; Hiebert et al., 1986; McGee & Vermeulen, 2007). In most of these studies there was no consideration of water flow (Hiebert et al., 1986; Vinsome et al., 1994; McGee & Vermeulen, 2007) and only the temperature dependence of the organic phase viscosity was included. Carrigan & Nitao (2000) and Hiebert et al., (1989) considered fluid transport while modeling ERH heating, but dependent properties such as fluid density or viscosity were not examined and buoyancy effects were ignored in part because mass removal in these cases was through volatilization. However, mass removal and transport at low temperatures will be dominated by advection, dispersion, desorption and biological/chemical reactions. All these mechanisms are temperature dependent, therefore understanding the effect of temperature on these processes is necessary to optimize remedial efforts.

Buoyancy effects have been well documented in briny or coastal aquifers by (Konz et al. (2009); Langevin & Guo (2006)), where buoyancy effects are due to changes in groundwater solute concentration. In addition, Diersch & Kolditz (2002) examined the effect of variable density due to geothermal heating, where convective water flow was seen in regions of high permeability. Density effects were also examined by Molson et al. (1992) who developed a finite element model for energy transport after hot water injection into a shallow unconfined aquifer. Temperature dependent density and viscosity of water were considered in this study and the movement of the thermal plume was influenced by the induced buoyancy.

Few studies have looked at buoyancy effects on groundwater movement as it pertains to ERH and contaminant remediation. O'Carroll & Sleep, (2007, 2009) examined the effect of temperature on interfacial tension and viscosity during hot water flushing, and showed that heat can have a significant impact on contaminant removal. However, changes in groundwater hydraulics and contaminant transport due to buoyant flow were not examined.

Here we present a new two dimensional (2-D) electro-thermal model for low temperature ERH that simulates fully coupled electrical current flow, heat transport, water flow, and solute transport. This study explores the effect of low temperature heating on subsurface hydraulics and solute transport in the context of soil and groundwater remediation. The model incorporates several temperature dependent parameters including density, viscosity, electrical conductivity, and diffusion coefficient. Model performance is evaluated with 2-D lab scale experiments, predicting power consumption, voltage, temperature distribution, and mass transport through the system.

# 3.1.1. Model Theory

# Modeling Voltage

Modeling of ERH is based on Ohm's Law which relates the current density (J), to the electric potential (V) and electrical conductivity of the medium  $(\sigma)$ . Electromagnetic effects are neglected since ERH is operated at low frequencies (60 Hz) resulting in quasi-static electric fields. Therefore currents associated with time varying magnetic fields are considered negligible (Hiebert et al., 1986). Ohm's Law states:

$$\vec{J} = -\sigma \nabla V$$

[3.1]

Electrical conduction in clean sands is largely due to ionic conduction through the bulk pore fluid (Butler & Knight, 1998; Friedman, 2005; Sen, 1992; Sen & Goode, 1988) and can be described using Archie's Law (Archie, 1942), while less permeable soils need to take into account the presence of clay particles (Butler & Knight, 1998; Sen & Goode, 1988; Waxman & Smits, 2003). For both types of soils, the electrical conductivity of the subsurface depends on the fluid electrical conductivity ( $\sigma_w$ ), which is temperature dependent, as described by (Arps, 1953):

$$\sigma_{w2} = \sigma_{w1} \frac{T_2 + 21.5}{T_1 + 21.5} \tag{3.2}$$

where  $\sigma_{w1}$  corresponds to a water electrical conductivity at a reference temperature  $T_1$ .

Using conservation of electric charge and allowing for a spatially variable electrical conductivity, due to temperature dependence, Equation (2.1) becomes:

$$\nabla \cdot (\sigma \nabla V) = Q$$

[3.3]

where Q represents sinks and sources of electric charge, and is non-zero only at the electrodes. Since ERH uses alternating current, the electrode potential is a function of time resulting in a phase-shifted voltage distribution:

$$V = V_o cos(\omega t + \varphi)$$

[3.4]

where  $V_0$  is the voltage amplitude,  $\omega$  is the angular frequency, and  $\varphi$  is the phase angle. The power dissipated can be calculated by either averaging the value through a power cycle, treating the voltage as a phasor quantity, or separating the electrode voltages into separate, single-phase solutions as described by Carrigan & Nitao (2000). The electro-thermal model presented here

uses phasors to calculate the voltage distribution, as described by Hiebert et al., (1986, 1989) and McGee & Vermeulen (2007):

$$V = V_1 cos(\omega t) + V_2 sin(\omega t) = V_1 + jV_2$$
[3.5]

where  $V_1$  and  $V_2$  correspond to the real and imaginary roots of the voltage (rms), respectively.

# **Modeling Power**

The power dissipation in the subsurface (U) is determined using Equation [3.6]

$$U = \sigma \mid \nabla V \mid^2$$
 [3.6]

# Modeling Temperature

the energy equation (Equation 3.7) to obtain the subsurface temperature distribution

$$\frac{\partial}{\partial t} \left[ \rho_w \phi c_w T + (1 - \phi) \rho_b c T \right] + c_w \rho_w \nabla \cdot \left[ \vec{q} T \right] - K_H \nabla^2 T - U = 0$$
[3.7]

where T is the temperature  $\rho_w$  is the density of water,  $\phi$  is soil porosity,  $\rho b$  is the bulk density of the soil, c is the heat capacity of the soil,  $c_w$  is the heat capacity of water, qT is the Darcy velocity vector, and  $K_H$  is the bulk thermal conductivity.

### Modeling Flow

Since fluid density changes with temperature, the Darcy velocity is written in terms of an equivalent freshwater head  $(h_f)$ , which is defined as (Frind, 1982):

$$h_f = \frac{P}{\rho_f g} + z \tag{3.8}$$

where  $\rho_f$  is the freshwater density (taken to be the density at ambient temperature), while  $\rho$  is the density of the fluid at the current temperature. This leads to a form of Darcy's Law for systems with varying densities:

$$\vec{q} = -\frac{kg\rho_f}{\mu} \left[ \nabla h_f + \rho_r \nabla z \right]$$
[3.9]

where  $\rho_r$  is the density coefficient  $(\rho - \rho_f)/\rho_f$ , k is the soil permeability and  $\mu$  is the water viscosity. Similar procedures have been used by others when modeling density driven flow in briny aquifers (Langevin & Guo, 2006), deep aquifer systems (Bachu, 1995), and gas transport (Sleep & Sykes, 1989)

# **Modeling Transport**

Mass transport in the system is calculated taking into account advection and dispersion (Sleep & Sykes, 1993a):

$$\frac{\partial}{\partial t} \left[ \rho_w \phi C \right] + \nabla \cdot \left[ \rho_w C \vec{q} \right] + \nabla \cdot \left[ \phi \vec{J}^D \right] = 0$$
[3.10]

where C is the mass fraction of the contaminant and  $J^D$  is the dispersive flux vector.

# Fluid-dependent properties

Liquid viscosity decreases with increased temperature. There are many approximations to this relationship including the Andrade equation and the Lewis-Squires method (Poling et al., 2001). Here the relationship described by the Van Velzen, Cardozo and Langenkamp Method (Reid et al., 1987) is used:

$$log(\mu) = \beta_{\mu} \left[ \frac{1}{T} + \frac{1}{\tau_o} \right]$$
[3.11]

where  $\beta$  and  $\tau_0$  are the viscosity temperature dependence parameters (Munson, 2002). Liquid densities depend on pressure and temperature. As the temperature increases, the density of the fluid decreases and can be approximated using polynomial interpolation functions (Yang & Edwards, 2000) or using the following linear relationship (Gebhart et al., 1988):

$$\rho = \rho_0 [1 + \alpha (P - P_0)] [1 + \beta (T - T_0)]$$
[3.12]

where  $\rho$  is the liquid density,  $\rho_0$  is the reference density at a reference temperature T0 and reference pressure P0, T is the temperature, P is the pressure,  $\alpha$  is the pressure coefficient, and  $\beta$  is the thermal expansion coefficient. In the electro-thermal model, the pressure differences were assumed negligible. The aqueous molecular diffusion coefficient was calculated from a ratio of viscosities as follows (Reid et al., 1987):

$$\frac{D_d}{(D_d)^{ref}} = \left(\frac{\mu_w}{\mu_w^{ref}}\right)^{-1.14}$$

[3.13]

where  $D_d$  is the diffusion coefficient,  $\mu$ w is viscosity,  $\mu_w^{ref}$  is the reference water viscosity and  $D_d^{ref}$  is the reference diffusion coefficient, both taken at the ambient temperature.

### 3.1.2. Materials and Methods

To study transport processes in the subsurface during heating, an experiment was conducted in a polycarbonate "visualization" physical model (60 cm long, 45 cm tall and 1 cm thick, Figure 3.1-3.3) using single-phase ERH. The experiments focused on the movement of groundwater during subsurface heating. The tank was packed with 0.5 mm glass beads with a hydraulic conductivity of approximately 0.3 cm/s. Groundwater was injected at a rate of 5 cm³/min using a multi-channel peristaltic pump with five injection and 5 extraction wells. The tank included two columns of 6 electrodes each. The first column was connected to a 120 V AC power source while the other six electrodes were attached to neutral. To increase the electrical conductivity of the system, a 2 g/L sodium sulfate solution was used as groundwater.

The temperature data were collected through 48 thermocouples that surrounded the heated zone. Temperature and AC current measurements were recorded using Labview® and a Measurement Computing® data acquisition board. The same system was used to control temperature during the experiment. Four of the thermocouples, located 2-3 cm from the electrodes, were used to maintain temperature at the target value. Before the start of the experiment, the tank was fully water saturated.

An initial isothermal experiment using Rhodamine WT was conducted in the model to allow comparison to the non-isothermal experiments. In the second experiment, the temperature was increased initially to  $30^{\circ}$ C and maintained for 36 minutes, after which the temperature was increased to  $50^{\circ}$ C. To examine the hydraulics of the heated system, Rhodamine WT was injected at a rate of  $0.03 \text{ cm}^3$ /min into 5 injection ports once the temperature reached  $50^{\circ}$ C (approximately 2 hours after the start of the experiment). The tracer was injected for 140 minutes. Time-lapse Images of the tracer were captured using a Nikon D90 camera interfaced to a computer. During the experiment the ambient temperature remained relatively constant at  $21.2 \pm 1.2^{\circ}$ C. The experiment lasted 8 hours and 45 minutes. The photographs were post-processed with Labview® to highlight distribution of the tracer.

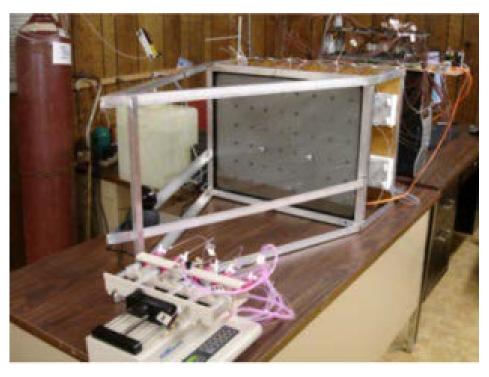


Figure 3. 1. Photograph of the physical model used for visualization experiments. During operation the aluminum frame is fully enclosed with optically-black covers. The syringe pump in the foreground is used for tracer injection.

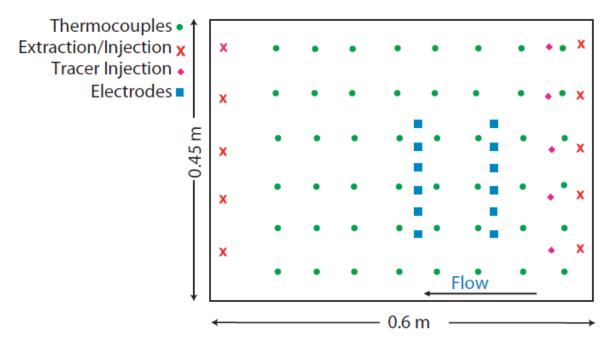


Figure 3. 2. Schematic drawing of the 2D visualization tank. The green circles are thermocouple locations, the blue squares are electrode locations, the red Xs are injection and extraction

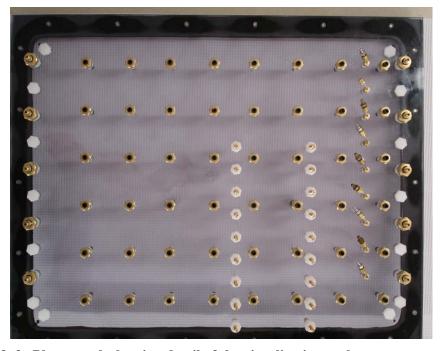


Figure 3. 3. Photograph showing detail of the visualization tank.

## 3.1.3. Numerical Approach

The electro-thermal model equations were discretized using block-centered implicit finite differences. At the beginning of each time step the voltage distribution was calculated using Equation [3.4] with electrode voltages applied as source terms and electrical conductivities calculated using temperatures from the previous time step. The boundaries were assumed to be insulated with respect to current flow. Following calculation of the electric field, the power dissipation was calculated using Equation [3.5]. The groundwater flow equation given by Equation [3.9] was then solved for hydraulic head and Darcy velocity, with temperature dependent fluid density and viscosity calculated using temperatures from the previous time step.

As the heat and flow equations are coupled through the temperature dependence of water properties, an iterative approach was used. Given the Darcy velocities and heat transfer coefficients, the heat equation [3.6], was solved for temperature. The solution of the water flow and heat transport equations was then repeated iteratively, using the updated values of temperature dependent (viscosity, density) parameters from the current time step (implicit formulation) to calculate new fluid properties. This was performed until an absolute convergence criterion of  $1 \times 10^{-6}$  for temperature was achieved. The Darcy velocities and temperatures obtained from those calculations were then used to calculate mass transfer coefficients (dispersion coefficient) and the mass transport equation [3.7] was solved for solute mass fractions. Parameters that changed spatially were averaged between grid blocks, using the harmonic mean value. These parameters included the hydraulic conductivity, electrical conductivity and thermal conductivity.

The model was capable of applying upstream or midpoint weighting methods for the solution of the advective-dispersive equation. The heat transport boundary conditions for simulating the tank experiments were zero flux for the top and bottom of the system, while a known energy flux was specified at the inlet. Since all experiments were performed in uninsulated polycarbonate tanks, there were heat losses across the tank walls. These were modeled by calculating the amount of energy required to heat the polycarbonate walls as well as the heat loss through an air buffer zone outside the tank. At each node, a heat sink term was added to account for the energy required to heat the wall:

$$U_{wall} = \frac{2c_w(T^t - T^{t-1})}{t}$$

[3.14]

where  $c_w$  is the volumetric heat capacity of the wall, and T and  $T^{-1}$  are the wall temperatures at time steps t and t-1.

The heat loss term for the conduction across the air layer was calculated using:

$$U_{air} = \frac{2K_{Hair}(T^t - T_{ref})}{d \cdot \triangle y}$$
[3.15]

where d is the air buffer layer thickness,  $T_{ref}$  is the ambient temperature outside the tank,  $\Delta y$  is the thickness of the tank, and  $K_{Hair}$  is the thermal conductivity of air. The air buffer layer thickness was changed until the Pearson product correlation coefficient (PMCC) during the heating portion of the experiment was maximized and the temperature distribution was comparable to the experimental data. This resulted in an air buffer thickness of 2 mm. (The same heat loss terms was also used for the large tank simulations discussed in Section 3.2) The loss terms were multiplied by a factor of two to account for the two sides of the tank and the losses at the top and bottom of the tank were considered negligible.

The boundary conditions for flow and mass transport were zero flux for the top and bottom of the system. The injection and extraction wells in the visualization tank were modeled as sources and sinks, respectfully, while the large tank assumed a constant flow inlet and constant head outlet boundary condition. The tracer injection wells were modeled as sources. The linear equations for the discretized current, groundwater flow, heat transport, and mass transport were evaluated using the backslash operation in MATLAB which uses appropriate algorithms, depending on the structure of the matrix. For temperatures, upstream weighting was used, defined by:

$$T_{in} = T_i$$
 for  $h_f > h_{i+1}$  (q<sub>x</sub> is positive)  
 $T_{in} = T_{i+1}$  for  $h_f < h_{i+1}$  (q<sub>x</sub> is negative)

[3.16]

To simulate the solid state relay that turned the power to the electrodes on and off, a temperature check at the thermocouple location was incorporated into the numerical model. Once the temperature at the thermocouples reached the set point, the power was switched off and turned back on when the temperature dropped down below the set point temperature. During each time step energy and mass balances were performed on the numerical model system to ensure mass and energy conservation.

The electro-thermal model was compared to a 1-D Ogata-Banks solution for advective and dispersive transport (Ogata, 1970). In addition, the power and voltage distributions were compared to an analytical one-dimensional solution similar to (Hiebert, 1987). There was excellent agreement between the analytical solutions and the model, giving a PMCC of 1 for both voltage and power. To further evaluate the model, the power consumption, temperature, fluid velocity, and mass movement in the 2-D tank were simulated. The tank properties as well as model parameters are given in Table 3.1. There was no sorption of Rhodamine WT onto the glass beads.

**Table 3. 1. Properties of the 2D Visualization and simulation parameters (sources:** <sup>a</sup>Gori et al., 2001; <sup>b</sup>Lide, 2006; <sup>c</sup>Michaeli, 2003)

		Small Tank
		glass beads
$\sigma_w$	Water Electrical Conductivity $(S/m)$	0.24
$K_{Hb}$	Medium Thermal Conductivity $(W/mK)^a$	0.9
$K_{Hair}$	Air Thermal Conductivity $(W/mK)^b$	0.026
$c_w$	Wall Volumetric Heat Capacity $(J/Cm^3)^c$	$1 \times 10^6$
n	Porosity (-)	0.4
k	Permeability $\times 10^{-10} (m^2)$	4
$K_x/K_z$	Anisotropy Ratio (-)	0.7
$\triangle y$	Tank Thickness (m)	0.018
dx, dz	Discretization $(m)$	0.002

## 3.2. INFLUENCE OF SOIL HETEROGENEITY ON ENERGY AND MASS TRANSPORT

Two approaches for assessing the role of ERH during mass transport in heterogeneous media are presented here. The first is to use a combination of physical model studies and numerical modeling to evaluate the performance of the numerical model. The second is to apply the model to well-characterized heterogeneous systems to better understand the impacts in "realistically-complex" subsurface settings.

#### 3.2.1. Large Tank Experiments

A second experiment was conducted in a physical model tank that was 1.2 m tall by 2.4 m long and 0.15 m thick (Figures 3.4 and 3.5). The tank walls were again made of polycarbonate, and the tank was filled with medium silica sand with 0.3 m of a mixture of sand and illite clay at the bottom. Groundwater was injected into a fully-screened well at the inlet end of the tank using a constant-rate ceramic-piston pump and a constant-head reservoir was used at the effluent end. The hydraulic conductivity of approximately 0.014 cm/s. The sand and illite clay had a hydraulic conductivity ~3 orders of magnitude lower than the sand. The groundwater velocity for these experiments was approximately 0.75 m/d (Darcy velocity ~8.7 x 10 <sup>-6</sup> m/s) and the injected water had a concentration of 1.2 g/L of sodium sulfate. Temperature and voltage were monitored at 70 locations using a data acquisition and control system similar to that used in the visualization tank.

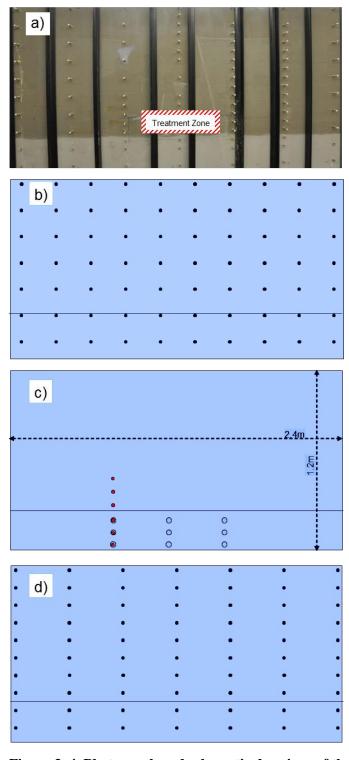
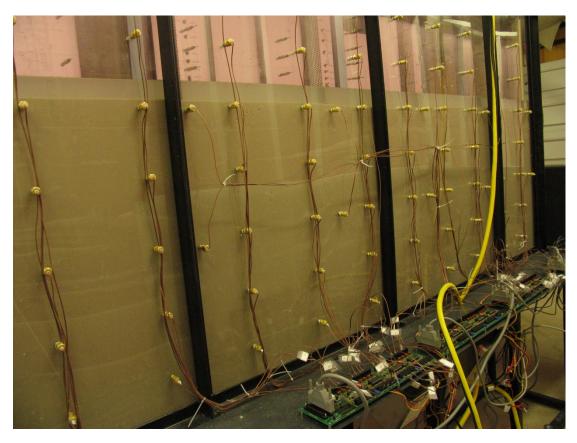


Figure 3. 4. Photograph and schematic drawings of the large physical model. a) photograph of the physical model; b) schematic drawing of the temperature monitoring point array; c) locations of the electrodes used in the up-gradient (solid red circles) and beneath (open black circles) experiments; and d) array of voltage measurement locations



 $Figure \ 3.\ 5.\ Photograph\ of\ the\ large\ model\ during\ filling\ and\ showing\ the\ thermocouple\ array\ used for\ temperature\ measurements.$ 

A total of 12 electrodes were placed in the tank to allow two different heating arrangements, and three different heating experiments were conducted in this model. In the first, an array of six electrodes up-gradient of the treatment zone (solid circles in Figure 3.4c) were connected to 120 volt AC power supply (electrodes 2, 4 and 6 were connected to the "hot" electrical lead and 1, 3 and 5 to the "neutral "electrical lead.). In the second experiment, 9 electrodes (larger open circles in Figure 3.4c) were used, with the two 6 outer electrodes connected to the "hot" lead of the 120 V AC supply and the center 3 connected to the neutral lead. For each experiment the voltage during ERH was measured throughout the model at an array of 70 locations (Figure 3.4d), the sampling ports also serve as voltage points). Temperature was controlled by monitoring thermocouples located close to the electrodes.

In these experiments once the temperature distribution had reached steady-state, a dye tracer was introduced into the tank at five up-gradient locations and the movement of the tracer was observed down the length of the tank.

Following the tracer experiments, a DNAPL (TCE) was injected into the sand to create a small source above the sand/clay layer. Aqueous TCE concentrations were measured at a number of sampling points down-gradient of the source. In addition, the total flux of TCE from the source was measured at the effluent of the tank. An area up-gradient of the source was then heated from 20°C to 50°C and then to 75°C to increase flow through the source zone and increase mass flux.

#### 3.3. BUBBLE FORMATION DURING LOW-TEMPERATURE ERH

Heating in the subsurface will result in gas production when the sum of the vapor pressures of all of the volatile constituents (including dissolved gases, contaminants and water) exceeds the in situ pressure. Sustained gas formation will occur when the subsurface temperature reaches the boiling point of water at the hydrostatic pressure where the heating occurs. Sustained boiling can also occur at below the boiling point of water if sufficient volatile materials are present. In the context of in situ thermal remediation, the most significant case is when non-aqueous phase liquids are present. This case is often called heteroazeotropic boiling. If sustained boiling occurs, contaminants present in the boiling zone will be carried upward in the vapor phase, where they can either re-condense or reach the water table.

It is important to recognize that bubbles can also form at temperatures well below the boiling point of water or azeotropes because of the presence of dissolved atmospheric gases and/or other dissolved contaminants. However, in this case gas formation will not be sustained, because the dissolved concentrations of those dissolved species will quickly be reduced once bubble formation begins. As a consequence, upward migration of those bubbles may be limited, and those bubbles can persist. This can be important because, if the pore space contains a significant fraction of bubbles, the permeability of water through the medium can be significantly reduced.

Various aspects of this behavior can be experimentally observed and numerically modeled, however, the processes are complicated and the predictive capability of the models is currently limited.

#### 3.3.1 Bubble Formation Mechanics

Most groundwaters contain dissolved gases derived from equilibrium with the atmosphere during recharge and/or processes occurring in the subsurface (e.g. microbial respiration). As a result, nitrogen, oxygen and carbon dioxide are typically present. Nitrogen concentrations are often near atmospheric concentrations, oxygen can be at that level, or below due to chemical interactions and carbon dioxide is often above equilibrium concentrations due to biogeochemical processes. (e.g.,Kulongoski et al., 2006). As the data in Table 3.2 indicate, groundwaters can frequently contain total dissolved gas volumes that are on the order of half the volume of the water containing them (i.e., 1 mL of water containing 0.5 mL of gas at STP.)

GAMA	Carbon dioxide	Nitrogen	Argon	Oxygen	Methane		
identification	(cm³ STP g⁻¹ H₂0)						
No.	x 10 <sup>-2</sup>	x 10 <sup>-2</sup>	x 10 <sup>-2</sup>	x 10 <sup>-2</sup>	x 10 <sup>-4</sup>		
Valley and	Plains wells						
NSFVP-34	35.5	4.71	4.31	1.16	0.41		
NSFVP-37	117	6.05	5.08	2.31	0.32		
NSFVP-38	16.7	4.48	4.20	0.72	4.87		
NSFVP-40	29.6	4.54	4.17	0.43	8.03		
Hydrothe	rmal study						
NSFHOT-01	14.2	1.05	1.10	0.56	44.0		
NSFHOT-02	22.7	1.97	1.49	0.41	97.3		
NSFHOT-03	283	4.75	3.86	1.42	0.66		
NSFHOT-04	50.8	2.18	2.01	1.21	103		
NSFHOT-05	4.58	0.36	0.44	0.45	3.35		
NSFHOT-06	22.1	4.35	3.76	0.60	98.4		
NSFHOT-07	4.94	3.41	1.89	0.71	313		

Table 3. 2. Measured concentrations of dissolved gas (cm3 per gram of water) from the California Ground-Water Ambient Monitoring and Assessment (GAMA) program (Kulongoski et al., 2006).

The solubilities of most atmospheric gases decrease with increasing temperature (Figure 3.6). Nitrogen is frequently found in excess of saturation with respect to atmospheric concentrations, and as a result, even a small amount of heating can result in bubble formation. Carbon dioxide, oxygen, argon, and methane can also contribute to bubble formation during modest heating.

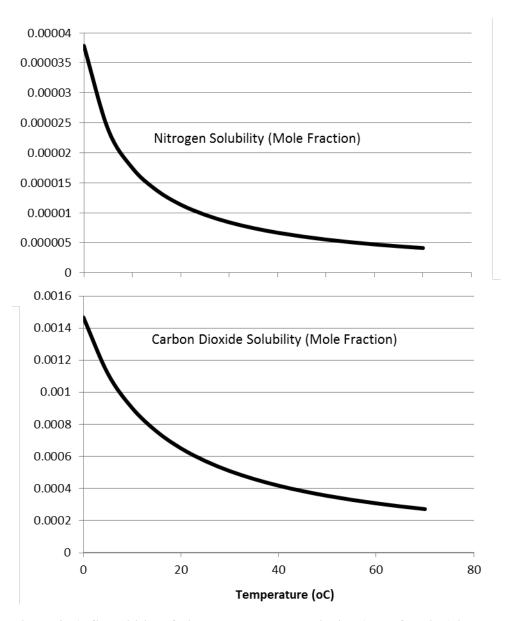


Figure 3. 6. Solubilities of nitrogen and carbon dioxide (mole fraction) in water as a function of temperature.

At temperatures of  $\sim 50^{\circ}$ C and higher the vapor pressure of water begins to have a significant role as well (Figure 3.7).

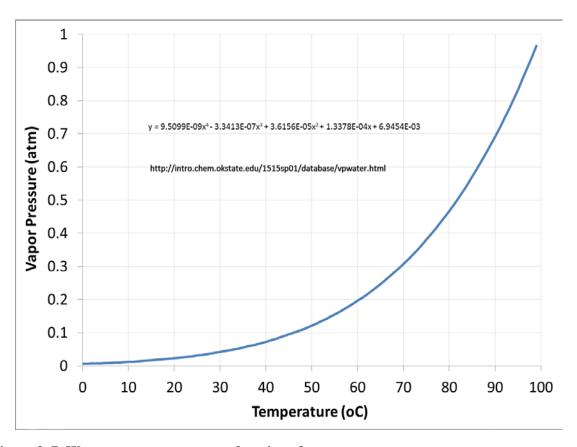


Figure 3. 7. Water vapor pressure as a function of temperature.

The temperature at which gas will form depends upon the dissolved concentration and the hydrostatic pressure. Figure 3.8 shows the case for water saturated with nitrogen gas at 1 atmosphere total pressure. As the hydrostatic pressure increases, the temperature at which a gas phase will form increases. This is due to changes in the Henry's gas constant which are driven primarily by decreased solubility with increasing temperature.

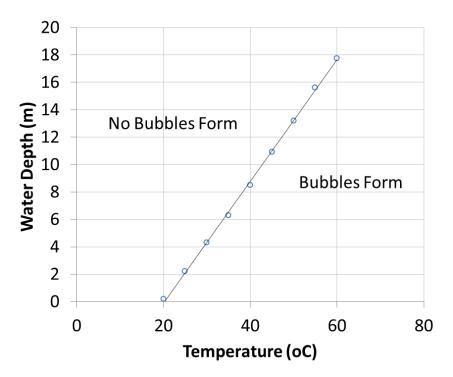


Figure 3. 8. Plot showing regions in which water saturated with gas at atmospheric pressure will produce bubbles as a function of temperature and pressure.

At the modest temperatures discussed here, the volume of nitrogen bubbles formed upon heating is small (e.g., <1% of the pore space). Conversely, if concentrations of a soluble gas like carbon dioxide are elevated (e.g., due to biogeochemical processes), then significant volumes of gas can form (as shown in Figure 3.9).

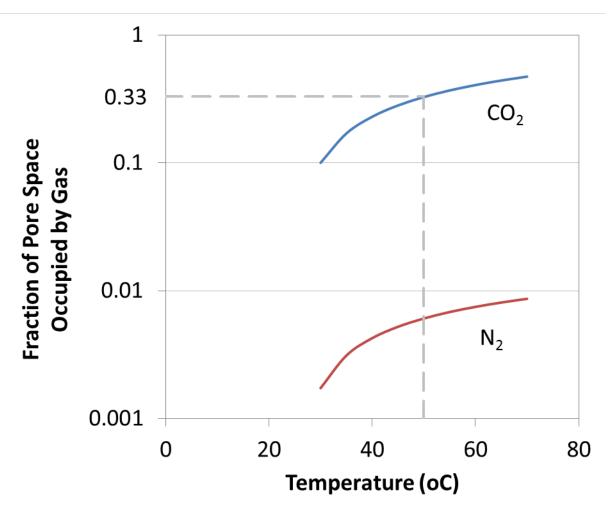


Figure 3. 9. Fraction of pore space occupied by gas as a function of temperature for carbon dioxide and nitrogen initially at saturation concentrations, 20°C and atmospheric pressure.

# 3.3.2. 2-D Laboratory Physical Model Experiment to Examine the Effects of Bubble Formation during Low-Temperature ERH

The physical model setup used for this experiment was similar to the one used for the heating experiment in section 3.1. In this case, rather than sparging the influent water with helium to prevent bubble formation, it was sparged with  $CO_2$ . During the first phase of the experiment, the volume of gas produced during the heating process was estimated. This was accomplished by calibrating the light transmission system for luminosity as a function of measured water content prior to the start of the experiment. Then, once the temperature distribution had stabilize at  $\sim 50^{\circ}$ C a tracer test was conducted to observe the effect of gas formation on flow.

## 3.4. HETEROGENEOUS AZEOTROPIC BOILING DURING LOW-TEMPERATURE ERH

Unlike the case for a dissolved contaminant, if a source zone containing a dense, non-aqueous-phase liquid (DNAPL) is heated to the temperature of the water/contaminant azeotrope, sustained gas production can result. The extent to which boiling occurs will likely depend upon the interfacial area between the two phases. From a source-zone remediation perspective, the extent to which the DNAPL phase can be removed by volatilization at this temperature is an important one. Stated another way, one might ask the question: Will complete removal of the DNAPL require heating to the boiling point of the most-volatile constituent (water or DNAPL). To address this question, a series of laboratory experiments were conducted and are described here.

#### **3.4.1.** Theory

Raolt's law provides an estimate of total vapor pressure of an ideal mixture. However, when a pure-phase DNAPL solvent is present, and when it is in contact with the water, the total vapor pressure at a given temperature can be calculated as the sum of the pure vapor pressure of the separate phases:

$$P_{\text{WATER}} + P_{\text{DNAPI}} = P_{\text{TOT}}$$
 [3.17]

The vapor pressures for each of the phases can be calculated as a function of temperature using Antoine's equation

$$log(P) = A - \left(\frac{B}{T+C}\right)$$
 [3.18]

where P is pressure typically reported in in mm Hg; A,B and C are constants available in the literature (e.g., (Yaws & H. Yang, 1989) and T is the temperature (°C)). As an example, the vapor pressure parameters for three important chlorinated solvent DNAPLs are listed in Table 3.3 and the resulting vapor pressures for those compounds are plotted in Figure 3.10.

	Α	В	С
carbon tetrachloride	6.8941	1219.6	227.17
tetrachloroethene	7.02	1415.5	221.01
trichloroethene	7.0281	1315.1	230.01

Table 3. 3. Antoine equation parameters for carbon tetrachloride, TCE and PCE (Yaws & H. Yang, 1989)

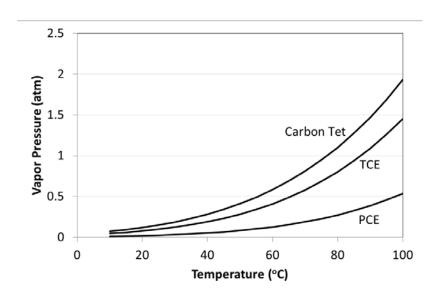


Figure 3. 10. Vapor pressures of carbon tetrachloride (CT), TCE and PCE as a function of temperature.

The composition of the gas produced by the heterogeneous boiling process can be derived directly from the fractions of the total vapor pressure contributed by the water and DNAPL. As discussed in the previous chapter, when sufficient gas is produced to induce upward displacement of the gas, it will move from the DNAPL zone into the overlying water. This process can be complicated due to variations in entry pressure of the gas into aquifer materials. As discussed above, it can also be complicated if the temperature of the overlying water is low enough that the vapor can re-condense. However, the movement of mass up from the DNAPL zone will increase the overall mass transfer from the DNAPL zone, and in the context of source removal is typically a desirable thing. That is almost certainly the case for pools of DNAPL within a source zone, which is the focus here.

#### 3.4.2. Materials and Methods

A series of 1-D and 2-D experiments were conducted to examine the processes controlling DNAPL removal under heterogeneous azeotropic boiling conditions (i.e., at temperatures below the boiling point of the DNAPL). The measurements made during those

experiments include a visual (photo) record, temperature measurements, mass recovery and (for 2-D only) change in fluid volume within the experiment. The 1-D experiments provided an approach for well-controlled conditions to be examined (e.g., a "pure DNAPL pool" emplaced without water, and well mixed sand, water and DNAPL). The 2-D experiments allowed DNAPL to be spilled into the granular medium to produce a quasi-realistic spill.

Carbon tetrachloride (CT) was used for these experiments because: 1) its boiling temperature is far enough below water that there is not a large co-distillation problem"; and 2) there is a  $\sim 10^{\circ}$ C temperature difference between the azeotrope and the boiling point (66.8 v. 76.8°C, respectively).

In both the 1-D and 2-D experiments, temperature was controlled by placing the entire experiment in a controlled-temperature bath (Figure 3.11). The experiments were designed such that, as the CT is volatilized, it moved up through the medium and the tube at the top of the experiment. The tube between the experiment and the condensing jacket was heated to  $\sim 100^{\circ}$ C with a heating tape. When the vapor got to the condensing jacket it was converted back to a liquid, which flowed into the collection vial and was weighed by the analytical balance. The temperature of the water bath, height of the water in the tube and the mass of CT collected were all recorded by a computer using Labview software.

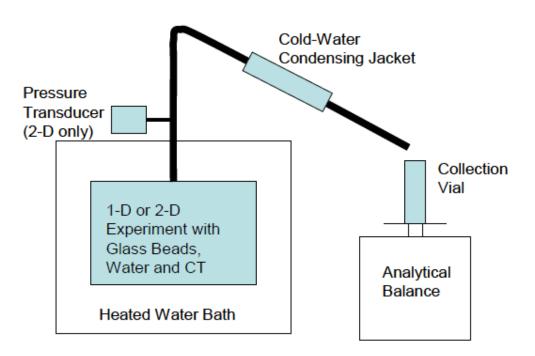


Figure 3. 11. Schematic representation of the experimental apparatus used for the heterogeneous azeotropic boiling experiments.

#### *3.4.2.1. 1-D experiments*

The 1-D experiments were conducted using 0.5 mm glass beads in a 40 mL glass vial. In the first experiment described here, 8 g of CT was placed in the bottom of the vial and the beads were added until the CT was fully contained within them. Water was then added to the vial and glass beads were added to fill the vial (while keeping them under saturated conditions.

To conduct the experiment, the temperature was ramped from ~25 to 69±0.9 and held at the latter value. Every 60 seconds a high-resolution photograph of the experiment was taken. For the second experiment, 10 g of CT were combined with water and glass beads in the vial such that the beads were all contained within the liquids. The contents were then stirred vigorously to distribute the CT throughout the water and beads. Water and beads were then added to finish filling the vial.

#### 3.4.2.2. 2-D experiment

The container for the 2-D experiments was a glass and aluminum tank similar to the one used for the flow experiments in Section 3.1. It had internal dimensions of ~55cm x 45 cm x 1.3 cm thick. Prior to filling the tank, an approximately 1 cm thick layer of saturated Illite clay was placed in the bottom. Water was then added to the tank and glass beads were added to fill the tank under saturated conditions. To conduct the experiment, 15 grams of CT were added to the tank at a position roughly in the center. The CT then flowed downward until it reached the clay and spread out laterally.

#### 3.5. THERMAL EFFECTS ON IN SITU CHEMICAL OXIDATION

The combination of low-temperature ERH and in situ chemical reactions represents a potentially-important approach for treatment of groundwater contaminated with chlorinated ethenes (e.g., TCE and PCE). Two aspects of the effects of temperature are examined here: 1) the rate of PCE oxidation; and 2) the persistence of the persulfate under thermal activation conditions. ISCO with persulfate requires activation, and this can be achieved with the heat from ISTR, so there may be advantages to combining these technologies. To explore this possibility, we determined the kinetics and products of chlorinated ethene oxidation with heat-activated persulfate and compared them to the temperature dependence of other degradation pathways.

Contaminant destruction with in situ chemical oxidation (ISCO) using persulfate (peroxydisulfate, persulfate)can be enhanced by activation, which increases the rate of persulfate decomposition to sulfate radicals (SO4  $\bullet$ ). This step initiates a chain of radical reactions involving species (including SO4  $\bullet$  and OH $\bullet$ ) that oxidize contaminants more rapidly than persulfate does directly. Among current activation methods, thermal activation is the least well studied. Combining new data for environmentally relevant conditions with previously published data, we have computed three sets of Arrhenius parameters (ln A and  $E_A$ ) that describe the rate of persulfate decomposition in homogeneous solutions over a wide range of temperature and pH.

In addition to interest in the rate at which contaminants degrade, it is important to understand the lifetime of the oxidant in the subsurface in order to understand its limitations with regard to transport. In this context, aquifer solids are particularly important. Soil increases the

decomposition rate of persulfate due to reactions with organic matter and possibly mineral surfaces, but the kinetics are still pseudo-first-order in persulfate and conform to the Arrhenius model. A series of re-spike experiments with soil at 70°C was used to examine this and also to examine reactions rates once the oxidant demand had been met.

## 3.5.1. Background

In situ chemical oxidation (ISCO) of subsurface contamination is performed by injection of a chemical oxidant (e.g., hydrogen peroxide, permanganate, ozone, or persulfate) that produces reactive intermediates such as hydroxyl radical or sulfate radical (ITRC, 2005). The variety of ISCO methods makes this approach applicable over a range of settings. For example, hydrogen peroxide ( $H_2O_2$ ) premixed with chelated iron can be effective when injected directly into a contaminant source zone, which allows the hydroxyl radicals produced by iron-catalyzed degradation of  $H_2O_2$  to react with the contaminants before they react with other aquifer components (e.g., bicarbonate or natural organic matter (ITRC, 2005)). In contrast, contaminants in hard to reach areas may be treated more effectively with permanganate, which is less reactive and more selective than hydroxyl radicals, thereby allowing more time for the oxidant to be delivered to areas with contamination. Persulfate offers some of the advantages of both activated  $H_2O_2$  and permanganate (Watts & Teel, 2006). Persulfate is relatively stable and therefore can be delivered considerable distances in the subsurface (like permanganate), but it can be activated to produce sulfate radicals, which are very reactive with a wide range of contaminants.

There are two general ways of activating persulfate: homolysis of the peroxide bond using heat or light (eq 3.19) (Wilmarth & Haim, 1962)

$$S_2 O_8^{2-} \xrightarrow{\Delta \text{ or } h\nu} 2SO_4^{\bullet-}$$
 [3.19]

$$S_2O_8^{2-} + M^{n+} \rightarrow SO_4^{\bullet-} + SO_4^{2-} + M^{n+1}$$
 [3.20]

and an oxidation/reduction process (analogous to the Fenton reaction) with electron donors, including  $e^{-}(aq)$  from radiolysis of water (Neta et al., 1977) or low-valent metals ( $M^{n+1}$ ) such as  $Fe^{2+}$  and  $Ag^{+}$  (equation [3.20]) (Anipsitakis et al., 2006; Wilmarth & Haim, 1962). For in situ applications, recent attention has mostly focused on activation by equation [3.20] with (chelated)  $Fe^{2+}$  (Block et al., 2004; Liang et al., 2004a, 2004b), although heat activation by equation [3.19] continues to be used, especially in bench-scale studies (Block et al., 2004). It has been suggested that persulfate be activated by  $H_2O_2$  (Block et al., 2004; Robinson et al., 2004), but this may be due mainly to homolysis of the peroxide bond (as in equation [3.19]) by heat evolved from decomposition of the  $H_2O_2$ . Once persulfate is activated (equation [3.19] or [3.20]), the resulting sulfate radical initiates a chain of reactions involving other radicals and oxidants (equations [3.21-3.26]), some of which are potentially reactive intermediates, such as hydroxyl radical and peroxymonosulfate ( $HSO_5^-$ ).

$$SO_4^{\bullet -} + H_2O \rightleftharpoons HO^{\bullet} + H^{+} + SO_4^{2-}$$
 [3.21]

$$2SO_4^{\bullet -} \rightarrow S_2O_8^{2-}$$
 [3.22]

$$SO_4^{\bullet -} + HO^{\bullet} \rightarrow HSO_5^{-}$$
 [3.23]

$$2\mathrm{HO}^{\bullet} \to \mathrm{H}_2\mathrm{O}_2 \tag{3.24}$$

$$H_2O_2 \rightarrow H_2O + 0.5O_2$$
 [3.25]

$$H_2O_2 + S_2O_8^{2-} \rightarrow 2H^+ + 2SO_4^{2-} + O_2$$
 [3.26]

The variety of intermediate oxidants generated in activated persulfate systems complicates the kinetics of contaminant oxidation. In principle, the contaminant disappearance should be describable with a pseudo-first-order rate constant that is the sum of second-order terms for each oxidant where k" represents the second-order rate constants for the reaction of the contaminant with each reactive intermediate. Under most conditions, the dominant term in equation [3.27] is presumed to be the one involving sulfate radical (Couttenye et al., 2002; Fountain, 1998; Kolthoff & Miller, 1951), but it is not known how the relative significance of these terms varies with system parameters, such as temperature.

$$k_{\text{obs}} = k_{\text{SO}_4}^{"} \cdot [\text{SO}_4^{\bullet -}] + k_{\text{HO}}^{"}[\text{OH}^{\bullet}] + k_{\text{S}_2\text{O}_8^{2-}}^{"}[\text{S}_2\text{O}_8^{2-}] + k_{\text{other}}^{"}[\text{other}]$$
 [3.27]

As mentioned earlier, a potential advantage of persulfate is its stability before activation, which may allow delivery of the oxidant to contamination in hard to reach places. To take full advantage of this property, the best method of activating persulfate may be the remote, localized, and directed heating provided by some of the technologies used for in situ thermal remediation (ISTR). (For a review of ISTR heating technologies, see (Fountain, 1998)) This approach to activating persulfate contrasts favorably with activation methods that involve mixing reagents before injection (e.g., persulfate with chelated iron) because the latter inevitably result in reaction of some of the oxidant before it reaches the contaminated zone. In the case of persulfate activation with chelated iron, we expect that some of the sulfate radical produced will react with excess Fe<sup>2+</sup> (McElroy & Waygood, 1990) thereby lowering the concentration of sulfate radical that is available to degrade contaminants. This effect may account for the observation that iron

activation of persulfate is not always effective at degrading some contaminants that are degraded with persulfate activated by other methods (Block et al., 2004).

Combining ISTR with ISCO using persulfate may enhance remediation performance in more ways than just thermolysis of persulfate to sulfate radical (equation [3.19]). For example, k'' for all the terms in equation [3.27] will increase with temperature, resulting in faster oxidation of contaminants if the oxidant concentrations are not decreased. The latter, however, cannot be assumed because the concentrations of sulfate radical and other oxidants shown in equation [3.27] are the net result of many reactions (equations. [3.19]-[3.26]), the reactions of each oxidant with the contaminants and their byproducts, etc., each of which will have its own dependence of rate on temperature. An additional uncertainty is the effect of temperature on the relative rates of contaminant degradation by chemical oxidants other than persulfate and background degradation processes such as hydrolysis. This study addresses these issues for the chlorinated ethenes by determining the temperature dependence of the kinetics and products of their oxidation by persulfate and comparing these results to calculations made from previously published data on the degradation of the chlorinated ethenes by permanganate and hydrolysis.

Since the lifetimes of the reactive activation products of persulfate are short, the effectiveness of persulfate for degrading chlorinated ethenes will also depend on its ability to be delivered to where it is needed, and then to produce those reactive products. Activation of persulfate in situ by mixing with Fe<sup>2+</sup> or other ions is challenging because of the difficulties of delivery of multiple mobile fluids to the same subsurface location. In that context, thermal activation has a distinct advantage, because delivery of a second reactive fluid is not necessary.

Delivery followed by in situ thermal activation has another advantage in that it may minimize the loss of persulfate due to soil oxidant demand in non-target treatment areas. In the context of ISCO, persulfate oxidant demand by aquifer materials has been considered in only a few published studies (e.g, Brown et al., 2004; Costanza et al., 2010; Dahmani et al., 2006; Haselow et al., 2003) but detailed studies on permanganate oxidant demand (Jones et al., 2006; Mumford Thomson, 2002; Mumford et al., 2005; Urynowicz et al., 2008) have shown that the kinetics of this process are complex, making the results highly dependent on test conditions such as oxidant concentration, exposure time, mixing regime, etc. This uncertainty regarding the characterization of natural oxidant demand (NOD) for persulfate is a major obstacle in the design of field-scale applications of activated persulfate for ISCO. In this study, we provide a more complete and quantitative understanding of the primary processes involved in persulfate oxidant demand, using well-mixed batch reactors containing homogeneous aqueous solutions, with and without aguifer solids. We emphasized several aspects of this problem that have not received much attention in previous work on persulfate NOD, including quantitative decomposition kinetics, the effect of temperature, and implications for the lifetime and diffusion distance of persulfate during injection into the subsurface. The latter are of direct practical significance to the field-application of activated persulfate because the time between injection and delivery to contaminated areas can be on the order of weeks or months, depending in part on how far the contaminants are from the primary zones of groundwater flow (e.g., if they are in diffusioncontrolled regions). The effect of temperature on the decomposition of persulfate is also of practical interest because of the potential advantages to performing heat activation of persulfate by combination of ISCO with in situ thermal remediation (Waldemer et al., 2007).

Persulfate Thermal Decomposition Chemistry. In this section the kinetics of persulfate decomposition are outlined. The decomposition reactions are, of course, similar to the radical-producing reactions discussed above. However, here they will be formulated in the context of the lifetime of the persulfate, rather than for the contaminant disappearance. Kolthoff & Miller (1951) and Wilmarth & Haim (1962) have concluded that the overall reaction for uncatalyzed, thermally-activated aqueous decomposition of persulfate between neutral and alkaline pH (equation [3.28]) is initiated by homolysis of persulfate (equation [3.29]) followed by oxidation of water by the resulting sulfate radicals (equation [3.30]), and disproportionation of the resulting hydroxyl radicals to dioxygen (equation [3.31]).

$$S_2O_8^{2-} + H_2O \rightarrow 2HSO_4^- + \frac{1}{2}O_2$$
 [3.28]

$$S_2O_8^{2-} \xrightarrow{\Lambda} 2SO_4^{\bullet-}$$
 [3.29]

$$SO_4^{\bullet-} + H_2O \rightarrow HSO_4^{\bullet-} + OH^{\bullet}$$
 [3.30]

$$2OH^{\bullet} \rightarrow H_2O + \frac{1}{2}O_2$$
 [3.31]

For pH < 3, these studies have explained the increased rate of persulfate disappearance by slightly different overall reactions, for example (equation [3.32])

$$S_2O_8^{2-} + H_2O \rightarrow H_2SO_5 + SO_4^{2-}$$
 [3.32]

could arise by acid catalyzed asymmetric fission of persulfate (equation [3.33]) followed by hydrolysis of the SO4 intermediate (equation [3.34]).

$$S_2O_8^{2-} + H^+ \Longrightarrow_{slow} HSO_4^- + SO_4$$
 [3.33]

$$SO_4 + H_2O \rightarrow H_2SO_5$$
 [3.34]

There has been much less consideration of persulfate decomposition under strongly alkaline conditions, but one study (Chandra Singh, 1976) showed increased rates of persulfate disappearance that were attributed to hydroxide-initiated fission of persulfate (equation [3.35]) followed by decomposition of the peroxymonosulfate intermediate (equation [3.36]).

$$S_2O_8^{2-} + OH^- \longrightarrow HSO_4^- + SO_5^{2-}$$
 [3.35]

$$SO_5^{2-} \rightarrow SO_4^{2-} + \frac{1}{2}O_2$$
 [3.36]

In all three cases, the first step (equations. [3.29], [3.33] and [3.35]) is expected to be rate determining, so we can propose the following overall rate law for decomposition of persulfate as a function of pH (equation [3.37])

$$-\frac{d[S_2O_8^{2-}]}{dt} = k_1[S_2O_8^{2-}] + k_2[H^+][S_2O_8^{2-}] + k_3[OH^-][S_2O_8^{2-}]$$
[3.37]

by combining previously proposed formulations for the acid to neutral and basic conditions (Chandra Singh, 1976). Under pseudo first-order conditions, equation [3.37] simplifies to a general expression for  $k_0(k_{\text{obs}})$  as a function of pH.

$$k_0 = k_1 + k_2[H^+] + k_3[OH^-]$$
[3.38]

All of the experimental work reported here targeted the pH region dominated by  $k_1$ , because that is the most generally relevant regime for in situ applications; however, we have included some previously published data for the extreme pH regimes in our analysis because they validate the consistency of the model and there is some interest in using alkaline pH to activate persulfate for ISCO (Block et al., 2004). Upon activation of persulfate, the resulting strong oxidants (especially sulfate radical, hydroxyl radical, and  $HSO_5^-$ ) can go on to react with contaminants of concern, soil organic matter, or anions such as chloride or carbonate. Collectively, these reactions create the oxidant demand for persulfate—ultimately converting it to two equivalents of sulfate.

At the same time, these reactions maintain the concentrations of the reactive intermediates which results in degradation of contaminants. An important, and sometimes overlooked, consequence of the kinetics controlling the fate of reactive intermediates like sulfate and hydroxyl radicals is that their high turnover rate gives them very short life-times (milliseconds to a few seconds in aqueous solutions, Huie & Clifton, 1993 Banerjee & Konar, 1984), which means that there can be negligible transport of the reactive intermediates in the subsurface. Instead, the delivery of oxidant for remediation of groundwater contaminants depends entirely on the transport of the precursor oxidant (persulfate, in this case), hence the need for a more quantitative understanding of the processes that limit the lifetime of persulfate during in situ applications.

#### 3.5.2. Materials and Methods

**PCE dechlorination experiments.** Saturated stock solutions of the chlorinated ethenes were made by allowing the pure non-aqueous-phase liquid to equilibrate with deionized, air-saturated water overnight with gentle stirring. Organic co-solvents were never used. Sodium persulfate solutions were made not more than 3 h before use in experiments.

Reactions were carried out in 40-mL volatile organic analysis (VOA) vials with Mininert valves (VICI Precision Sampling, Inc., Baton Rouge, LA) incubated without shaking in water baths at 30, 40, 50, 60, and  $70^{\circ}$ C ( $\pm 1^{\circ}$ C). Most experiments were performed without buffers or ionic strength compensation to avoid potential complications due to reaction between these additives and radical species produced during the experiment. Although some studies of reactions with activated persulfate have been done with pH and ionic strength control (e.g., Liang et al., 2003), the risk of side reactions is great because radicals react readily with many common inorganic anions. Furthermore, the risk of significant pH or ionic strength effects on the results reported here is small because the chlorinated ethenes are uncharged, and persulfate and most of the significant radicals are un-protonated even in highly acidic solutions (Jiang et al., 1992).

For most kinetic experiments with PCE, 1.3 mL of the saturated PCE stock was added to 40 mL of un-buffered deionized water in a VOA vial with a Mininert<sup>®</sup> valve. After the solution was heated to the desired temperature, 1 mL of  $0.019 \text{ M Na}_2S_2O_8$  was added, and the syringe plunger was flushed 3 times to mix the contents of the vial. At this point, there was little to no headspace in the vials (<0.5 mL), and the concentrations of PCE and Na<sub>2</sub>S<sub>2</sub>O<sub>8</sub> should have been  $4.5 \times 10^{-5} \text{ M}$  and  $4.5 \times 10^{-4} \text{ M}$ , respectively.

Experiments with *cis*-DCE and *trans*-DCE were done with higher initial concentrations (0.002 M) due to the lower sensitivity of the electron capture detector for these analytes. These experiments were carried out in 0.020 M Na<sub>2</sub>S<sub>2</sub>O<sub>8</sub>, to keep the proportions constant at 10:1. Experiments with TCE were prepared at the same concentrations as those for the DCE's. In all other aspects, experiments with TCE, *cis*-DCE, and *trans*-DCE were set up like those with PCE. For all four chlorinated ethenes and all five temperatures studied, at least one control experiment in which 1 mL of water was added instead of 1mL of Na<sub>2</sub>S<sub>2</sub>O<sub>8</sub> stock solution was conducted at each temperature to show that disappearance of the parent compounds was due to reaction with activated persulfate and not autoxidation, hydrolysis, volatilization, adsorption, or leakage.

A series of experiments with PCE was conducted in the presence of carbonate, mainly to determine the degree to which carbonate suppresses contaminant degradation rates by radical scavenging. In most respects these experiments were the same as those described above, but they were prepared with three concentrations of sodium bicarbonate (100, 300, and 500 mg L<sup>-1</sup>) and were run at three temperatures (30, 50, and 70°C). In all cases, the initial pH of the bicarbonate solution was measured at 50 and 70°C. The pH was also measured at the end of each experiment, and at 30°C. The pH was measured at each sampling event by inserting a needle-form combination pH electrode (Microelectrodes, Inc., Bedford, NH) into the vial through an enlarged hole in the Mininert valve.

Concentrations of the chlorinated ethenes and volatile byproducts were determined by analysis of headspace samples using gas chromatography (HP 5890) with a 30 m x 0.32mm Econo-cap 1 column (Alltech) and electron capture detection, with helium as the carrier gas. The oven temperature was 40°C for all the ethenes except PCE, for which the oven temperature was 80°C. For PCE and TCE, the headspace samples were made by injecting 20  $\mu$ L or 100  $\mu$ L, respectively, of reaction mix from the experiment vial into a crimped 60 mL vial containing 30 mL of water. The vials were shaken vigorously, and 0.5 mL of nitrogen gas was added to the vial before removing 0.5 mL of sample for analysis. Because of the lower sensitivity of the dechlorinated ethenes, the headspace analysis was done by inserting 100  $\mu$ L of the reaction mix from the experiment vial into a crimped 10 mL vial. The vials were shaken vigorously, and 0.5 mL of nitrogen gas was added to each vial before removing 0.5 mL of sample for analysis. Chloride concentrations were analyzed by ion chromatography (Dionex IC-25) with an Alltech Allsep 2 column. A buffer of 2.1mM NaHCO<sub>3</sub> and 1.6mM Na<sub>2</sub> CO<sub>3</sub> was used at a flow rate of 2 mL/min.

**Persulfate and Sulfate Analyses.** Aqueous concentrations of persulfate were determined by spectrophotometric analysis using iodine oxidation according to the method from (Frigerio, 1963). Sulfate concentrations were measured by the barium chloride turbidometric method using Hach<sup>®</sup> reagents.

**Batch Tests.** Persulfate decomposition was studied with batch experiments in 40 mL septum-cap vials incubated in 30, 50, and 70°C constant-temperature baths. Most experiments were started with 5 mM Na<sub>2</sub>S<sub>2</sub>O<sub>8</sub> (Aldrich Chemical, 98+), but 0.1, 1.0, 10, and 100 mM were also used. These and all other solutions were prepared with air-saturated deionized water. The batch experiments with carbonate contained 100, 300, and 500 mg/L NaHCO<sub>3</sub> (EM Science, reagent grade). Batch tests with soil (medium grained Columbia River sand of basaltic origin with an organic carbon content of~0.3% by weight) were prepared by mixing 20g of soil with 20mLof 5mM persulfate solution (i.e., soil concentration ~ 1 g/mL). Reaction progress for most of these experiments was monitored by measuring sulfate concentrations, although persulfate concentrations were measured in some cases.

**Re-spike Experiments.** Re-spike experiments were performed in 40mL septum-cap vials containing 20 g of soil and 30 mL of 0.1, 1, 10, and 100 M Na<sub>2</sub>S<sub>2</sub>O<sub>8</sub> (i.e., soil concentration ~0.67 g/mL). These vials were gently mixed by rolling on a tipping tray in a water bath at 70°C. Water samples were periodically withdrawn from each vial and analyzed for persulfate. After 24 h, each vial was re-spiked with persulfate at the same concentration as in the first spike. This process was repeated six times.

**Oxidant Demand.** To provide an initial value of the soil's natural oxidant demand (NOD) for modeling the re-spike experiments, we determined NOD using permanganate (ASTM, 2007). Thirty mL of a 0.63 mM KMnO<sub>4</sub> solution (Sigma-Aldrich, ACS Reagent grade) was added to vials containing 0, 1, 3, 10, and 30 g of soil and allow to react for 24 h with gentle shaking at 70°C. The change in permanganate concentration was determined from the decrease in absorptivity at 550 nm. The mass of permanganate reacted was then used to calculate the reducing equivalents per gram of soil, assuming three equivalents per permanganate ion.

#### **SECTION 4. RESULTS AND DISCUSSION**

## 4.1. LOW-TEMPERATURE ERH, SUBSURFACE FLOW AND TRANSPORT IN HOMOGENEOUS MEDIA<sup>1</sup>.

#### **4.1.1.** Voltage and Power Measurements

The experimental and predicted power usage for the visualization tank with time is presented in Figure 4.1. Overall, the electro-thermal model simulations showed good agreement with the experimental power. However, the peak power in the experimental tank, when 30°C and 50°C was reached was slightly underestimated by the model. The time to reach these temperatures was also slightly underestimated. In addition, the heat losses in the first part of the experiment were slightly overestimated by the model. Once the temperature reached 50°C, higher heat losses were observed due to the higher temperature differences between the tank and outside temperatures. At the end of the experiment, the predicted power for the small tank was similar to the experimental observations (46 W compared to 47 W) and the total energy predicted for the entire experiment was 866 kJ, compared to the actual 888 kJ supplied by the electrodes, which corresponds to a 2% error.

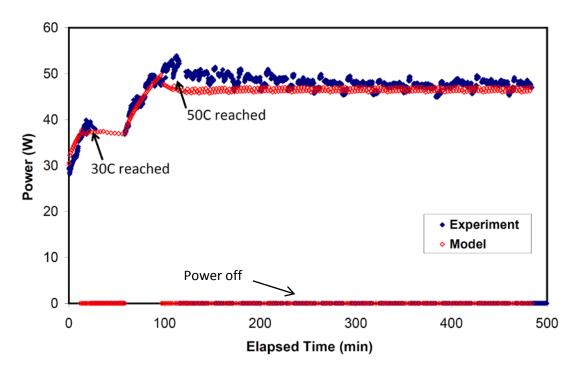


Figure 4. 1. Experimental and modeled power results for LTERH in the visualization model.

<sup>&</sup>lt;sup>1</sup> Most of the material in this section came from our publication Krol et al., 2011.

## 4.1.2. Temperature

Figure 4.2 shows the predicted and experimental temperature distribution of the visualization tank 1.5 and 3 hours after start of tracer injection (this corresponds to 3.5 and 5 hours of heating). The simulated temperatures in the heated zone showed good correspondence with the experimental results. The largest deviation between observed and simulated temperatures was seen in the upper part of the tank, where the model underestimated the temperatures by approximately 9°C. The temperatures simulated near the electrodes were approximately 12°C higher than the cut off temperature of 50°C which was expected since the thermocouples that served the temperature control, were not located at the electrodes.

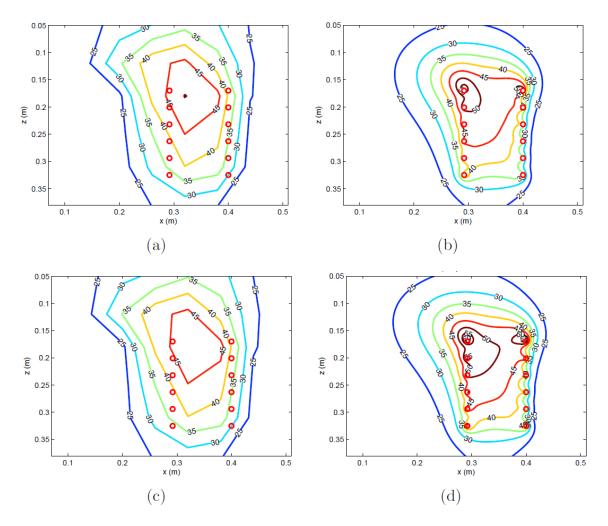


Figure 4. 2. Comparison of experimental and modeled temperature distributions in the visualization experiment. Red circles indicate electrode positions. a) experiment at 1.5 hours; b) model at 1.5 hours; c) experiment at 3 hours; and d) model at 3 hours.

## 4.1.3. Tracer Study

Photographs of Rhodamine WT tracer distribution in the visualization physical model at 1.5 and 3 hours are shown in Figures 4.3a and 4.3c. The isothermal tracer experiment was simulated and the model results shown in Figures 4.3b and 4.3d are in good agreement with the experimental data. The measured non-isothermal tracer distributions at 1.5 and 3 hours after tracer injection are presented in Figures 4.3e and 4.3g, respectively. In both figures, the temperature around the electrodes was approximately 50°C. The observed flow pattern was distinctly different than the isothermal case, with strong buoyant flow throughout the heated region. In both figures, the top most tracer plume moved more slowly than the rest of the plumes due to a convective zone which developed in the region above the electrodes. Tracer movement was simulated for 1.5 and 3 hours after tracer injection and is presented in Figures 4.3f and 4.3h, respectively. Originally, the tank was modeled using isotropic hydraulic conductivities and low dispersion coefficients. This resulted in large dispersion within the heated zone and distinct tracer "fingers" were not visible. To address this issue, several techniques were examined. A midpoint weighing scheme was implemented and smaller vertical discretization was used to decrease numerical dispersion. This resulted in no significant improvement in the tracer profile. Subsequently, zero hydrodynamic dispersion as well as an anisotropy ratio of 0.7 for hydraulic conductivity was implemented. This resulted in more distinct tracer profiles for the 1.5 hour scenario, but the 3 hour tracer profile still showed more "smearing" than was observed in the experiment, especially in the upper tracer plumes.

These results suggested that the smearing was not a result of hydrodynamic dispersion but rather numerical dispersion, even at small grid discretization. Since the resulting groundwater flow in the heated section was diagonal to the finite difference grid, grid orientation effects associated with upstream weighting of the advection terms were determined to be causing the excessive spreading of the tracer plumes (Kozdon et al., 2008). Consequently, the velocities obtained by the electro-thermal model were exported into a modified version of MT3DMS (Xheng, Wang, & Zheng, 1999). The ULTIMATE scheme (a total variation diminishing (TVD) method) was used and resulted in distinct tracer plumes for both time scenarios. A dispersivity of 0.1 mm was used in the longitudinal and transverse directions. The model also captured slower and more dispersed tracer movement down-gradient of the upper tracer injection point. The buoyant flow in the heated zone developed due to the difference in density of 1.3%. In addition, a decrease in viscosity of 40%, as well as the change in density, resulted in increased velocities within the heated zone to on the order of 5.2 x 10<sup>-5</sup>m/s, almost 5 times faster than the isothermal velocity.

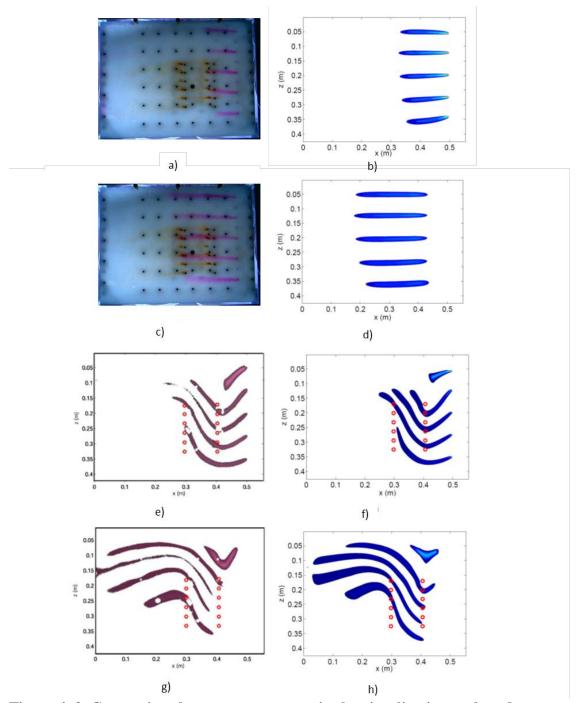


Figure 4. 3. Comparison between tracer tests in the visualization tank and corresponding model results. a) photograph of tracer tests ~1.5 hrs after startup; b) model results at 1.5 hrs; c) photograph at 3 hours; d) model results at 3 hours, all for the isothermal experiment. For the  $50^{\circ}$ C heating experiment: e) processed image at 1.5 hrs; f) model results at 1.5 hrs; g) processed image at 3 hrs; h) model results at 3 hrs.

#### 4.2. HEAT AND MASS TRANSPORT IN HETEROGENEOUS MEDIA

### 4.2.1. Heating Up-Gradient of the Target Zone

In the homogeneous-media experiments discussed above we demonstrated that significant buoyancy occurred when a portion of the porous media was heated to 50°C. Thus, if contaminant source zones can be heated, this could be a strategy for enhanced flow and dissolution of the contaminants. However, many dense non-aqueous phase liquid (DNAPL) sources – e.g., pools of chlorinated solvents – are found just above geologic strata with lower hydraulic c. In addition, placement of electrodes within source zones is risky because the emplacement process can lead to downward mobilization of the DNAPL, which can exacerbate problems with remediation.

One scenario is to heat the water just up-gradient of the source and let the heat flow through the target zone. Figure 4.4 shows results of a physical model experiment where this approach was used. Figure 4.4a shows the locations of the electrodes (solid black circles) relative to the treatment zone, as well as voltages throughout the experimental domain. Under steady-state conditions, measured AC voltages ranged from 45 (blue) to 75°C (red). The resulting steady-state temperature distribution is shown in Figure 4.4b. Measured temperatures ranged from 21 (blue) to 66°C (red).

Once steady-state conditions were achieved, tracer pulses were released from 7 ports upgradient of the treatment and heating zones. Figure 4.4c shows the migration of those pulses through the model. Each color represents a different time snapshot and the white lines indicate the approximate flow paths for each of the tracer pulses.

The data indicate that water flow just up-gradient of the heating zone dipped and then rose as it moved through the heated zone. The water near the sand-clay interface (i.e., within the treatment zone) then dipped again. While the velocity of the lowest tracer plume was initially much faster than at locations higher in the model, the velocity then slowed and the overall velocity within the treatment zone was similar to most of the other tracer locations in the model. This indicates that, in this case, there would be little enhancement of the dissolution process

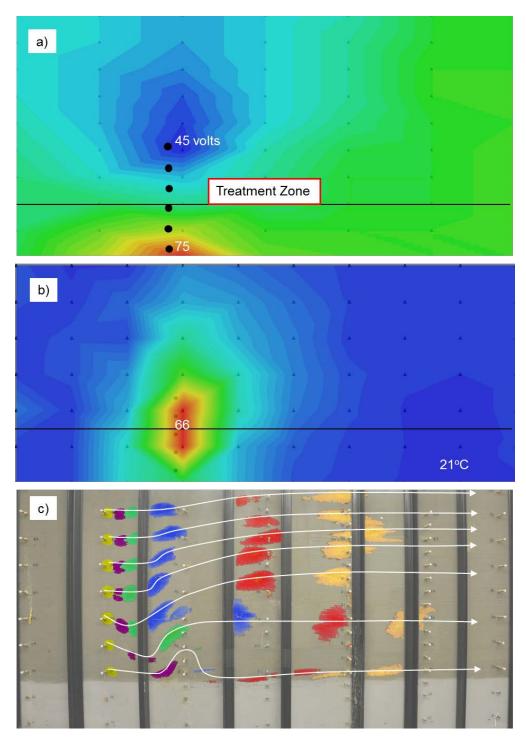


Figure 4. 4. a) Electrode locations (solid black circles) and measured voltages; b) measured temperatures under steady-state conditions; and c) composite photograph showing snapshots of tracer plume movements for heating up-gradient of the treatment zone.

### 4.2.2. Heating Beneath the Target Zone

In many cases the electrical conductance of lower-permeability layers is significantly greater than that of adjacent aquifers. As a consequence, it is possible to selectively heat the lower-permeability layers with ERH (especially if electrodes are only in contact with those layers). This situation was simulated in the physical model by placing 9 electrodes in the clay beneath the treatment zone (only the upper 6 are shown in Figure 4.5a)

In many cases the electrical conductance of lower-permeability layers is significantly greater than that of adjacent aquifers. As a consequence, it is possible to selectively heat the lower-permeability layers with ERH (especially if electrodes are only in contact with those layers). This situation was simulated in the physical model by placing 9 electrodes in the clay beneath the treatment zone (only the upper 6 are shown in Figure 3a). As in the previous experiment, steady state voltages (8-101) and temperature (21-51°C) are shown in Figure 4.5. Figure 4.5c shows time snapshots and the paths of 6 tracer pulses injected under those conditions. In this case, in part due to the lower temperature, there was less buoyancy than in the previous case. However, the velocity of the groundwater through the treatment zone was approximately twice the value of the up-gradient heating case.

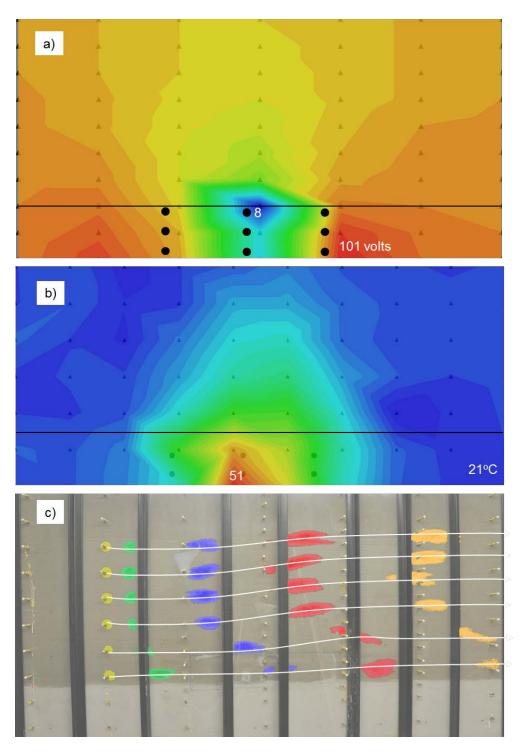


Figure 4. 5. a) Electrode locations (solid black circles) and measured voltages; b) measured temperatures under steady-state conditions; and c) composite photograph showing snapshots of tracer plume movements for heating beneath the treatment zone.

## 4.2.3. Dissolution from a DNAPL Source while Heating Upstream

To directly evaluate the impact of heating upstream of a DNAPL source zone,  $\sim$ 120 mL of TCE was released into the heterogeneous model through a 0.5-inch diameter stainless steel tube with a perforated end (shown as the blue object in Figure 4.6). The average groundwater in the model was maintained at  $\sim$ 100 cm/day. Following the release, groundwater was allowed to flow through the model for a period of 10 days while the temperature of the model was maintained at  $\sim$ 20°C



Figure 4. 6. Photograph showing the PCE DNAPL source zone created in the heterogeneous tank and used for the dissolution experiment. The blue rectangle represents the approximate location of the perforated portion of the injection tube.

The concentration of TCE in the effluent was measured every ~2 days during that period (Figure 4.7.) In addition, the concentration directly down-gradient of the source was measured and was consistently near the solubility limit of TCE (1700 mg/L). After 10 days the vertical array of 6 electrodes (Figure 4.4.a) were used to heat the portion of the aquifer up-gradient from the TCE to 50°C. The concentration data in Figure 4.7 indicate that there was some increase in effluent concentration, but that the increase was probably less than a factor of two (i.e., from ~60 to ~100 mg/L). When the temperature was increased to 75°C, the effluent concentration appeared to decrease.

The temperature data in Figure 4.8 suggest that the heated zone reached a final temperature of only ~35°C. Perhaps more important is that water flowing through the heated zone moved upward due to buoyancy. As a consequence, the volume of water flowing through the source zone may have actually decreased. Given that the solubility should have stayed

constant or increased slightly (Knauss et al., 2000), the decrease in concentration supports the idea that buoyancy was causing the source zone to be bypassed.

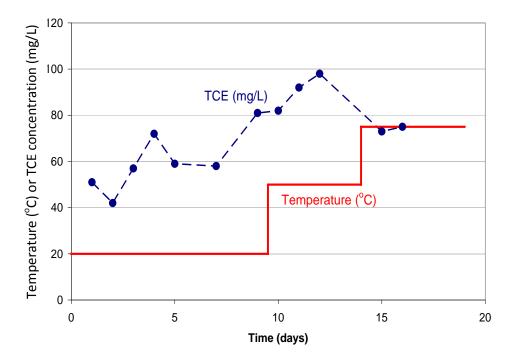


Figure 4. 7. Effluent concentration and temperature program for the TCE dissolution experiment.

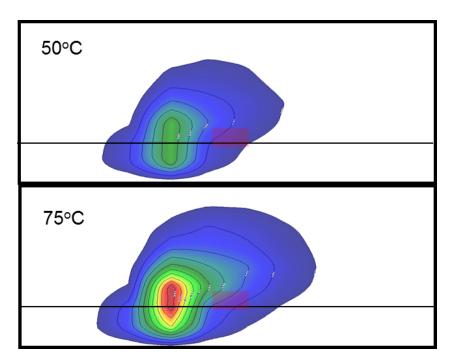


Figure 4. 8. Steady-state temperature profiles at 50 and 75°C during the TCE dissolution experiment. The pink rectangle in each figure corresponds to the approximate location of the TCE source.

### 4.2.4. Numerical Modeling of Voltage and Power in the Heterogeneous Tank

The large tank was used to assess the capability of the model to simulate voltage distribution in a 2D system with different soil layers. Voltage in the large tank was measured at the start of the experiment and when the experiment reached steady state temperature. The experimental voltage distribution is presented in Figures 4.9a and 4.9c. The largest difference between the initial and final voltage is seen at the bottom of the tank, where higher clay electrical conductivity values led to higher voltage values. This also resulted in higher temperatures in the clay zone. The results of the modeled initial and final voltage contours are presented in Figures 4.9b and 4.9d. The model predicted the experimental voltage with good accuracy and, similar to the experiment, also predicted an increase in the final voltages in the clay zone.

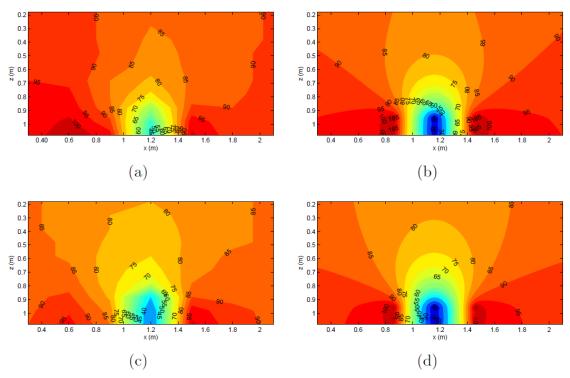


Figure 4. 9. Voltage distribution in the large tank: a) initial experimental voltage; b) initial modeled voltage; c) final experimental voltage; d) final modeled voltage.

Power consumption during the heating of the large physical model is shown in Figure 4.10. The blue points are measured power, the red points are modeled values. The points at the bottom of the represent periods during which the control system switched the power off to regulate temperature. The difference in total electrical energy input over the course of the large tank experiment was calculated to be 8%.

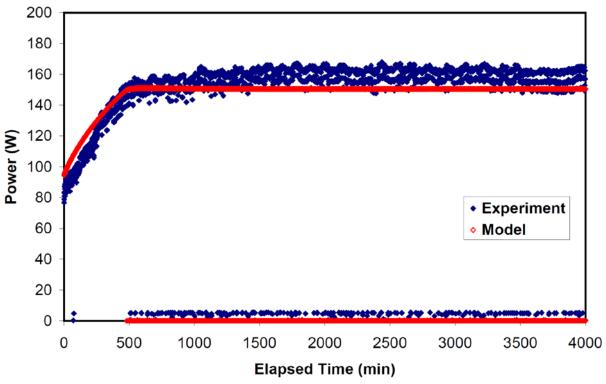


Figure 4. 10. Power consumption during heating of the large physical model. Blue points represent measured values, red points represent modeled values.

## 4.2.5. Simulation of Heating, Flow and Transport in Heterogeneous Media

The combination of physical and numerical modeling of simple systems described above resulted in a calibrated model that can be used to evaluate more complex (i.e., realistic) remediation conditions. This section describes application of the coupled electro-thermal flow and transport model to two well-characterized heterogeneous aquifer systems. To quantify the effects of heterogeneity on heating, groundwater flow and mass transport in the subsurface, two aquifers with different soil permeability distributions were considered: the Borden aquifer (Sudicky, 1986); and a sand and gravel aquifer located in the northeastern part of Switzerland (Jussel et al., 1994). The two aquifers had similar mean values and distributions of permeability but the variance of permeability was higher for the Swiss aquifer. Both aquifers were simulated with different initial bulk electrical conductivities and applied groundwater fluxes

The effect of aquifer heterogeneity on fluid flow and transport has been well established in the literature (Dekker & Abriola, 2000; Sudicky, 1986; Woodbury & E. Sudicky, 1991). The distribution of permeability has been described by a normal or exponential distribution (ln(k)) (Sudicky, 1986; Woodbury & E. Sudicky, 1991). Permeability also has a strong spatial correlation structure due to the manner that soil layers were deposited, leading to larger correlation lengths in the horizontal rather than vertical direction (Dekker & Abriola, 2000).

The power dissipated by ERH is directly dependent on the bulk electrical conductivity  $(\sigma_b)$ . EC is dependent on the saturation  $(S_w)$ , pore water EC  $(\sigma_w)$  and porosity  $(\phi)$  as described by Archie's law (Archie, 1942):

$$\sigma_b = \phi^m S_w^n \sigma_w \tag{4.1}$$

where m is the cementation exponent ranging from 1.3 to 1.5 for clean sands and n is the saturation coefficient, typically taken to be 2 (Butler & Knight, 1998).

Pore water EC changes with temperature and salinity (Sen et al., 1988). Therefore, bulk EC can vary depending on the soil type as well as the subsurface conditions. Although many studies have shown that electrical conductivity can vary substantially (Butler & Knight, 1998; Henry, 1997; McNeill, 1980; Sen & Goode, 1988; Waxman & Smits, 2003), the effect of electrical conductivity on energy and mass transport during ERH is not fully understood. In addition, operators of ERH have claimed that ERH will preferentially heat more conductive soil such as silts and clays (Beyke & Fleming, 2005) but a quantitative analysis of the effect of EC on heat and mass transport has not been performed. Groundwater velocities can vary extensively depending on the porous medium. Although it is expected that groundwater velocity will impact heat and mass transport, different applied groundwater fluxes were considered in this study to examine if higher variance in soil permeability will obscure the effect of groundwater velocities. In addition, the onset of buoyant flow will depend on the buoyancy ratio which is affected by the groundwater velocity. Therefore, by examining variable velocities, the effect of buoyant flow on mass and energy transport was also investigated.

### 4.2.6. Parameters Used to Characterize Heat and Mass Transport

For each aquifer, random fields of permeability were generated using the Field Generator in PMWIN (Chiang, 2005) which uses Mejia's algorithm (Frenzel, 1995; Mejia & Rodriguez-Iturbe, 1974). By generating numerous permeability realizations and observing how the heat and mass distribution changes, a view of the "average" heating and mass transport behavior was examined. To interpret the model output and quantify the movement and shape of heat and mass distributions, several heat and mass parameters were used. These parameters were based on the investigations by Dekker & Abriola (2000) and modified for this study. The horizontal center of energy was calculated by:

$$x_{ce} = \frac{1}{E} \int x de \tag{4.2}$$

where E is the total energy of the system, x is the distance in the x direction, and de is the incremental portion of energy. The vertical center of energy was calculated similarly in the z direction. The spreading of heat was measured using the radius of gyration:

$$x_{spread}^e = \sqrt{\frac{I_z^e}{E}} \tag{4.3}$$

where  $I_z^e$  is the second moment of energy about the z-axis and is defined as:

$$I_z^e = \int x^2 de \tag{4.4}$$

where *x* is the distance from the z-axis. The spread of energy in the z direction was also calculated using equation 4.4, but using the second moment of energy about the x-axis. These parameters are represented in Figure 4.11.

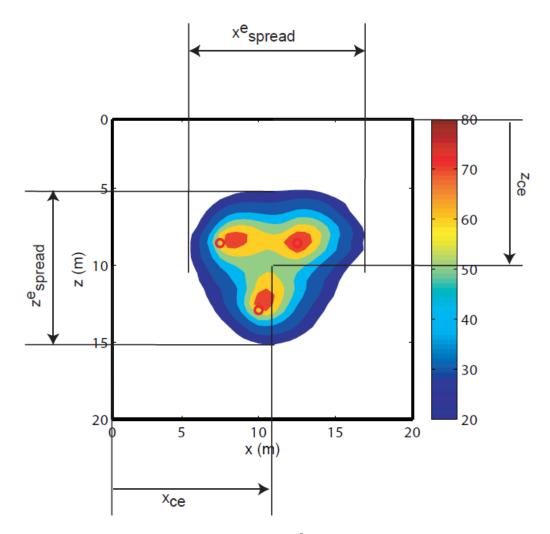


Figure 4. 11. Temperature contours  $(20-80^{\circ}C, scale on right of figure)$  and energy parameters used to quantify the movement of energy.

To quantify the shape and movement of the mass distribution, similar parameters were used. The horizontal center of mass was calculated using:

$$x_{cm} = \frac{1}{M} \int x dm$$

[4.5]

where *M* is the total mass of the system, x is the distance in the x direction, and dm is the incremental portion of mass. The spreading of mass was measured in a manner similar to the energy, where the radius of gyration for mass was defined as:

$$x_{spread}^{m} = \sqrt{\frac{I_z^m}{M}}$$
 [4.6]

and where  $I_z^m$  is the second moment of mass about the z axis and is defined as:

$$I_z^m = \int x^2 dm \tag{4.7}$$

where *x* is the distance from the z-axis. The vertical mass parameters were similarly calculated. The last parameter that was used to examine the effect of heterogeneity on mass distribution was the maximum concentration in the subsurface at the time of the analysis.

## 4.2.7. Simulation Description

The ETM model was used to simulate ERH in a vertical slice of an aquifer, presented in Figure 4.12. The top and bottom heat and mass boundary conditions were assumed to be zero flux. A constant flow boundary condition was used on the left side of the domain (i.e., a known flux specified at a reference temperature (20°C)). A constant head boundary was used on the right hand side. All voltage boundary conditions were set to zero flux. ERH was modeled using three electrodes spaced at a radius of 4 m, with an applied voltage of 400 V. An initial concentration of 1000 mg/L of trichloroethylene (TCE) was specified in the center of the heated zone (Figure 4.12).

The model simulated 50 days of heating to 80°C but the statistical analysis was performed after 10 days of heating in order to ensure the entire mass and energy plumes were within the simulated domain. The Borden aquifer was used as a base scenario using properties obtained from Dekker & Abriola (2000), presented in Table 4.1. The Borden aguifer was selected as the base case because it is well characterized and relatively homogeneous (Dekker & Abriola, 2000; Sudicky, 1986). The Swiss aquifer was more heterogeneous but had similar mean permeability and correlation lengths as the Borden aquifer (Dekker & Abriola, 2000; Jussel et al., 1994). However, the variance of permeability was higher in the Swiss aquifer, resulting in higher contrast in permeability. The simulations were modeled using the layout shown in Figure 4.12. Realizations of permeability were generated using the Field Generator in PMWIN (Chiang, 2005) which used the vertical and horizontal correlation lengths, as well as, the log mean value and log standard deviation of permeability as the input values. The aquifer properties are shown in Table 4.1. One hundred realizations were generated for each aquifer and 20 realizations were chosen randomly for the analysis. The estimate of variance was calculated for different parameters and convergence of variance was observed to occur within 20 realizations, as shown in Figure 4.13.

Table 4. 1. Aquifer properties and simulation parameters.

	<u> </u>	Borden Aquifer	Swiss Aquifer	
$\phi$	Porosity $(-)^a$	0.34	0.34	
k	Average permeability $(m^2)^{b,c}$	$1.1 \times 10^{-11}$	$1.6 \times 10^{-11}$	
$\sigma$	Variance $(\log(k)) (-)^{b,c}$	0.2130	0.4343	
$\mu$	Mean $(\log(k))$ $(-)^{b,c}$	-11.01	-11.01	
$\boldsymbol{x}$	Horizontal correlation length $(m)^b$	5.1	5.1	
z	Vertical correlation length $(m)^b$	0.21	0.21	
$K_x$	Initial hydraulic conductivity $(m/s)^{b,c}$	$1.1 \times 10^{-4}$	$1.6 \times 10^{-4}$	
	Anisotropy factor $(-)^d$	0.5	0.5	
dx dz	Grid discretization $(m)$	0.5, 0.5		
$q_{in}$	Applied Groundwater Flux $(m/s)^e$	$1 \times 10^{-6},  2 \times 10^{-6},  3 \times 10^{-7}$		
$\sigma_b$	Bulk electrical conductivity $(S/m)^f$	0.02,  0.1,  0.2		
$C_o$	Initial TCE concentration $(mg/L)$	1000		

Sources: <sup>a</sup>Sudicky (1986) <sup>b</sup>Woodbury & Sudicky (1991) <sup>c</sup>Jussel et al. (1994) <sup>d</sup>Brown et al. (1994) <sup>e</sup>Sudicky et al. (1983) <sup>f</sup>Waxman & Smits (1968)

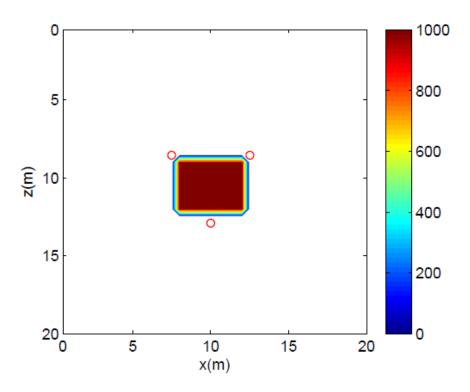


Figure 4. 12. Initial TCE aqueous concentration (mg/L) in a vertical slice of the subsurface. The red circles represent electrodes.

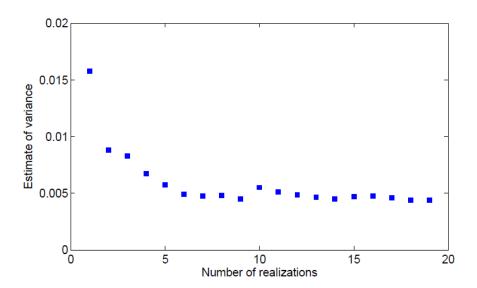


Figure 4. 13. Estimate of variance for the center of energy of the Borden aquifer.

The Swiss aquifer was modeled with the same mean permeability, correlation length, porosity, and electrical and thermal properties as the Borden aquifer but with a higher variance in permeability, resulting in larger contrasts in the permeability fields. Figure 4.14 presents a single realization of permeability for both aquifers as well as the resulting streamlines under isothermal conditions. Greater variability in the permeability contours was observed in the Swiss aquifer leading to more tortuous streamlines.

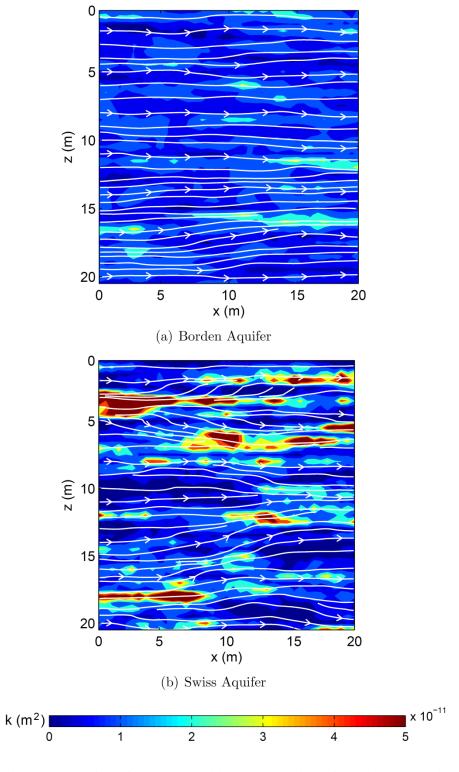


Figure 4. 14. Aquifer permeability distributions for a single realization and the corresponding streamlines.

Four realizations of mass distribution after 50 days of heating at 80°C are shown in Figures 4.15 and 4.16 for four different realizations for the Borden and Swiss aquifers, respectively. In all cases the contaminant plume moved both horizontally (e.g., the primary direction of groundwater flow) and vertically (as the result of buoyant flow.)

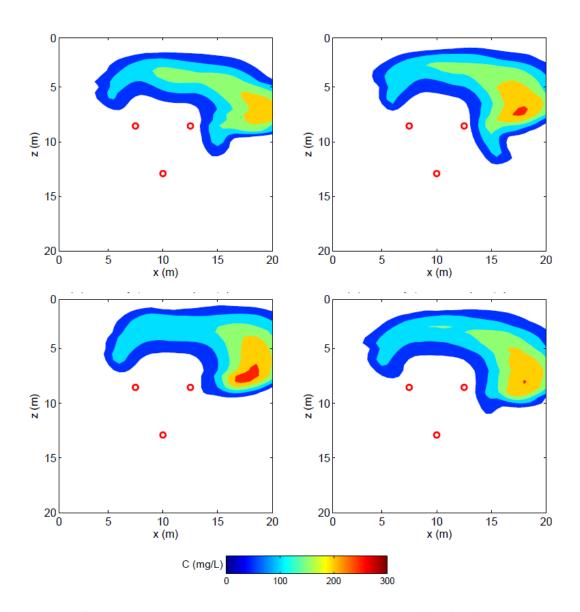


Figure 4. 15. Simulated concentration contours for Borden aquifer for four different soil permeability realizations after 50 days of heating to 80°C. Red circles represent electrode locations.

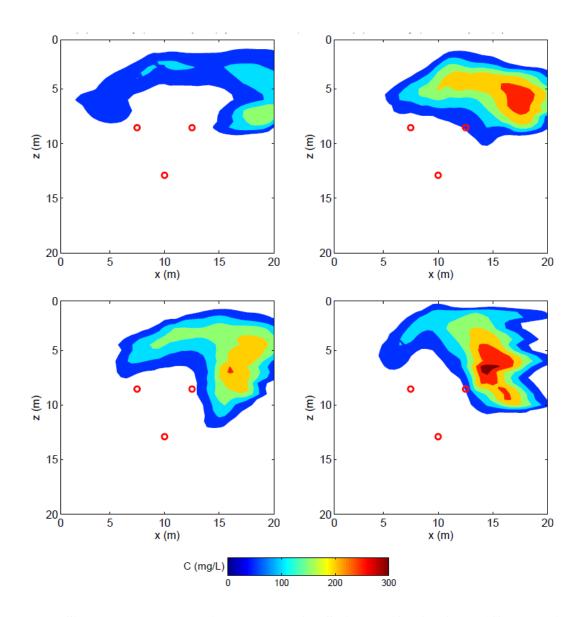


Figure 4. 16. Simulated concentration contours for Swiss aquifer for four different soil permeability realizations after 50 days of heating to 80°C. Red circles represent electrode locations.

The important effect of buoyant flow can be seen in Figure 4.17 which shows flow lines for the same permeability realization for the Swiss aquifer before and after heating to 80°C for 10 days. In the isothermal case, flow was preferentially directed through the high permeability zones. However as buoyant flow became established, the majority of the flow was directed

upwards rather than horizontally along higher permeability zones. The significance of the

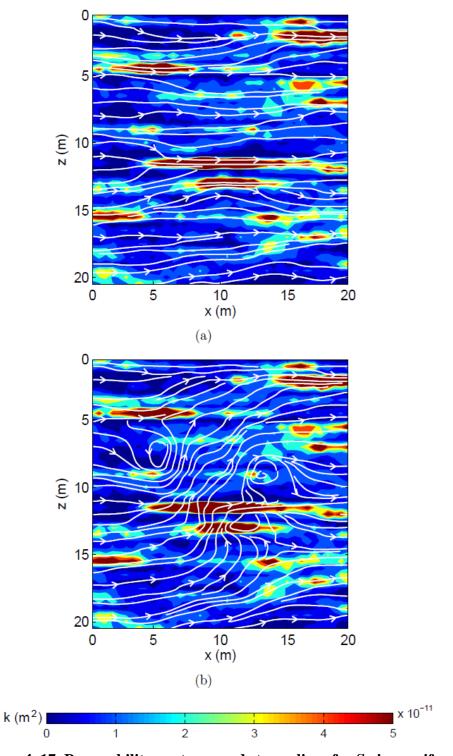


Figure 4. 17. Permeability contours and streamlines for Swiss aquifer a) before heating; b) after 10 days of heating.

vertical flow is perhaps best demonstrated by looking at the simulated DNAPL: distribution for the Swiss aquifer (Figure 4.18), that comes from Dekker and Abriola (2000). As the figure indicates, much of the DNAPL mass occurs in pools at the interface between high and low-permeability layers. Thus, as we observed in our simulations, if heating can significantly increase vertical flow through those zones, then mass transfer from the pools will be significantly increased.

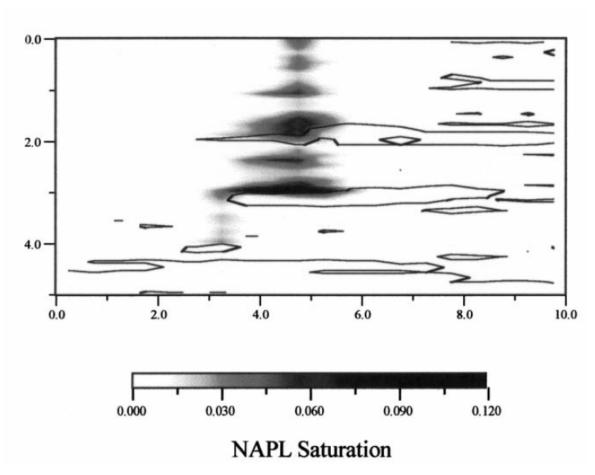


Figure 4. 18. Simulated DNAPL distribution in the Swiss aquifer from Dekker and Abriola (2000).

#### 4.3. BUBBLE FORMATION DURING LOW-TEMPERATURE ERH

To evaluate the effects of heating on bubble formation and movement, as well as the effect on water flow, experimental and numerical studies were carried out. The processes observed in the physical model experiments were quite complicated and a full numerical representation of them is not yet possible. However, the combination of the experimental observations and simulations still provide significant insight into the overall process.

# 4.3.1. 2-D Experiments with Heating and Bubble Formation

These experiments were conducted in the 2-D visualization tank. As described in Section 3.3, the water delivered to the tank was sparged with CO<sub>2</sub> prior to injection. Temperature profiles, recorded at approximately 3 minute intervals are presented in Figure 4.19. At the same time as the temperature data were collected, photographs of light transmitted through the tanks were taken. In order to determine the water saturation in each image, the red, green and blue (RGB) values from each pixel in the photos were converted to a luminosity measurement using equation [4.8]:

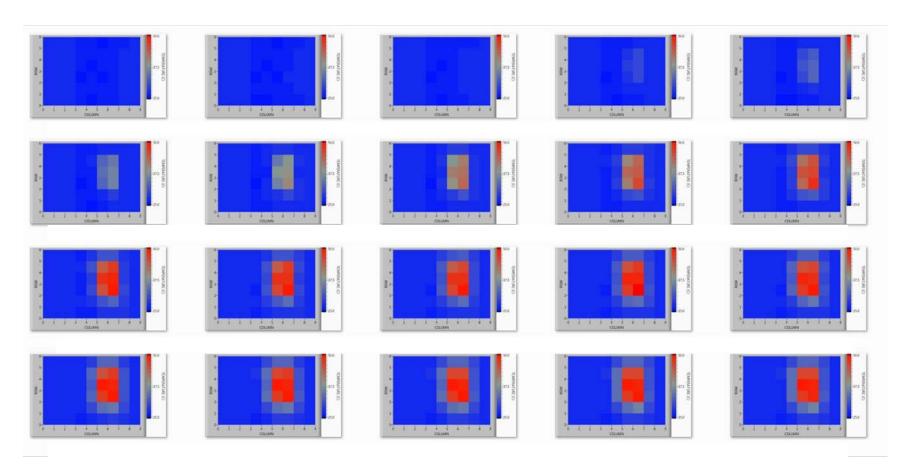


Figure 4. 19. Temperature profiles from the experiment measured at  $\sim$ 3 minute intervals during heating. Blue represents a temperature of 20°C and red is 50°C.

$$((\text{Red value X } 299) + (\text{Green value X } 587) + (\text{Blue value X } 114)) / 1000$$
 [4.8]

The resulting calibration curve for water saturation versus luminance is shown in Figure 4.20. Water saturation is calculated from the total porosity and residual saturation using the equation (sometimes called effective saturation):

$$S(eff)) = \frac{S - S(residual)}{1 - S(residual)}$$
 [4.9]

The normalized luminance is calculated using a similar equation:

$$L(eff)) = \frac{L - L(residual)}{1 - L(residual)}$$
[4.10]

As a result, both saturation and luminance should vary from 0 to 1 for the water contents that range from residual saturation to fully saturated. The experimental data in Figure 4.20indicate that this is the case.

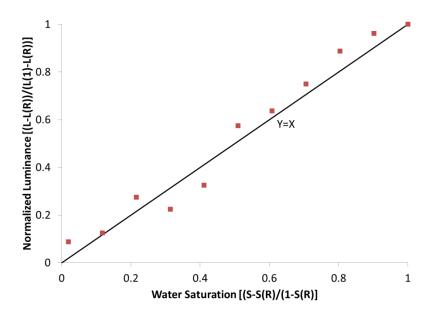


Figure 4. 20. Correlation between measured luminosity and measured water content for the visualization tank.

Using the data in Figure 4.20 (i.e., the equation Y=X), the average water saturation within the heated zone (white box in Figure 4.21) was calculated and is shown in Figure 4.22. The data indicate that water saturations dropped to about 60% over a ~40-minute period and remained at more-or-less that value. The temperature of the heated zone was held constant for ~1200 minutes, and there was no significant change in water saturation during that entire period.

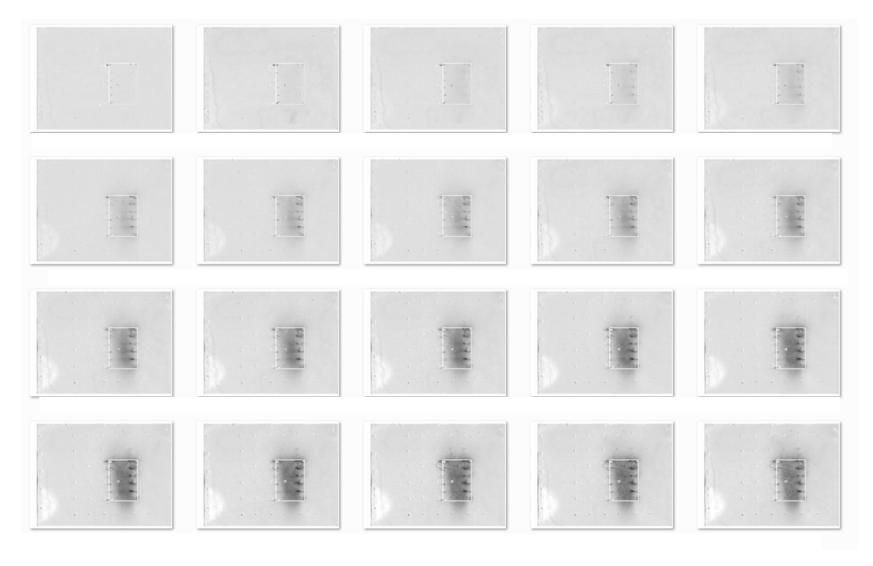


Figure 4. 21. Luminosity images converted from RGB images taken at times corresponding to the temperature snapshots in Figure 4.19.

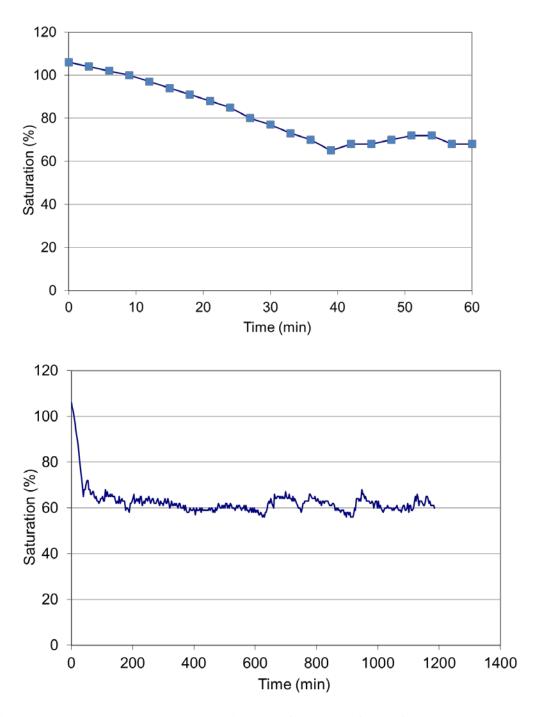


Figure 4. 22. Percent water saturation as a function of time for the heating case with  $CO_2$ -saturated water.

As will be discussed below, the lack of change in water saturation over time most likely occurs because the critical gas saturation (i.e., the maximum fraction of pore space occupied by gas before gas movement occurs) for the porous medium is in the range 0.35 to 0.4. As a result, if additional gas is produced within the heated zone it will move upwards and out of the zone. The luminosity data in Figure 4.21 suggest that could be happening in the later images. Nevertheless, the gas saturation remained high within the heated zone. As will be discussed next, this level of air saturation would be expected to result in a significant reduction in water permeability within that zone.

Reduction in water saturation to levels of 60-65% can dramatically reduce the hydraulic conductivity of the medium in that region (i.e., it will reduce the relative permeability for water) Several relationships between effective water saturation and relative permeability have been developed. The two most common of these are the Brooks-Corey and van Genuchten (e.g., Morel-Seytoux et al., 1996). Figure 4.23 shows the values of water relative permeability for water in a medium sand. As the figure indicates, as the air content increases (i.e., water saturation decreases) the relative permeability drops rapidly and, depending on the relationship used, is on the order of 5-10% of the fully-saturated value when 40% of the pore space is filled with air.

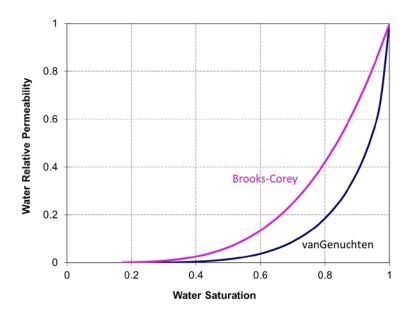


Figure 4. 23. Plots of relative permeability as a function of water saturation for the Brooks-Corey and van Genuchten equations.

However, these relationships were not developed for a system similar to the one described here (i.e., exolution of bubbles due to supersaturation), and as a result there is considerable uncertainty with regard to which relationship is appropriate for this case. Fry, Selker, & Gorelick (1997) examined a number of different gas emplacement mechanisms; however, none of those cases exactly match our case either.

A key issue in determining the overall effect of the trapped gas is the amount of gas that can be retained in the formation and the relative permeability at that saturation. As discussed above, if water continues to flow into a heated zone, the gas volume can continue to increase. However, at some point the gas bubbles begin to aggregate and become of sufficient size that they will move upward due to buoyancy. If this occurs then, as the experimental data suggest, the saturation may stabilize at that value. If the relative permeability is greater than zero at that point, some sustained upward movement of gas could result.

## **4.3.2.** Tracer Test Following Heating and Bubble Formation

To evaluate the extent to which bubble formation due to heating can be important for groundwater flow, a physical model experiment was conducted in our "visualization" tank. As with the previous heating experiment, Rhodamine WT was injected into the physical model at 5 locations near the up-gradient edge of the model. As the false-color images in Figure 4.24 indicate, movement of the tracer for the ~4 hours following injection was much different than for the case where bubbles were not present (data from the previous experiment where bubble formation was minimized by sparging the influent water with helium are shown in Figure 4.25 for convenience). The data indicate that movement of the tracer essentially stopped, suggesting that the relative permeability at a saturation of ~0.65 was essentially zero. However, at present, the data necessary to simulate the tracer experiment are not available, and as a result, modeling of flow is difficult because of uncertainty in the "balance" between upward bubble migration and permeability loss. Nevertheless, it is useful to model how bubble formation occurs as a first step towards understanding the overall process. To accomplish this, we conducted a number of numerical modeling simulations using the macroscopic invasion percolation (MIP) model, which is discussed in the following section.

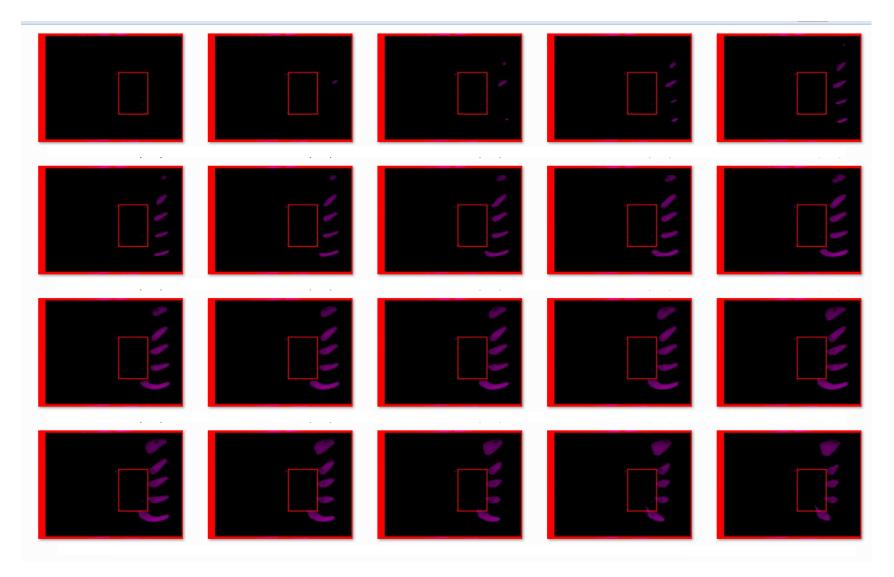


Figure 4. 24. False color images showing the tracer distribution at  $\sim\!20$  minute intervals.

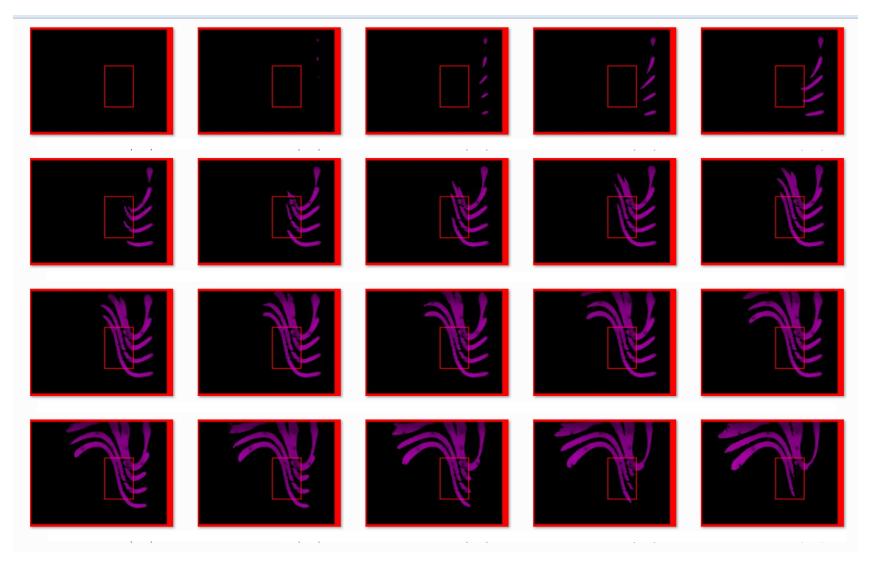


Figure 4. 25. False-color images of tracer distribution for the "no-bubbles" case discussed in Section 4.1.

## 4.3.3. Numerical Modeling of Bubble Movement

As mentioned above, a key parameter in controlling the behavior of the bubbles is the maximum saturation. That is, if the medium can retain enough bubbles to reduce the relative permeability of water to near zero, then a stable non-flowing situation will result. If, on the other hand bubbles begin to migrate upwards at a lower volumetric content (and when the relative permeability of water is still significant), then water flow will continue through that zone. As water continues to move into that zone and outgas bubbles, the bubbles will move upward. In general terms, it has been observed that the upwardly mobilized pathways will be relatively widely spaced and have a relatively minor impact on bulk groundwater flow (Ye et al., 2009). This is unlike the case within a heated zone discussed above where exsolution of bubbles can significantly reduce flow. However, the effect of upwardly mobile bubbles is an important one in the context of mass transport away from source zones, and is discussed further below.

The vapor pressures of volatile organic contaminants (VOCs) increase with increasing temperature. However, unlike most gases, solubility of VOCs also increase with temperature. As a result, bubble formation is controlled by the temperature-dependent Henry's gas constant, which is essentially the ratio of vapor pressure to solubility. For an organic species present at concentrations below saturation values, the vapor pressure of that species is given by:

$$P = C_w H ag{4.11}$$

In the following section, a conceptual model of bubble formation and movement resulting from a single species VOC is simulated. The simulations presented below were completed by combining the two-dimensional electro-thermal model (ETM) discussed above and a macroscopic invasion percolation (MIP) model. The MIP technique is based on the model of Mumford et al. (2010) and modified for non-isothermal conditions. Therefore, the model applied the same assumptions as Mumford et al., (listed below) as well as those related to a heated subsurface:

- (1) local equilibrium between the aqueous and gas phases
- (2) aqueous flow is not significantly affected by local changes in gas saturation
- (3) gas phase expansion occurs as a quasi-static displacement and gas movement occurs during the MIP step only; no advection or diffusion of the gas phase in the ETM mass transport step
- (4) gas phase mobilization occurs much faster than expansion or dissolution, such that mass transfer between gas and aqueous phase during a mobilization (MIP) step is negligible
- (5) thermal equilibrium exists between water and gas phases.

As discussed previously, the ETM model used finite differences to discretize the current, mass, flow and energy equations spatially and temporally, using a backwards difference, block-centered approach. The model used a fully implicit method for the temporal discretization of the current, energy, flow and mass transport equations. Since the heat and flow equations were coupled through temperature dependence of water properties, an iterative approach was used to calculate both the temperature and velocities in the system. Parameters that changed spatially

were averaged between grid blocks, using the harmonic mean value. These parameters included the hydraulic conductivity, water density, and electrical conductivity.

The ETM-MIP model assumed that aqueous transport, gas phase formation, expansion and movement occurred within the same time step. Each time step was divided into four distinct modules: electrical; thermal and flow; mass transport; gas movement. During the electrical module, the voltage and heat generated during ERH was calculated and used in the thermal and flow module to calculate the temperature distribution and velocity fields. Also within the thermal and flow module, all the temperature dependent variables were calculated. These included the Henry's coefficient, water vapor pressure, water density and viscosity, and hydraulic conductivities. New gas saturations were obtained through equilibrium calculations which were in turn used to calculate new total pressures and aqueous phase concentrations. These concentrations were used in the mass transport module, where the aqueous mass was transported according to the advection-dispersion equation. The gas movement module identified gas clusters and determined whether the bubbles mobilized or expanded using a MIP algorithm, as described by Mumford et al. (2010). Equilibrium calculations were performed after each mass transport and gas movement step.

Equilibrium between aqueous and gas phase for one organic species was established using Henry's law, Dalton's law and Ideal Gas Law:

$$C_g = x_g P_q^{tot} / RT ag{4.12}$$

$$C_w = C_q / K ag{4.13}$$

$$P = C_w H ag{4.14}$$

$$S_a + S_w = 1 ag{4.15}$$

$$\sum x_g = 1 \tag{4.16}$$

$$\sum x_g = 1$$

$$\sum x_w = 1$$
[4.16]
$$[4.17]$$

$$P_g^{tot} = \sum P = P_c + P_w \tag{4.18}$$

The subscripts g and w refer to gas or water phase, respectively; C is the concentration of the volatilizing specie; x is the molar fraction;  $P_g^{tot}$  is the total gas pressure; P is the partial pressure; T is the subsurface temperature; R is the ideal gas constant; K is the partition coefficient of volatilizing specie; H is the Henry's coefficient; S is saturation;  $P_w$  is the water pressure; and  $P_c$ is the capillary pressure. For a two species system (water and one dissolved species), the total

gas pressure consisted of the water vapor pressure  $(P_w^v)$  and the partial pressure of the volatile specie, written in terms of the Henry's coefficient (equation 4.14):

$$P_g^{tot} = P_w^v + C_w H = P_c + P_w$$

$$C_w H = P_c + P_w - P_w^v$$
[4.19]

$$M = M_g + M_w$$

$$M = C_g S_g \phi + C_w (1 - S_g) \phi$$

$$M = K C_w S_g \phi + C_w (1 - S_g) \phi$$

$$(4.20)$$

Using these relationships the total mass of volatile species in the system was written where  $\varphi$  is the porosity. Equations [4.19] and [4.20] were combined to give:

$$M = K \left( \frac{P_w + P_c - P_w^v}{H} \right) S_g \phi + \left( \frac{P_w + P_c - P_w^v}{H} \right) (1 - S_g) \phi$$
 [4.21]

where the capillary pressure is a function of gas saturation as described by the Brooks-Corey relationship:

$$P_c = \left(\frac{1 - S_g - S_{wr}}{1 - S_{wr}}\right)^{-\frac{1}{\lambda}} P_d \tag{4.22}$$

The MIP model is a modified form of the invasion percolation (IP) technique which has been used extensively to model fluid displacement processes in the subsurface (Glass et al., 2001; Kueper & McWhorter, 1992). IP and MIP techniques use invasion and drainage thresholds to control the fluid movement, however whereas IP represents the porous medium by a network of sites and bonds, MIP models the domain with sites only. In addition, MIP differs from IP because the sites represent a sub-region of the medium (as opposed to an individual pore) and they can be occupied by multiple fluids (Kueper & McWhorter, 1992). Similar to Mumford et al. (2010), this study used the capillary pressure - saturation relationship (equation 4.22), to model the occurrence of two fluids (water and gas) within one site.

In the model, a gas bubble formed once the average gas pressure overcame the confining pressure. However, the gas movement module which used the MIP algorithm, within the combined ETM/MIP model, was called upon only once the gas saturation exceeded the critical gas saturation ( $S_{\rm gcr}$ ). This value, taken to be 0.3 (Mumford et al., 2010), represented the gas saturation that a block needed to reach in order for the gas in one block to be connected to the gas in an adjacent block. Any grid block with a gas saturation over  $S_{\rm gcr}$  could be included in a

multi-block cluster and able to mobilize, fragment, or expand. In addition, any newly occupied block was assigned a gas saturation equal to  $S_{\rm gcr}$ .

To calculate the gas saturation, each block in the domain was assigned an entry pressure  $(P_e)$ , a terminal pressure  $(P_t)$ , and a displacement pressure  $(P_d)$ . A variable distribution of displacement pressures was obtained using a cumulative distribution function based on the Young-Laplace equation. Entry pressures were calculated using equation (5.11), applying the obtained displacement pressures and setting the water saturation to  $(1 - S_{gcr})$ . The ratio between terminal pressure and entry pressure was taken to be 0.57 throughout the domain (Gerhard & Kueper, 2003; Mumford et al., 2009).

Thresholds for drainage  $(P_{te})$  and for imbibition  $(P_{tt})$  were:

$$P^{te} = P^e + P_w ag{4.23}$$

$$P^{tt} = P^t + P_w ag{4.24}$$

Gas saturations were obtained using equation 4.21. If any block resulted in a gas saturation exceeding  $S_{gcr}$ , the gas movement module was called upon. Any blocks with gas saturations at or above  $S_{gcr}$  were tagged. Using the MATLAB image processing toolbox, any connected tagged blocks were identified as part of the same cluster. In searching for connections, only blocks sharing faces were considered (coordination number of 4). Each cluster was examined individually and assessed for expansion or mobilization, following the rules outlined by Glass et al. (2001) and Li & Yortsos (1995). The three processes are shown in Figure 4.26, where the hatched squares represent gas-occupied blocks while white squares are fully water saturated grid blocks (adapted from Wagner et al. (1997).

In order for a gas cluster to expand into an adjoining block (Figure 4.26a), the average gas pressure in a cluster ( $P_{ave~1;2}$ ) had to be greater than the drainage threshold of the adjacent block( $P_{te~3}$ ) (subscripts refer to block numbers in the Figure). For mobilization (Figure 4.26b), the minimum drainage threshold of a block located next to a gas cluster ( $P_{te~4}$ ) had to be less than the threshold for imbibition for a block the gas cluster( $P_{tt~1}$ ). Fragmentation occurred when the mobilized block was located within a gas cluster as seen in Figure 4.26c. In this case the gas from block 2 moved to block 4 (via block 3), fragmenting the original cluster into two gas clusters. It is useful to characterize the potential for cluster mobilization in a given sand using a critical cluster length. Critical cluster lengths ( $h_{crit}$ ) can be estimated using the capillary pressures at the bottom ( $P_{bottom~c}$ ) and top ( $P_{top~c}$ ) of the gas cluster as well as the hydrostatic pressure drop across the height of the cluster, as given by Mumford et al., (2009).

$$h_{crit} = \frac{P_c^{top} - P_c^{bottom}}{\Delta \rho g}$$
 [4.25]

Values of  $h_{crit}$  can be calculated by taking  $P_{top c}$  to be the capillary pressure at a gas saturation of 0.3 (using equation 4.22) and  $P_{bottom c}$  to be half of  $P_{top c}$  (Mumford et al., 2009)

The Bond number (Bo) which relates buoyancy forces to capillary forces can also be used as an indication of discrete gas movement (Brooks et al., 1999; Mumford et al., 2009; Selker et al., 2007).

$$Bo = \frac{\Delta \rho g r^2}{\sigma} \tag{4.26}$$

 $\Delta \rho$  is the difference in density between the wetting and non-wetting fluids (water and air, receptively), r is the characteristic pore radius, and  $\sigma$  is the interfacial tension. Typically, large Bond numbers and short cluster lengths correspond to high permeability soils where gas clusters tend to mobilize more easily(Mumford et al., 2009). When a bubble mobilized, the pressure in the invading block (P4 from Figure 4.26b) was adjusted for the temperature based on conservation of mass between the invading block and the block from which the bubble is leaving (P1), using the Ideal Gas Law:

$$P_4 = \frac{P_1 S_{g1} T_4}{T_1 S_{gcr}}$$

[4.27]

Similarly, each time a gas cluster expanded or mobilized, the pressure within a gas cluster was modified. Since the temperature in a gas cluster was different at each block, the average temperature within a cluster was used and the pressure was adjusted in order to have the same average gas mass and pressure in each cluster block. At the end of the gas movement module, if a bubble expanded or moved, new aqueous concentrations were calculated keeping the aqueous mass constant. After the gas movement step, the water and gas concentrations and saturations for each grid block were calculated using the total mass (*M*) from the gas movement module and the equilibrium using equation 4.21. If the equilibrium calculations resulted in gas saturations of zero (due to spatial change in temperature) in nodes where bubble mobilization or expansion occurred, the bubble would collapse. Bubble collapse would result in the mass in the gas phase being transferred to the aqueous phase:

$$C_w = \frac{M}{\phi}$$

[4.28]

After each time step an energy and mass balance was performed on the system.

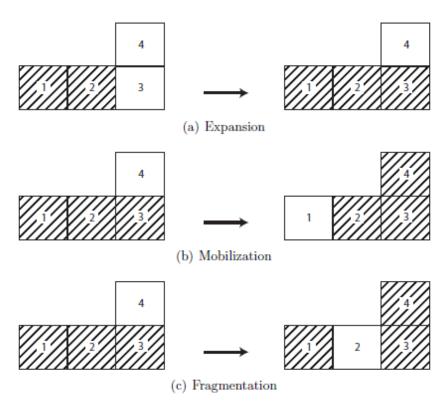


Figure 4. 26. Gas clusters before and after: a) expansion; b) mobilization; and c) fragmentation. Hatched squares represent gas-occupied grid blocks, while white squares are fully water-saturated blocks. Adapted from Wagner et al., (1997)

#### Simulations of bubble formation and movement

To examine the effect of heat on bubble formation and resulting mass distribution, several soil and temperature scenarios were simulated using the ETM-MIP model. The simulation consisted of a 34 cm by 34 cm cell that represented a vertical cross section of the subsurface. Six electrodes were used in the simulation of ERH, using one phase heating. A Darcy velocity of 5 x  $10^{-6}$  m/s was specified at the left boundary. Three soils with different permeabilities and displacement pressures were examined and the corresponding parameters are listed in Table 4.2. Table 4.2 also lists the calculated critical cluster lengths and Bond numbers based on eqs. (4.25) and (4.26) respectively.

At the beginning of the simulations, the subsurface was fully water saturated and no dissolved gases were present in the subsurface. A uniform subsurface temperature of 20°C was assumed. The heat and mass transport boundary conditions were zero flux for the top and bottom of the system, while a known water flow at 20°C was specified on the left side boundary. In

addition, the water pressure at the top of the domain was set to atmospheric pressure. All voltage boundary conditions were zero flux, assuming no current flow outside the boundaries of the simulated area. The linear equations for the discretized current, groundwater flow, heat, and mass transport were evaluated using the backslash (n) operation in MATLAB which uses appropriate algorithms depending on the structure of the matrix.

The organic compound chosen for this study was 1,1,1 TCA, with a relatively low boiling point and a solubility of 1,330 mg/L (at 20°C) (Pankow & Johnson, 1996). Table 4.3 lists the properties of the compound as well as the initial conditions of the simulated scenarios. An initial aqueous concentration of 1200 mg/L 1,1,1 TCA was specified in the center of the simulation area, presented on Figure 4.27. Each case was simulated at three target temperatures, 50, 70 and 90°C. To control the subsurface temperature, the power in the model was turned off when the maximum temperature anywhere in the domain reached the target temperature, and then turned on once the maximum temperature dropped below the target level.

The reference permeabilities, displacement pressures, pore size distribution indices and residual water saturations were obtained from (Kueper 1990) and were used to develop a variable pore radius matrix based on the Young-Laplace relationship. Relative permeability of the water phase was not reduced due to air saturation in these simulations (i.e., the focus here is on gasphase transport and it has been assumed that gas-phase movement is independent of advective water velocity.)

Table 4. 2. Bubble formation simulation scenarios. (Source - Kueper, 1990)

Ottawa sand	Reference	Mean	$P_{dref}$	λ	$S_{wr}$	Bond	$h_{crit}$
fraction	permeability	pore radius				$_{ m number}$	
(units)	$(cm^2)$	(mm)	(cm)	(-)	(-)	(-)	(cm)
#25	$2 \times 10^{-6}$	0.257	4.43	3.51	0.069	$8.7 \times 10^{-3}$	2.5
#50	$5.3 \times 10^{-7}$	0.077	13.5	2.49	0.098	$7.8 \times 10^{-4}$	7.9
#70	$8.2 \times 10^{-8}$	0.034	33.1	3.30	0.189	$1.5 \times 10^{-4}$	19

To calculate the locally variable displacement pressures ( $P_d$ ) in macroscopically homogeneous soils, the Young-Laplace equation and the variable pore radius matrix were used. Permeability distributions (k) were obtained using the Leverett relationship (equation 4.29), using the reference displacement pressures and permeabilities, where the porosity and surface tension were kept constant (Kueper & Frind, 1988; Kueper & McWhorter, 1992; Leverett, 1940).

$$k = \left(\frac{P_{dref}}{P_d}\right)^2 k_{ref}$$

[4.29]

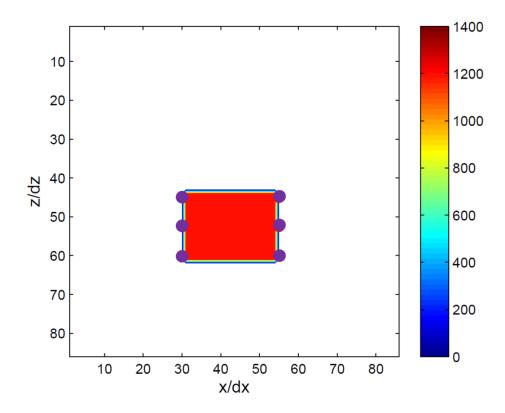


Figure 4. 27. Initial aqueous concentration (mg/L) in a vertical slice of the subsurface; purple circles represent electrodes locations

**Table 4. 3. System initial conditions and 1,1,1-TCA properties. Sources:** <sup>a</sup>Markle et al., 2006; <sup>b</sup>Pankow & Johnson, 1996; <sup>c</sup>Lide, 2006; <sup>d</sup>Mumford et al., 2010

$L_z, L_y$	Simulation depth and width (mm)	340, 340
dx, dy	Grid discretization $(mm)$	4, 4
dt	Time step $(s)$	10
n	Soil porosity (-)	0.35
$K_H$	Soil Thermal Conductivity $(W/mK)^a$	2
T	Initial Temperature ( ${}^{\circ}C$ )	20
q	Darcy Velocity $(m/s)$	$5 \times 10^{-6}$
$P_w^v$	Water Vapour Pressure $(Pa)^b$	$2.3 \times 10^{3}$
$\sigma$	Water Interfacial Tension $(N/m)$	0.072
S	1,1,1- TCA Solubility $(mg/L)^b$	1330
Bp	1,1,1- TCA Boiling Point (°C <sup>c</sup> )	74
H	Henry's Coefficient $(Pa.m^3/mol)^b$	$1.3 \times 10^{3}$
$C_{0}$	Initial Concentration $(mg/L)$	1200
$S_{gcr}$	Critical Gas Saturation $(-)^d$	0.3

Thirty minutes of heating was simulated for all three sands at all three temperatures, and gas saturations and aqueous concentrations were recorded throughout the simulations. Once the subsurface temperature increased to a level where the total gas pressure was greater than the confining pressure, gas bubbles started forming. When the gas saturation reached  $S_{\rm gcr}$ , the gas movement module was called and the contaminant mass was also transported by gas movement. The following section describes the results for the three soils for a single realization of the pore space.

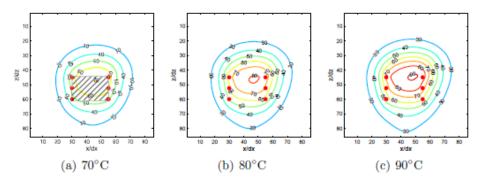


Figure 4. 28 Temperature distributions for #25 Ottawa sand after 30 minutes of heating. Temperature distributions for the #50 and #75 sands were similar.

The temperature distributions for all three temperatures for the #25 Ottawa sand are presented in Figure 4.28. Bubble formation started when temperatures reached 65°C in the area with the highest concentration and temperature and lowest confining pressure. The gas pressure was based on Henry's law (Gossett, 1987) using a concentration of 1200 mg/L 1,1,1 TCA. Figure 4.29 shows the calculated temperature at which this combined pressure was equal to atmospheric (upper boundary water pressure).

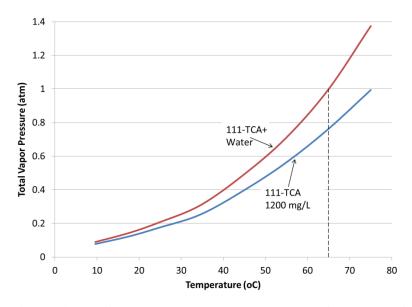


Figure 4. 29. Calculated total vapor pressures for 1,1,1-TCA with (red line) and without (blue line) the contribution of water.

Discrete bubble formation was followed by expansion and mobilization of the gas clusters within the heated section once gas saturation reached  $S_{\rm gcr}$ . The effect of temperature on gas bubble formation and movement in #25 Ottawa sand is presented in Figure 4.30a. Mass transfer of 1,1,1-TCA from the aqueous to the gas phase within the heated zone was observed at all temperatures, however gas phase mobilization only occurred at operating temperatures of 80 and 90°C. High temperatures resulted in higher gas pressures leading to greater bubble expansion. In addition, in these simulations, higher temperatures resulted in increased groundwater velocities through the heated zone leading to faster advective mass transport. However, as discussed above, loss of water permeability due to the bubbles was not included in the model.

Gas saturations for the #50 Ottawa sand are presented in Figure 4.30b. Bubble mobilization in #50 Ottawa sand occurred less frequently than in the more permeable soil (#25 Ottawa sand) and the extent of bubble movement was limited. The same trend was observed in experiments conducted by Mumford et al. (2009a) and Mumford et al. (2009b). Since #50 Ottawa sand had longer critical cluster lengths than #25 Ottawa sand, more bubble growth (expansion) needed to occur before bubble mobilization could take place. At 90°C, increased cluster gas pressure led to increased gas expansion, resulting in bubble mobilization. However, bubble mobilization occurred less often than in the more permeable soil

Gas saturation (Figure 4.30c) for #75 Ottawa sand, were similar to those of #50 Ottawa sand, especially at lower temperatures. At higher temperatures, rapid aqueous mass transport out of the heated zone occurred in #75 Ottawa sand through gas expansion where the gas bubbles either collapsed or got trapped by higher entry pressures. Since #75 Ottawa sand has very high critical cluster lengths, bubble activity was almost exclusively limited to bubble expansion (very little bubble mobilization occurred). This transfer of aqueous mass to the gas phase was especially pronounced at 90°C, where the heated zone was mostly gas filled (Figure 4.30c).

An important conclusion from the modeling is that, regardless of temperature or soil type, for aqueous contaminants, mobilization occurred for only a short period of time when the combination of subsurface temperature and high dissolved concentration was present in the heated zone. At the beginning of the simulation, temperatures were too low to induce bubble growth, whereas at the end of the simulation, significant amount of mass had moved out of the aqueous phase to substantially reduce the vapor pressure contribution of the contaminant. These effects may have both benefits and advantages for in situ remediation using low-temperature ERH, depending on how they are managed. Unfortunately, this modeling is not currently predictive, and as a result the overall effects are difficult to assess at this point.

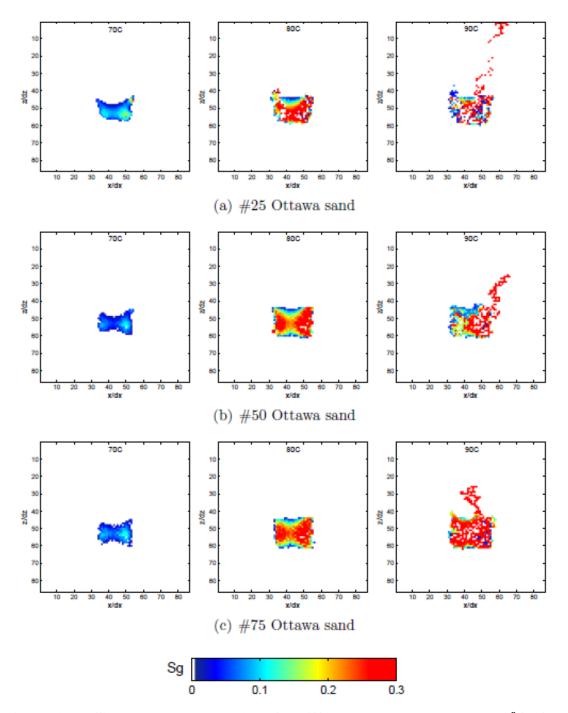


Figure 4. 30. Simulated gas saturations for different sands at 70, 80 and  $90^{\circ}\text{C}$  after 9 minutes of heating.

#### 4.4. HETEROGENEOUS AZEOTROPIC BOILING

## 4.4.1. 1-D Experiments

Figure 4.31 shows the temperature and mass removal data for the emplaced CT source experiment. In addition, the figure shows a sequence of photographs that are matched to the X axis on the graph. The photographs allow several qualitative observations about the experiments to be made. First, as the temperature approached the azeotrope value there was some upward displacement of the CT. This appeared to be due to the production of a small volume of vapor within the CT. This was likely to have been the case because of dissolved gases in the water used for the experiment. Once the temperature was above the azeotrope value (ca. 6000 seconds) there was a relatively steady removal of CT from the experiment.

Even at the azeotrope temperature, the time required for removal of the CT was fairly long (e.g., ~4000 seconds). This suggests that the volatilization process may have been controlled by a physical process within the system. Given that the water/DNAPL interface was intentionally kept to a minimum by emplacing the DNAPL to minimize water contact, it seems likely that the rate of dissolution at the water/CT interface could have been important.) This would not be surprising, since saturation conditions (CT in water or water in CT) need to exist before azeotropic boiling can occur, and in this experiment those conditions only existed at the water/CT interface.

For the well-mixed CT experiment there was an initial rapid removal of mass which was likely due to saturated CT concentrations in much of the water as the result of the mixing process (Figure 4.32). (A similar but smaller situation can be observed in the emplaced CT experiment, Figure 4.31). The rate at which CT was removed from the well-mixed experiment appears to be 2-3 times faster than for the emplaced source case, and this supports the idea that the mass removal rate is likely influenced by the extent of the CT/water interface.

In the 1-D experiments the mass recovery was slightly above 100 percent. This was due to incorporation of some water into the distilled materials (the typical azeotrope concentrations of CT and water are 95 and 5 percent by weight, respectively)

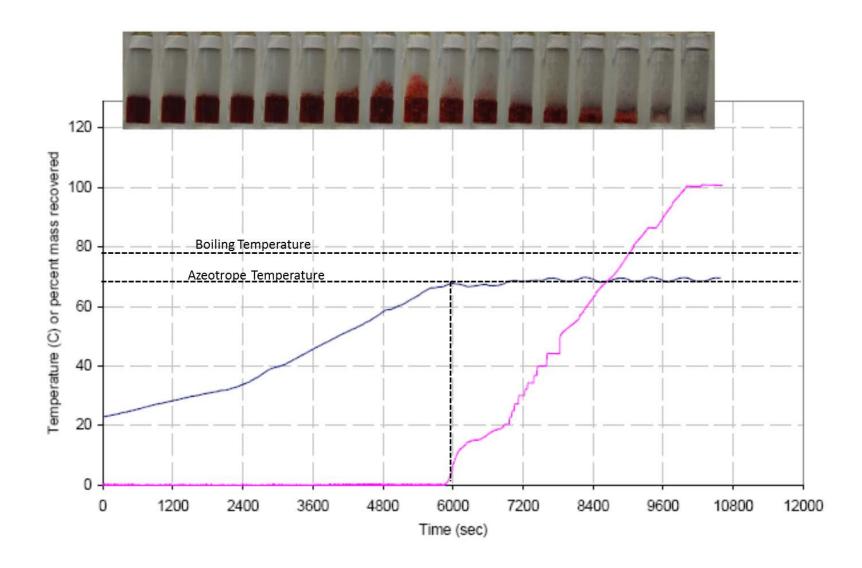


Figure 4. 31. 1-D heterogeneous azeotropic boiling experiment with an emplaced source. The blue line represents the temperature and the pink line is the percent mass recovered.

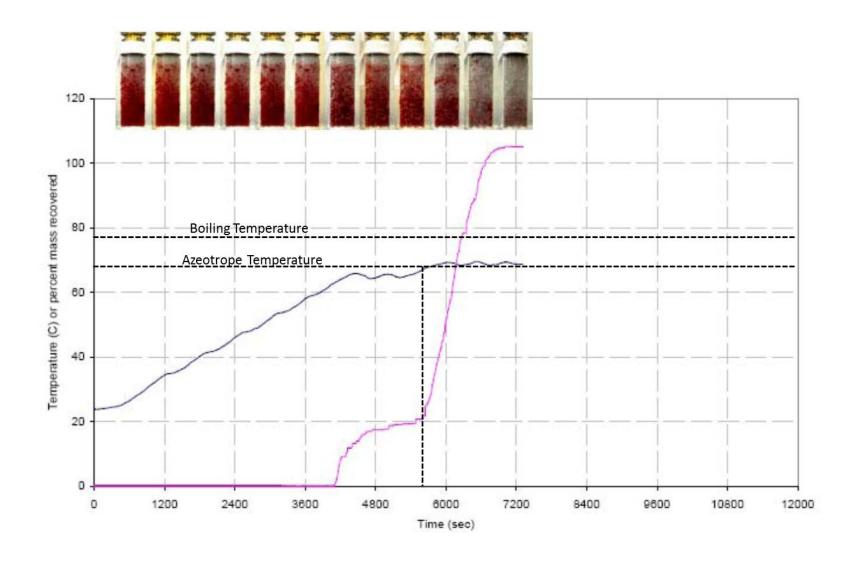


Figure 4. 32. 1-D heterogeneous azeotropic boiling experiment with well-mixed source.

The blue line represents the temperature and the pink line is the percent mass recovered.

#### 4.4.2. 2-D Experimental Results

Figure 4.33 shows mass removal, temperature and volume change data for the 2-D experiment, as well as photographs taken at several stages of the experiment. Some lateral spreading of the CT liquid was observed as the temperature was increased. This is not surprising, given the changes in viscosity and interfacial tension that would be expected with increasing temperature.

Unlike the 1-D experiments, mass removal did not occur for some time after the azeotrope temperature was reached. As discussed in the previous section, this was likely due to dissolution of the CT vapor back into the water above the spill. This would initially limit the vertical extent to which the vapor would move. As the concentration in the water adjacent to the vapor pathways increases, the rate at which the CT partitioned out of the vapor in into the water will decrease, and the vertical extent of the vapor pathways will increase. Eventually, depending on temperatures and groundwater flow, these pathways could reach the water table. However, in the context of targeted heating of DNAPL source zones, it is likely that vertical movement of the vapors could be readily controlled by managing the temperature.

As expected, the fluid volume (water +DNAPL) increased with increasing temperature. The volume of liquid in the experiment was ~1250 mL, and the approximate volume change due to water expansion is shown in Figure 4.33. Additionally, as discussed in the previous section, as the temperature increases the solubility of dissolved atmospheric gases decreases and they contribute significantly to the total vapor pressure at lower temperatures. At the azeotrope temperature for CT, it can be calculated that the dissolved atmospheric gases will contribute about 11 mL of gas in the experiment. This represents most of the difference between the increased volume due to water expansion and the observed change in volume within the experiment.

Initial breakthrough of CT at the water table occurred once continuous vapor channels to the surface were established. This occurs when the VOC concentration remains high enough in the gas to exceed the total vapor pressure. In the context of this experiment, where the temperature was uniform and there was not groundwater flow, this occurred fairly rapidly. The volume of fluids in the experiment reached a maximum just prior to vapor breakthrough at just before 10,000 seconds into the experiment. The volume increase was followed by a decrease in volume the corresponded to "venting" of a significant portion of the trapped vapor in the experiment. There was a noticeable increase in "noise" in the volume data beginning about 11000 seconds. This was due to the steady production of vapor and the movement of the vapor as bubbles up the vertical tube to which the pressure transducer was connected (see Figure 3.11).

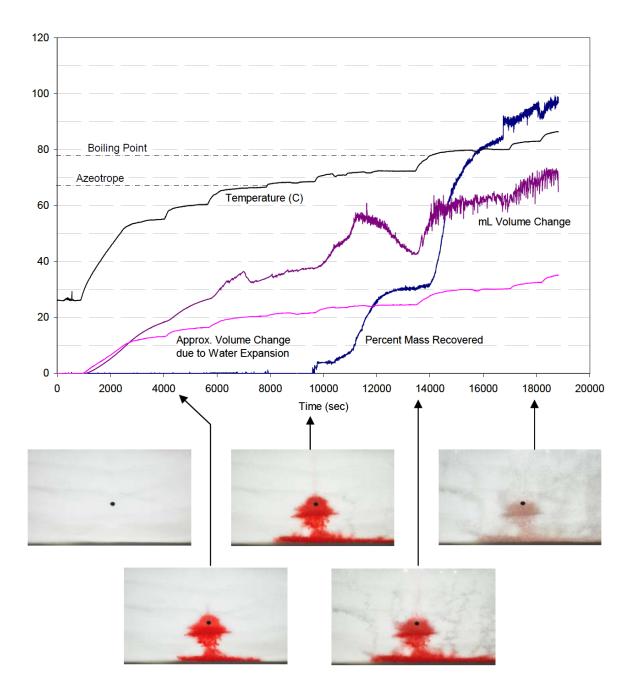


Figure 4. 33. 2-D Heterogeneous azeotropic boiling experiment with a DNAPL source.

#### 4.5. THERMAL EFFECTS ON IN SITU CHEMICAL OXIDATION

As discussed above, the combination of LTERH and in situ chemical reactions is attractive as a remediation strategy for a number of reasons. First, temperature-dependent reaction rates are typically very predictable and controllable. Second, if heating can be targeted, then so can the chemical reaction process. The experimental results described below utilize persulfate ion in batch experiments to assess both the rate at which contaminants can be degraded and the time frame over which the persulfate is likely to persist in the subsurface. The latter is important because it will control the time period over which treatment can be effective, as well as the distance over which the reactant can move by diffusion.

# 4.5.1. PCE Dechlorination Kinetics with Persulfate. <sup>2</sup>

As shown in Figure 4.34 for PCE, oxidation of the chlorinated ethenes with thermally activated  $Na_2S_2O_8$  was pseudo-first-order for 1-2 half-lives at every temperature studied. In some cases, data were collected for more than 2 half-lives, and the later time-points exhibited the distinctive downward curvature shown in Figure 4.35. The fact that this curvature can also be seen in previously published data for TCE and 1,1,1-trichloroethane oxidation by persulfate (Liang et al., 2003) suggests that the effect is not peculiar to the conditions of this study. The cause of this curvature was not explored in this or the previous study, but it could be due to the combined reactivity of sulfate radical and other reactive species that form as the reaction progresses. To avoid having to model this phenomenon, we fit only the initial linear portion of the data (1-2 half-lives) using the pseudo first- order model. From a practical perspective, the increasing slopes of the lines in Figure 4.35 indicate that the rate of degradation is increasing with time in these experiments. As a consequence, fitting the linear portions of the curves represents a conservative estimate of persulfate reaction rates.

-

<sup>&</sup>lt;sup>2</sup> Much of the information in this section came directly from our publication Waldemer et al. (2007)

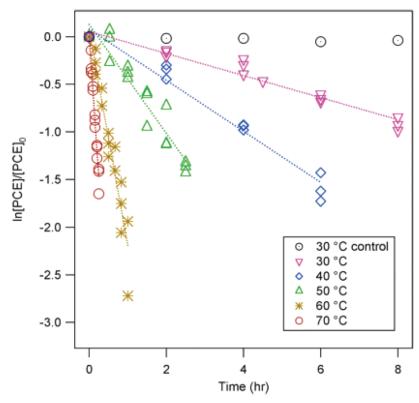


Figure 4. 34. Pseudo-first-order disappearance of PCE at five temperatures. Experimental conditions: unbuffered, 4.5 x  $10^{-5}$  M PCE, and 4.5 x  $10^{-4}$  M Na<sub>2</sub>S<sub>2</sub>O<sub>8</sub>. Regression on pooled data for triplicate experiments at each temperature. The control was done without persulfate.

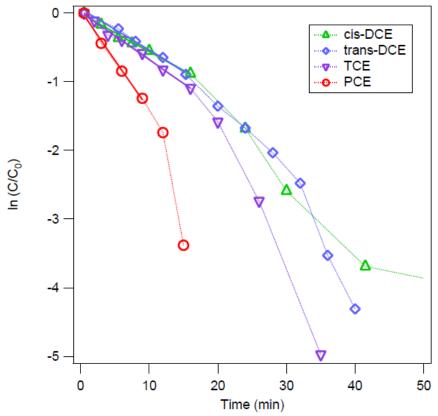


Figure 4. 35. Concentration over extended time periods, showing non-pseudo first-order behavior at longer experimental times. Experimental conditions: Unbuffered DI water,  $70^{\circ}$ C, 10:1 molar ratio of  $Na_2S_2O_8$  and chlorinated ethenes, concentration of PCE = 0.0014 M, concentration of the other chlorinated ethenes = 0.002 M.

The resulting values of  $k_{\rm obs}$  are given in Table 4.4 for the four chlorinated ethenes and five temperatures studied. For all four chlorinated ethenes,  $\ln(k_{\rm obs})$  decreased linearly with 1/T (Figure 4.36) and, therefore, were fit to an Arrhenius type model where A is the pre-exponential factor,  $E_A$  is the apparent activation energy, R is the universal gas constant, and T is the absolute temperature.

$$\ln k_{\text{obs}} = \ln A - E_A / RT \tag{4.30}$$

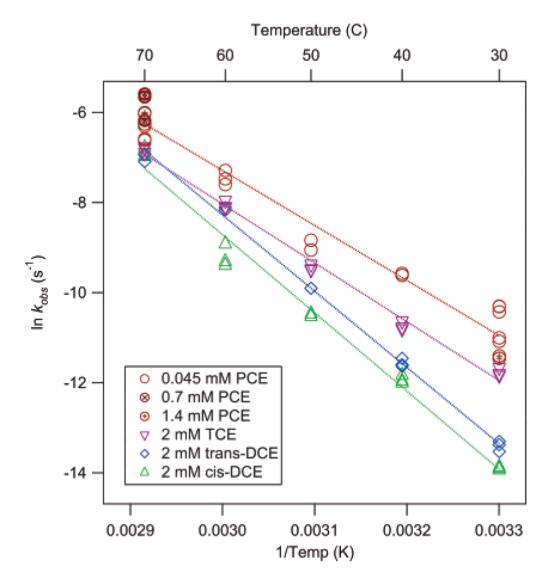


Figure 4. 36. Arrhenius plots for the chlorinated ethenes. Experimental conditions: unbuffered, 10:1 molar ratio of  $Na_2S_2O_8$  to chlorinated ethenes. Initial concentrations are given in the legend.

Compound	30°C		40 °C		50°C		60°C		70 <b>°</b> C		In A (s <sup>-1</sup> )	E <sub>A</sub> (kJmol <sup>-1</sup> )
•	0.023 hr <sup>-1</sup> 0.027 hr <sup>-1</sup>	0.95 0.97	0.24 hr <sup>-1</sup> 0.25 hr <sup>-1</sup>	0.99	0.0087 min <sup>-1</sup>	0.94	0.041 min <sup>-1</sup>	0.98	0.11 min <sup>-1</sup> 0.080 min <sup>-1</sup>	0.97	-	
0.045 mM PCE	0.031 hr <sup>-1</sup>	0.97	0.24 hr <sup>-1</sup>	0.96	0.0070 min <sup>-1</sup>	0.97	0.034 min <sup>-1</sup>	0.94	0.083 min <sup>-1</sup>	0.97		
	0.060 hr <sup>-1</sup> 0.055 hr <sup>-1</sup>	0.99_									29 ± 2	101 ± 4
0.0014 M PCE	0.038 hr <sup>-1</sup> 0.040 hr <sup>-1</sup>	0.99		 <b></b>		 <b></b> _			0.148 min <sup>-1</sup> 0.145 min <sup>-1</sup> 0.115 min <sup>-1</sup>	0.99 0.98 0.98	- -	
0.002 M TCE	0.027 hr <sup>-1</sup> 0.031 hr <sup>-1</sup> 0.026 hr <sup>-1</sup>	0.98 0.97 0.99	0.073 hr <sup>-1</sup> 0.087 hr <sup>-1</sup> 0.076 hr <sup>-1</sup>	0.94 0.97 0.93	0.0046 min <sup>-1</sup> 0.0045 min <sup>-1</sup> 0.0051 min <sup>-1</sup>	0.96 0.97 0.96	0.0211 min <sup>-1</sup> 0.0184 min <sup>-1</sup> 0.0179 min <sup>-1</sup>	0.99 0.99 0.99	0.061 min <sup>-1</sup> 0.067 min <sup>-1</sup> 0.069 min <sup>-1</sup>	0.99 0.99 0.9	31 ± 1	108 ± 3
0.002 M cis-DCE	0.0033 hr <sup>-1</sup> 0.0034 hr <sup>-1</sup> 0.0032 hr <sup>-1</sup>	0.93 0.96 0.95	0.023 hr <sup>-1</sup> 0.022 hr <sup>-1</sup> 0.026 hr <sup>-1</sup>	0.9 <u>6</u> 0.99 0.99	0.0017 min <sup>-1</sup> 0.0016 min <sup>-1</sup>	0.94 0.98	0.008 min <sup>-1</sup> 0.0054 min <sup>-1</sup> 0.005 min <sup>-1</sup>	0 <u>.91</u> 0 <u>.99</u> 0.80	0.056 min <sup>-1</sup> 0.068 min <sup>-1</sup> 0.057 min <sup>-1</sup>	0.99 0.98 0.99	43 ± 2	144 ± 5
0.002 M trans-DCE	0.0048 hr <sup>-1</sup> 0.0060 hr <sup>-1</sup> 0.0056 hr <sup>-1</sup>	0.97 0.96 0.97	0.033 hr <sup>-1</sup> 0.038 hr <sup>-1</sup> 0.032 hr <sup>-1</sup>	0.99 0.99 0.97	0.0030 min <sup>-1</sup> 0.0030 min <sup>-1</sup>	0.98 0.99	0.018 min <sup>-1</sup>	0.98 0.98 0.97	0.050 min <sup>-1</sup> 0.058 min <sup>-1</sup> 0.059 min <sup>-1</sup>	0.99 0.99 0.98	43 ± 1	141 ± 2

The  $R^2$  values given after each rate constant are for linear regression on the  $\ln$  concentration vs. time data for each experiment.

Table 4. 4.  $k_{obs}$  and corresponding activation parameters for all 4 chlorinated ethenes.

The fitting parameters from these calculations are presented in Table 4.5. Both  $\ln A$  and  $E_A$  follow the pattern PCE < TCE < trans-DCE < cis-DCE; in fact,  $\ln A$  and  $E_A$  correlate well with  $R^2$  of 0.999 (Figure 3), a phenomenon that is commonly observed but of uncertain significance.

Table 4. 5. Arrhenius parameters for chlorinated ethenes.

TABLE 1. Arrhenius Parameters for Chlorinated Ethenes							
compound	In $A$ (s $^{-1}$ ) $^a$	$E_{\rm A}$ (kJ mol $^{-1}$ ) $^a$	n	<b>R</b> <sup>2</sup>			
PCE TCE <i>cis</i> -DCE	$\begin{array}{c} 29 \pm 2 \\ 31 \pm 1 \\ 44 \pm 2 \end{array}$	$\begin{array}{c} 101 \pm 4 \\ 108 \pm 3 \\ 144 \pm 5 \end{array}$	25 15 14	0.96 0.99 0.98			
<i>trans</i> -DCE	$43\pm1$	$141\pm2$	14	0.99			

<sup>&</sup>lt;sup>a</sup> Uncertainties are one standard deviation derived from fitting eq 10 to the data in Figure 2.

A consequence of this is that  $k_{\rm obs}$  also follows the pattern PCE > TCE > trans-DCE > cis-DCE and correlates with  $\ln A$  and  $E_A$  (shown in Figure 4.37, for 30°C). Additionally,  $\ln A$ ,  $E_A$ , and  $k_{\rm obs}$  all correlate fairly well with the energy of the highest occupied molecular orbital ( $E_{\rm HOMO}$ ) for the chlorinated ethenes. This is to be expected because oxidations, regardless of the exact mechanisms, generally involve a shift of electron density from the HOMO of the reductant (in this case, the chlorinated ethenes) to an electron acceptor (in this case, sulfate radical) (Canonica & Tratnyek, 2003). These correlations suggest that the rate-determining step for chlorinated ethene oxidation by heat activated persulfate involves reaction with sulfate radical and is not, for example, the formation of the radical.

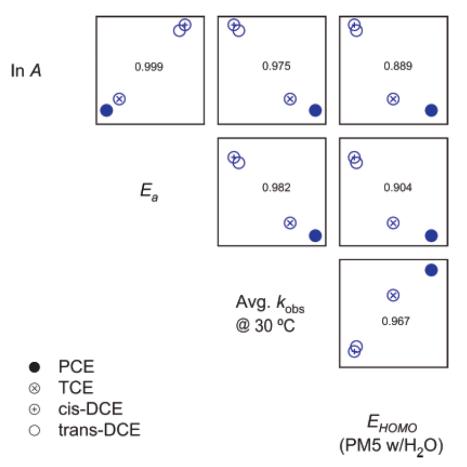


Figure 4. 37. Correlation between lnA,  $E_A$ ,  $k_{obs}$ , and EHOMO for oxidation of the chlorinated ethenes by heat-activated persulfate.  $R^2$  are given in each panel.  $E_{HOMO}$  were calculated as described previously (Waldemer & Tratnyek, 2006).

Our value of  $E_A$  for TCE is within 10% of the value reported previously (97.7 kJ mol<sup>-1</sup>) by (Liang et al., 2003). The only other data on  $E_A$  for oxidation of chlorinated ethenes by heat activated persulfate are from Huang et al. (2005). These values (PCE: 46.4, TCE: 60.7, *cis*-DCE: 41.4, *trans*-DCE: 49.8, 1,1-dichloroethene: 64.9, and vinyl chloride: 56.9 kJ mol<sup>-1</sup>) are significantly lower (2-3 fold) than the values reported here (and by Liang et al., 2003), and the two sets of data do not correlate well. A likely explanation for this disagreement lies in the fact that Huang et al. measured degradation kinetics in a mixture of 59 contaminants. In such a situation, all of the contaminants - and possibly their degradation intermediates and products can compete for sulfate radical and any other reactive species. This competition effect could explain why the apparent activation energies for the chlorinated ethenes are lower in pseudo-first-order reactions with many other species present than when they are the only reductant in solution.

**Effect of Bicarbonate.** Sulfate radical oxidizes bicarbonate ( $HCO_3$ ) to carbonate radical according to equation [4.31]. Both this reaction and the equivalent reaction for carbonate proceed rapidly, and since the pKa of carbonate radical is less than zero (Czapski et al., 1999), it will be produced whether the reaction is initiated with carbonate or bicarbonate.

$$SO_4^{\bullet -} + HCO_3^{-} \rightarrow SO_4^{2-} + CO_3^{\bullet -} + H^+$$
[4.31]

These reactions are of concern because (bi)carbonate concentrations that are typical of groundwater (50-400 mg/L or 0.82-6.6M (Matthess, 1982)) could result in suppressed concentrations of sulfate radical, and therefore slower degradation of chlorinated ethenes, during ISCO with activated persulfate. This problem is analogous to the effect of (bi)carbonate on hydroxyl radical when Fenton-like reactions are used for ISCO (ITRC, 2005). To determine the degree that environmental concentrations of carbonate species affect the kinetics of oxidation by heat-activated persulfate, PCE was used as the model compound, along with 100, 300, and 500 mg/L of bicarbonate at 30, 50, and 70°C. The data were fit to pseudo-first-order kinetics as shown in Figure 4.38 for 30°C and the resulting values of  $k_{\rm obs}$  are given in Table 4.5. At all temperatures, bicarbonate inhibited the oxidation of PCE by activated persulfate (Figure 4.39). The inhibitory effect of bicarbonate appears to be steeper than a simple exponential relationship and equivalent at all three temperatures, but we did not attempt to model this behavior. The inhibitory effect of bicarbonate probably reflects competition between the PCE and bicarbonate for sulfate radical but changes in pH could also be contributing.

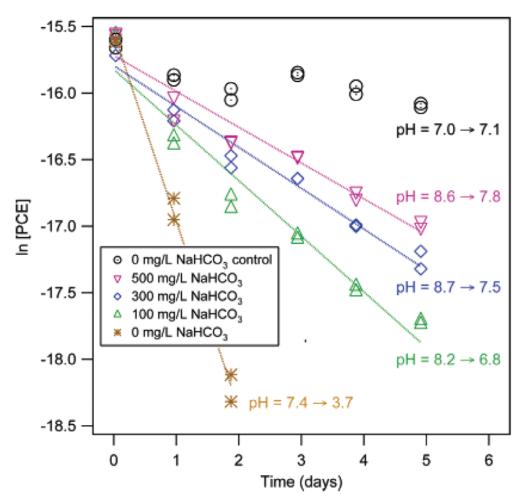


Figure 4. 38. Effect of bicarbonate on the oxidation of PCE by persulfate. Experimental conditions:  $30^{\circ}$ C,  $4.5 \times 10^{-5}$  M PCE,  $4.5 \times 10^{-4}$  M Na<sub>2</sub>S<sub>2</sub>O<sub>8</sub>. Replicate analyses are shown for each sample. The control did not contain persulfate or bicarbonate.

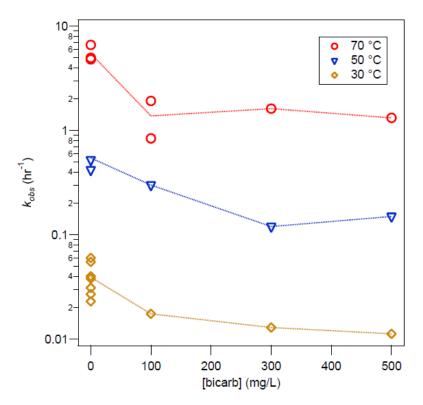


Figure 4. 39. Effect of bicarbonate concentration on kobs for PCE oxidation by persulfate activated at three temperatures. Conditions:  $4.5 \times 10^{-5}$  M PCE,  $4.5 \times 10^{-4}$  M Na<sub>2</sub>S<sub>2</sub>O<sub>8</sub>.

For all the experiments shown in Figure 4.39, the final pH decreased, possibly due to the release of protons when sulfate radical reacts with water and the degree of pH decrease was less pronounced with increased bicarbonate concentration (Figure 4.38). However, even with bicarbonate present, the oxidation of PCE still follows the Arrhenius model Figure 4.40, and the marginal changes in the Arrhenius parameters are consistent with simple competition between PCE and bicarbonate for sulfate radical (Table 4.6).

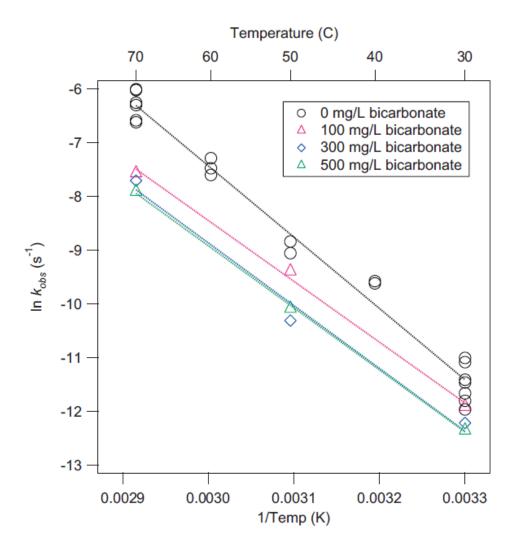


Figure 4. 40. Arrhenius plots of the oxidation of PCE by persulfate in the presence of various concentrations of bicarbonate. Experimental conditions:  $4.5 \times 10^{-5}$  M PCE,  $4.5 \times 10^{-4}$  M Na<sub>2</sub>S<sub>2</sub>O<sub>8</sub>. The data for 0 mg/L bicarbonate are the same as the data in Figure 4.36 in the text. Values for the data shown here are in Table 4.6.

Table 4. 6.  $k_{\rm obs}$  and corresponding activation parameters for PCE with different concentrations of bicarbonate.

Bicarbonate (mg L <sup>-1</sup> )	30°C	50°C	70°C	ln A (s · l)	E <sub>A</sub> (kJ mol <sup>-1</sup> )
	See Table S1	See Table S1	See Table S1	29 ± 2	101 ± 4
100	0.018	0.30	0.84	25 ± 2	94 ± 5
300	0.013	0.12	1.62	$26 \pm 5$	97 ± 12
500	0.011	0.15	1.32	$26 \pm 1$	96 ± 2

Little has been reported on the products of oxidation of the chlorinated ethenes by persulfate, and there is no information on how the reaction pathways and products are affected by temperature. Anticipating some degree of mineralization, we measured Cl<sup>-</sup> present at the end of experiments performed with the four chlorinated ethenes at 70°C. For this purpose, we chose to run each experiment for a period anticipated to encompass 4 half-lives of contaminant degradation (~94%), which was estimated from the average of the pseudo-first-order rate constants listed in Table 4.4. Overall, Cl<sup>-</sup> recoveries were consistent with complete dechlorination of 80-90% of each chlorinated ethene (data not shown). The only comparable literature data are for TCE, and they include Cl<sup>-</sup> recoveries of 75% at 40°C, 80% at 50°C, and 85% at 60°C (Liang et al., 2003). For systems containing sulfate radical, however, the interpretation of chloride data is complicated by the possibility that chlorine radicals are formed. The kinetic data necessary to evaluate how favorable chlorination of ethenes might be are available, but we did detect trace quantities of hexachloroethane as intermediates in the oxidation of TCE and PCE.

The only chlorinated compounds that were identified as major intermediates were *cis*-DCE during *trans*-DCE oxidation and *trans*-DCE during *cis*-DCE oxidation. This isomerization presumably occurs after formation of a single-bonded intermediate, which might be the radical cation formed by electron-transfer to sulfate radical (Minisci, Citterio, & Giordano, 1983), or the sulfate radical radical adduct, formed by asymmetric addition of sulfate radical to the double bond. Evidence for the latter is strong, with many sulfate radical adducts with alkenes having been identified by electron spin resonance (Chawla & Fessenden, 1975)(Davies & Gilbert, 1984; Koltzenburg, Behrens, & Schulte-Frohlinde, 1982). It is less clear, however, what factors control the elimination of sulfate radical to form the isomerized DCE's.

To evaluate the potential benefits of coupling ISCO and LTERH for chlorinated ethenes, it is necessary to consider how temperature affects a variety of contaminant degradation processes. For hydrolysis and oxidation by permanganate, it is straightforward to calculate the respective values of  $k_{\rm obs}$  vs temperature using previously published Arrhenius parameters (Huang et al., 2001; Jeffers et al. 1989), and appropriate assumptions regarding the dose of permanganate (100-40 000 mg/L, 0.0007 to 0.28M, Siegrist et al., 2001) and groundwater pH. For PCE, we show the results of these calculations in Figure 4.41, with the thickness of the bands reflecting the relevant ranges of permanganate concentration and pH.

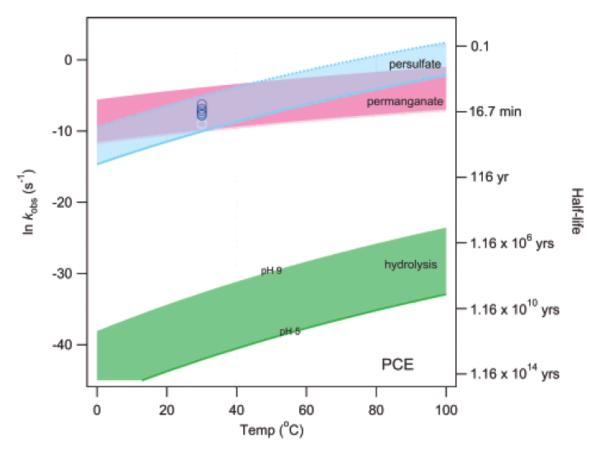


**Figure 4. 41.** Comparison of three degradation processes for PCE as a function of temperature. The hydrolysis band was calculated using Arrhenius parameters obtained from Jeffers et al. (1989). The bottom of the permanganate (pink) band corresponds to 100 mg/L (0.63 mM) permanganate and the top of this band corresponds to 40 000 mg/L (253 mM), calculated using Arrhenius parameters obtained from Huang et al. (2001). The persulfate band (light blue) corresponds to Arrhenius parameters obtained from experiments with 0.45 mM Na<sub>2</sub>S<sub>2</sub>O<sub>8</sub>/0.045 mM PCE. The data points correspond to experimental data for varying concentrations of  $S_2O_8^{2^2}$  while keeping the PCE concentration at 0.045 mM. The three concentrations represented by the data points are 4.5 mM, 45 mM, and 450 mM Na<sub>2</sub>S<sub>2</sub>O<sub>8</sub>. The dashed line (blue) shows the rate of reaction with PCE at the upper limit of this  $S_2O_8^{2^2}$  concentration range data extrapolated to higher temperatures assuming Arrhenius behavior.

For the other chlorinated ethenes, we used only a representative permanganate concentration and pH, and the results are shown in Figure 4.42.

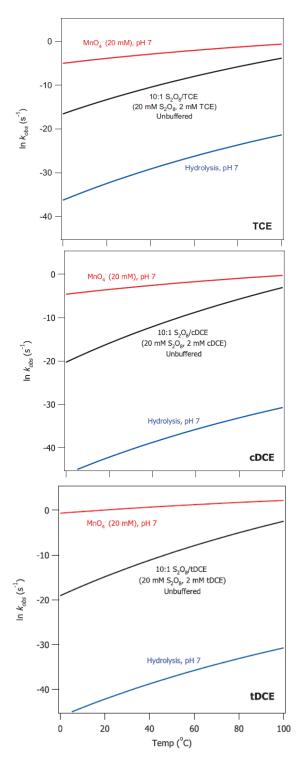


Figure 4. 42. Comparison of three degradation processes as a function of temperature for TCE, *cis*-DCE and *trans*-DCE.

Over the whole range of conditions considered, oxidation of the chlorinated ethenes is much faster than hydrolysis, although the opposite would have been the case for some of the more highly chlorinated ethanes. Additional factors must be considered for temperatures over

 $100^{\circ}$ C (Costanza et al., 2005). For contaminant oxidation by activated persulfate, it is more difficult to develop a general description of  $k_{\rm obs}$  vs. T because there are many reactions that can contribute to the concentration of sulfate radical, each with its own dependence on temperature. To overcome this, we used the  $E_A$  for PCE that was determined in this study (Table 4.5) to fix the slope of the temperature dependence and estimated the intercept ( $\ln A$ ) from replicate experiments done at initial concentrations of persulfate ranging from 107 to 107,000 mg/L (0.00045-0.45 M). This amounts to assuming that the apparent  $E_A$  is unaffected by persulfate concentration. The result, shown in Figure 4.41, reveals that the temperature at which the rate of PCE oxidation by heat-activated persulfate becomes greater than oxidation by permanganate is approximately  $40^{\circ}$ C; and, by  $100^{\circ}$ C, heat-activated persulfate oxidizes PCE about 400 times faster than permanganate.

In contrast, the other chlorinated ethenes (Figure 4.42) are much more reactive with permanganate than with activated persulfate. The relative reactivity of PCE with these two oxidants is consistent with the relative reactivity of the chlorinated ethenes with each oxidant: PCE > TCE > cis-DCE > trans- DCE with activated persulfate (Figure 4.36) and the reverse with permanganate (Waldemer & Tratnyek, 2006).

While the comparisons facilitated by Figures 4.41 and 4.42 should be qualitatively accurate, the absolute rates we calculated may differ from those observed in the field for a variety of reasons. Prominent among the factors that suggest slower degradation rates under in situ conditions is the inefficiency of mixing of aqueous-phase oxidants with aqueous- and nonaqueous-phase contaminants because of aquifer heterogeneity (Seol et al., 2003), limited dispersion (especially vertical mixing (Johnson & Pankow, 1992)), and displacement of nonsorbing contaminants by the injected fluids. Mixing inefficiencies might be ameliorated by coupling ISCO with LTERH, because LTERH should encourage mixing of the oxidant plume with the contamination (by increasing flow within the heated zone due both to reduced water viscosity and increased buoyancy of the heated water). Another reason to expect slower oxidation rates in the field is that "natural oxidant demand" will suppress sulfate radical concentrations (Brown et al., 2004). Here, again, coupling ISCO with LTERH may be advantageous, because persulfate will be relatively stable in unheated zones, and heat-activation can be focused on contaminated zones. Additional factors remain to be investigated, such as thermal effects on geochemical processes that might, in turn, influence contaminant oxidation rates.

# 4.5.2. Persistence of Persulfate under Thermal Activation Conditions<sup>3</sup>

# 4.5.2.1. Kinetics and stoichiometry of persulfate degradation.

The disappearance of persulfate in un-buffered deionized water is shown in Figure 4.43 for 70°C and four initial persulfate concentrations (0.1, 1.0, 10, and 100 mM).

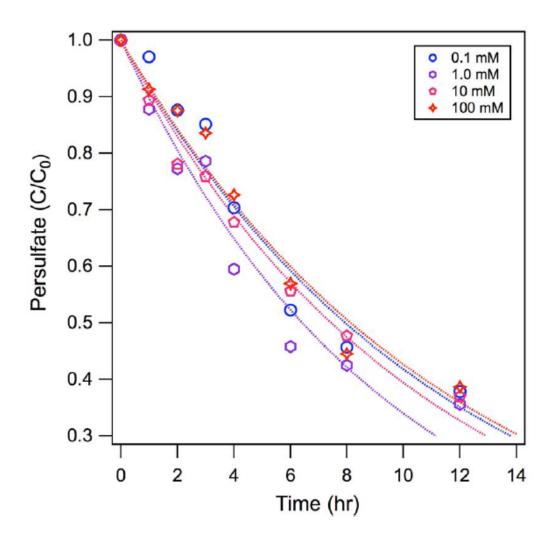


Figure 4. 43. Kinetics of persulfate disappearance in unbuffered, deionized water at 70°C. Initial persulfate concentrations are given in the legend. The curves are from fitting the data to first-order disappearance kinetics.

Fitting each time series for pseudo-first-order kinetics gives  $k_0$  ( $\pm 1$  standard deviation from the regression) equal to  $0.087 \pm 0.006$ ,  $0.108 \pm 0.008$ ,  $0.093 \pm 0.003$ , and  $0.085 \pm 0.005$  h<sup>-1</sup>, respectively. The agreement between these values—and lack of a trend among them—confirms that the disappearance of persulfate due to thermolysis under neutral conditions is pseudo first order. The values of  $k_0$  obtained from these experiments agree well with previously published

<sup>&</sup>lt;sup>3</sup> Most of the material in this section comes directly from our publication (Johnson et al., 2008)

results for similar conditions: e.g., 0.084/h (Kolthoff & Miller, 1951) and others discussed below. In some experiments, both sulfate appearance and persulfate disappearance were measured, and an example of these data is given in Figure 4.44.

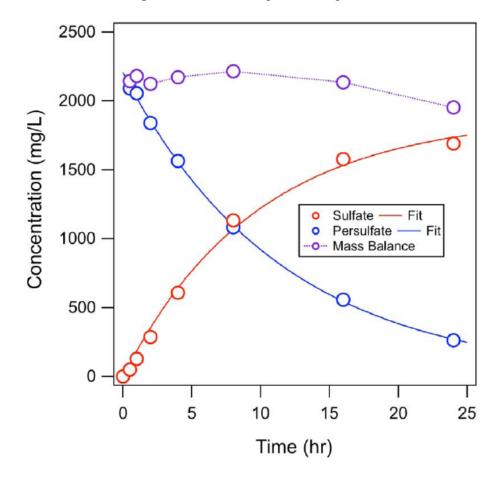


Figure 4. 44. Comparison of persulfate disappearance and sulfate appearance in unbuffered, deionized water at  $70^{\circ}$ C. Initial persulfate concentration = 2100 mg/L (10 mM).

Persulfate plus sulfate gave good mass balance, and  $k_0$  for disappearance of persulfate  $(0.087 \pm 0.002/h)$  is close to the  $k_0$  obtained for pseudo-first-order appearance of sulfate  $(0.104 \pm 0.011/h)$ . The average stoichiometric ratio for the data in the figure is 2.08. This is consistent with the expected 2:1 stoichiometry for uncatalyzed thermal homolysis of persulfate, but the overall 2:1 stoichiometry between sulfate and persulfate should hold even under conditions where the activation step is different (e.g., for low pH), because almost all pathways of persulfate decomposition eventually yield two sulfates. This characteristic—plus the greater sensitivity, linearity, and convenience of the sulfate analytical method, relative to that of the persulfate method—led us to use sulfate appearance as a surrogate for persulfate disappearance in some of the experiments described below. The appearance of sulfate was used to test for effects of pH and bicarbonate concentration on breakdown of persulfate at  $70^{\circ}$ C, and the results are shown in

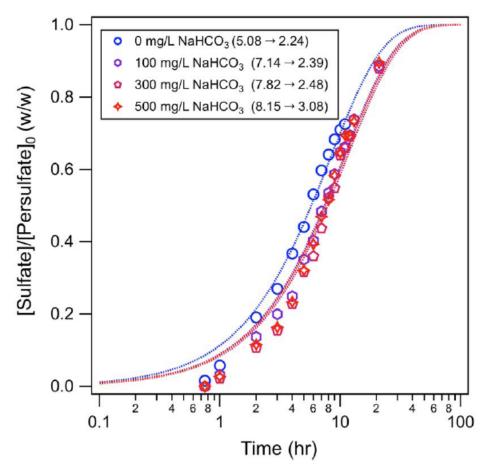


Figure 4. 45. Normalized sulfate concentration as a function of time for a series of bicarbonate concentrations. Experimental conditions: 70°C and an initial 5 mM persulfate concentration. The measured initial and final pH are given in the inset.

The concentration data are represented as mg/L normalized to the initial concentration of persulfate (so the limiting value is 1 as the reaction proceeds to completion), and time is represented on a log scale to resolve the data near the beginning of the reaction. During these experiments, decomposition of persulfate caused the pH in these reactors to decrease—as specified in the caption to Figure 4.45—resulting in a shift in speciation from bicarbonate to carbonate. Nevertheless, all four treatments gave similar kinetic profiles, which were fit to pseudo-first-order appearance kinetics, giving  $k_0 = 0.121 \pm 0.004$ ,  $0.094 \pm 0.003$ ,  $0.088 \pm 0.004$ , and  $0.092 \pm 0.004$ /h for 0, 100, 300, and 500 mg/L NaHCO<sub>3</sub>, respectively. The similarity between these rate constants—and lack of a trend among them—suggest that the rate of persulfate thermolysis is not affected by differences in total (bi)carbonate concentration, (bi)carbonate speciation, or pH (over the range of conditions tested). The range of bicarbonate concentrations tested was chosen to bracket the 50-400 mg/L (0.82-6.6 mM) range that is typical of groundwaters (Matthess 1982).

**Temperature Effects.** Using the same experimental approach used for the effect of initial persulfate and bicarbonate concentrations, we measured the effect of temperature on the appearance of sulfate from thermolysis of persulfate. The results for deionized water are shown in Figure 1 (filled symbols), along with the fits (smooth curves) to pseudo first- order appearance

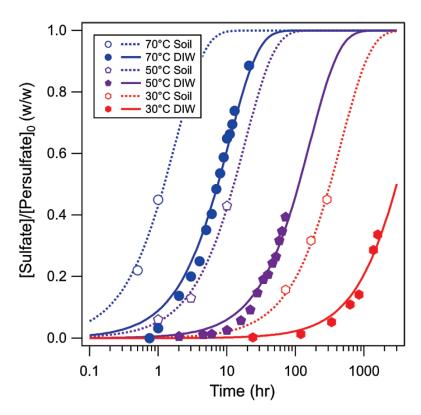


Figure 4. 46. Sulfate appearance (from persulfate decomposition) in un-buffered, deionized water (DIW) at 30, 50, and  $70^{\circ}$ C. Initial persulfate concentration = 5 mM. Soil concentration = 1 g/mL of water.

kinetics. The resulting values of  $k_0$  are  $0.094 \pm 0.003$ ,  $0.0062 \pm 0.0002$ , and  $0.00023 \pm 0.00001/h$  for 70, 50, and 30°C, respectively. Among the many prior studies that have included the effect of temperature on the thermolysis of persulfate in deionized water-based solutions, a few (Block et al., 2004; Goulden & Anthony, 1978; Peyton, 1993; Peyton et al., 1988) have addressed the consistency among results of experiments done under similar conditions (e.g., pH, ionic strength), but there has been no effort to develop a comprehensive kinetic model that covers the whole range of environmentally relevant conditions (especially near-ambient temperatures). Toward this end, we superimposed our data on an Arrhenius plot (Figure 4.47) that includes a selection of the most extensive and relevant data sets from the literature.

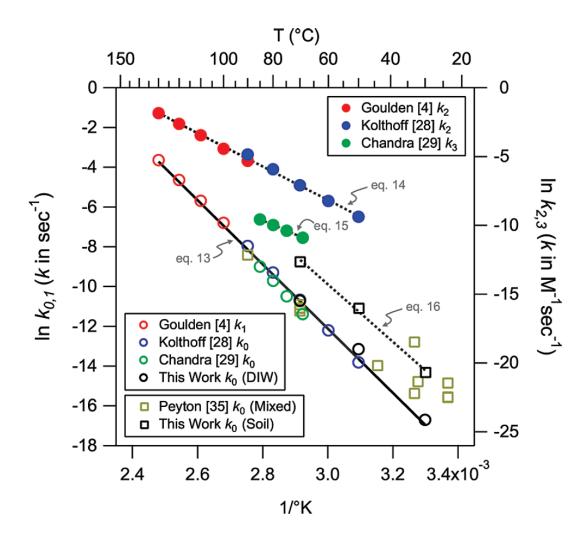


Figure 4. 47. Arrhenius plot for the thermal decomposition of persulfate. Open symbols are the first-order rate constants  $k_0$  and  $k_1$  (left axis) and filled symbols are the second-order rate constants  $k_2$  and  $k_3$  (right axis). The constants  $k_0$ ,  $k_1$ ,  $k_2$ , and  $k_3$  refer to the undifferentiated, neutral-, acid-, and base-initiated pathways, respectively. Squares are media other than deionized water (DIW) and buffered DIW. Lines are the results of fitting performed here on combinations of new and previously published data. The new data shown (black, labeled This Work) correspond to experiments shown in Figure 4.46.

The rate constants for the neutral conditions ( $k_1$  and most  $k_0$ , open circles) and acidcatalyzed ( $k_2$ , filled circles) processes are remarkably consistent despite modest differences between the conditions used in the various studies. Only one set of data is available for alkaline conditions ( $k_3$ , filled green circles), but the reliability of these data is supported by the companion data for  $k_0$  at circum-neutral pH from the same study, which agree well with other data for  $k_0$  and  $k_1$ . The three groups of data for thermal decomposition of persulfate in deionizedwater were fit to the linearized Arrhenius equation (Liang et al., 2003) where k is the rate constant, T is the absolute temperature (in Kelvin), and  $E_A$  is the activation energy (kJ/mol), A is the pre-exponential factor (units of k) and R is the ideal gas constant (8.314 J/(K mol)). The fitted lines shown in Figure 4.47 correspond to eqs. 4.32-4.34.

$$\ln k_1 = (36.6 \pm 0.8) - (134 \pm 2)/RT$$
[4.32]

$$\ln k_2 = (28.3 \pm 1.0) - (101 \pm 3)/RT$$
 [4.33]

$$\ln k_3 = (18.7 \pm 6.6) - (84 \pm 19)/RT \tag{4.34}$$

for  $k_1$  in 1/sec and  $k_2$  and  $k_3$  in 1/(M sec)

These values of  $\ln A$  and  $E_A$  agree well with previously reported values over a range of conditions (cf., Table 5 in House, 1962), but only the newly calculated values include quantitative estimates of uncertainty. Using eqs. [4.32]-[4.34] and equation [3.38], we have plotted  $k_0$  (and the corresponding half-lives) for thermal degradation of persulfate in aqueous solution as a function of pH and temperature in Figure [4.48]. It is apparent from Figure [4.48] that acid- or base-activation requires rather extreme pHs(<3or>12) in order to contribute significantly to persulfate activation during ISCO. Conversely, the increase in persulfate activation with temperature is largely unaffected across the whole pH range found under environmental conditions.

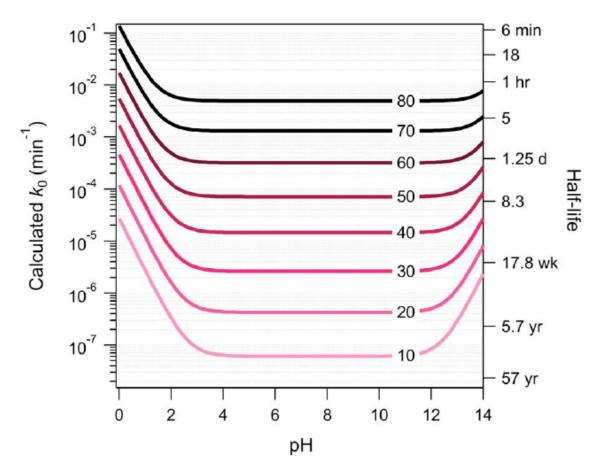


Figure 4. 48.Calculated kinetics of persulfate decay in deionized water as a function of pH and temperature.

**Reactions with Soil.** In water-saturated aquifer materials, the additional reactions associated with natural oxidant demand (NOD) cause the decomposition of persulfate to be faster. This effect on the appearance of sulfate is shown in Figure 4.46 for 1 g soil/mL of water and three temperatures. The pseudo-first-order kinetic model that adequately fit all of our sulfate appearance data obtained in homogeneous aqueous solutions (Figures 4.43-4.45) also was used to fit the data for experiments containing soil. The resulting values for  $k_0$  are  $0.566 \pm 0.047$ ,  $0.055 \pm 0.003$ , and  $0.0022 \pm 0.0001$ /h for 70, 50, and 30°C, respectively. These values are 6-10 times greater than those obtained in the deionized water-only case and presumably would have been even greater for higher concentrations solids or solids with higher organic matter content. The effect of temperature is best seen in Figure [4.47] where we have superimposed the rate constants for experiments in the presence of soil (black squares) on the data for homogeneous aqueous solutions that were discussed above. Fitting the new data to the Arrhenius model gives equation [4.35]

$$\ln k_0 = (33.6 \pm 2.6) - (120 \pm 7)/RT$$
[4.35]

for the temperature dependence of the first-order rate constant for the overall persulfate decomposition rate in water with soil.

From this result, it is notable that the value of  $E_{\rm A}$  is only slightly less than the value obtained for homogeneous aqueous solutions (equation [4.32]) and most of the difference between the two groups of data arises from their pre-exponential terms. In the case represented by equation [4.35], physical interpretation of the fitting parameters, especially the pre-exponential term, is difficult because the parameters represent the combination of processes that contribute to persulfate decomposition in a system containing both water and soil. These processes include (i) the uncatalyzed reaction with water, (ii) reduction by natural organic matter (in this case, introduced with the soil), and possibly (iii) other reactions with mineral surfaces that are not yet well characterized.

Two important distinctions between these processes can be anticipated: increased temperature will favor (i) more than (ii) or (iii) and accumulated exposure to persulfate will eventually exceed the capacity for (ii), but not (i), and (iii) may fall in between. The combination of these effects can be seen in the data for complex media represented by open squares in Figure 4.47. Our data are based on initial rates and reactant concentrations such that the overall NOD should not be affected, so the effect of temperature on k1 is nearly the same as with homogeneous aqueous solutions. In contrast, the data from Peyton et al. (1988) was obtained with low concentrations of an easily oxidized organic solute (benzene) and/or a natural soil, so the  $k_1$ 's they obtained at high temperature are dominated by (i) and at low temperature the trend in their data tails off because persulfate decomposition becomes dominated by the less-temperature dependent processes (ii) and/or (iii).

**Re-spike Experiments.** To better understand how the relative significance of the various processes controlling persulfate decomposition varies with operational factors, batch re-spike experiments were conducted at four initial persulfate concentrations, and the results of these

experiments were modeled with the simple reaction scheme discussed below. The soil used in all of these experiments had permanganate NOD = 0.019 reducing equivalents per gram (determined using the procedure described in the methods section), so this value was used in all of the modeling. Although the reaction between persulfate and soil may involve many reactions and intermediates, a simplified model for the persulfate decomposition process includes the thermal decay of persulfate and the reaction between persulfate and soil NOD.

$$S_2O_8^{2-} \xrightarrow{k_1} 2SO_4^{2-} \tag{4.36}$$

$$S_2O_8^{2-} + NOD \xrightarrow{k_4} 2SO_4^{2-}$$
 [4.37]

These lead to rate expressions of the form

$$\frac{d[S_2O_8^{2-}]}{dt} = -k_4[S_2O_8^{2-}][NOD] - k_1[S_2O_8^{2-}]$$
[4.38]

$$\frac{\mathbf{d[NOD]}}{\mathbf{d}t} = -k_4[S_2O_8^{2-}][NOD]$$
[4.39]

where the concentration units are expressed as millimoles of oxidizing or reducing equivalents per liter of water (e.g., assuming two moles of oxidizing equivalents per mole of persulfate).

The experimental results are shown in Figure 4.49 together with the modeling results for persulfate decomposition due to thermolysis alone (equation [4.36], dashed lines), reaction with NOD equation [4.37], dotted lines), and the net effect (solid lines). The rate constants obtained from this modeling are summarized versus re-spike number in Figure 4.50.

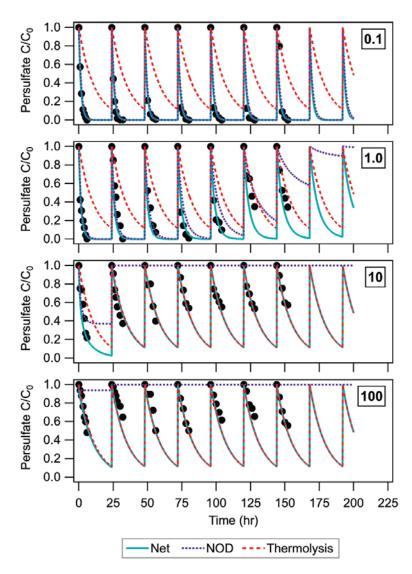


Figure 4. 49. Persulfate disappearance in batch re-spike experiments at  $70^{\circ}\mathrm{C}$  with soil concentration = 0.67 g/ mL. Initial persulfate concentrations (mM) as labeled. Experimental data are shown as circles. Solid blue line represents simulation of the process using a combination of persulfate thermolysis and a second-order reaction between persulfate and the soil oxidant demand. The dashed line represents the modeled decay using only the thermolysis reaction and the dotted line represents persulfate decay using only the second-order reaction.

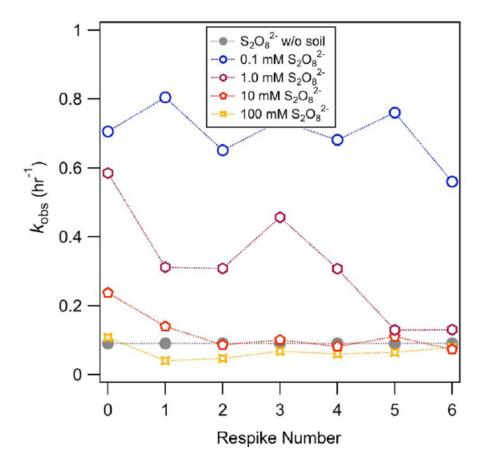


Figure 4. 50. Pseudo first-order disappearance rate constants (kobs) for persulfate in respike experiments (from fitting the experimental data shown in Figure 4.49). All data for batch experiments done at  $70^{\circ}$ C and soil concentration = 0.67 g/mL. Initial persulfate concentrations are given in the legend.

Taken together, the results indicate that (i) the process can be well represented by a combination of first-order thermolysis and second order reaction of persulfate with soil oxidant demand; (ii) once soil NOD is met, reaction rates return to first-order thermolysis values; and (iii) for each individual re-spike, disappearance of persulfate appeared to be pseudo-first order. Thus, the model results indicate that the rate of persulfate consumption by NOD proceeds in a well behaved manner until the NOD is met, and based on this behavior we believe that the persulfate/NOD reaction (equation [4.37]) can be effectively modeled in groundwater systems.

**Persulfate Diffusion into Contaminant Source Zones.** In many groundwater remediation contexts, contact between injected chemical oxidant and contaminant requires diffusion of the oxidant into low-permeability source zones. For thermally activated persulfate, access to diffusion limited source zones may be limited because persulfate decomposition at moderate to high temperatures has half-lives on the order of hours to days (Figure 4.48, Table 4.7). The impact of this can be examined using a simple one-dimensional diffusion model.

Table 4. 7. Kinetic parameters, diffusion coefficients and times to steady state diffusion profiles (days).

temperature (°C)	thermolysis rate constant (s <sup>-1</sup> )	thermolysis half-life (days)	persulfate/NOD second order rate constant (mM L <sup>-1</sup> s <sup>-1</sup> )	effective diffusion coefficient $^{a}$ (cm $^{2}$ s $^{-1}$ )	time to steady-state diffusion profile without NOD reaction <sup>b</sup> (days)	
30	$5.56 \times 10^{-8}$	143.6	$4.96 \times 10^{-8}$	$6.0 \times 10^{-6}$	190	760
50	$1.94 \times 10^{-6}$	4.1	$9.20 \times 10^{-7}$	$6.4 \times 10^{-6}$	13	105
70	$2.22 \times 10^{-5}$	0.36	$1.22 \times 10^{-5}$	$6.8 \times 10^{-6}$	1.5	7

<sup>&</sup>lt;sup>a</sup> Effective diffusion coefficients were approximated as the product of the Wilke-Chang correlation for diffusion in aqueous systems and the tortuosity factor ( $\tau$ ). For the latter it was assumed that  $\tau$  could be represented as porosity to the 4/3<sup>rds</sup> power. <sup>b</sup> Based on visual comparison to the long-term steady state profiles without NOD reactions.

Initial and boundary conditions for the model were (i) the diffusion zone was assumed to be infinitely thick; (ii) initially there was no persulfate in the diffusion zone; (iii) the persulfate concentration at the interface between the advection-dominated and diffusion zones was maintained at 100 mM (200 mM oxidizing equivalents) throughout the simulations; (iv) the soil was assumed to have an initial oxidant demand of 0.019 mmol of reducing equivalents per gram (i.e., the value determined for the soil in the re-spike experiments above); and (v) the soil bulk density and porosity were assumed to be 1.6 g cm-3 and 0.4, respectively. Effective diffusion coefficients used in the model were adjusted to vary linearly with the absolute temperature (i.e., to follow the Stokes-Einstein equation and Wilke-Chang correlation (Logan, 1999)).

Temperature-dependent values of the rate constants for persulfate decomposition by eqations [4.36] and [4.37], determined from the batch experiments discussed above, are listed in Table 4.7. Diffusion and reaction were simulated using an explicit finite difference solution to the following equations:

$$\frac{\partial [S_2 O_8^{2-}]}{\partial t} = D_{\text{Molec}} \frac{\partial^2 [S_2 O_8^{2-}]}{\partial x^2} - k_1 [S_2 O_8^{2-}] - k_4 [S_2 O_8^{2-}] [\text{NOD}]$$
 [4.40]

$$\frac{\partial [\text{NOD}]}{\partial t} = -k_4 [S_2 O_8^{2-}] [\text{NOD}]$$
[4.41]

where  $D_{\mathrm{Molec}}$  is the effective molecular diffusion coefficient (Table 4.7), the persulfate concentration is expressed in moles of oxidizing equivalents per liter of water (i.e., twice the molar concentration), and the aqueous NOD concentration is calculated as the oxidant demand per gram of soil times the bulk density of the soil divided by the porosity. Results of the diffusion modeling are shown in Figure 4.51.

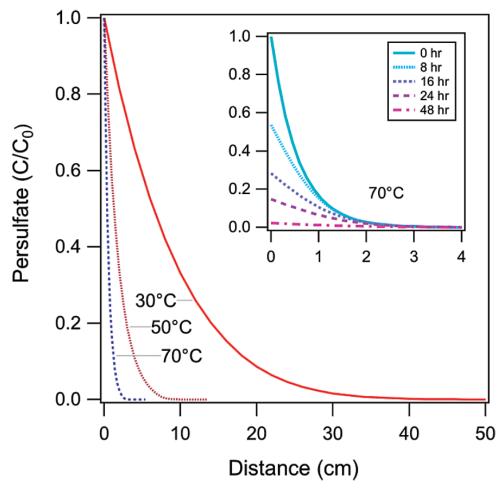


Figure 4. 51. Calculated steady-state diffusion profiles for persulfate in saturated soil without soil oxidant demand. Inset: calculated persulfate concentration profiles vs. time after injection of persulfate stopped.

The curves in the main figure are for persulfate degradation by thermolysis only. They show that the depth of persulfate penetration at elevated temperatures is limited, even in the absence of soil NOD. If the persulfate/ NOD reaction is included, the resulting steady-state profiles are essentially identical to the thermolysis-only cases. However, the time required to reach steady state including NOD are significantly longer than the thermolysis-only case (Table 4.7). As discussed above, the lifetime of persulfate at elevated temperatures is short when compared to transport times. The insert in Figure 4.51 shows concentration profiles for persulfate at 70°C. The 0 h curve represents the steady-state diffusion profile (i.e., the same as in the main figure) where concentration at the diffusion boundary is maintained at a constant value. If the persulfate at that interface is not replenished, the concentration throughout the profile will drop rapidly, and within 48 h the concentration will be near zero throughout the diffusion zone.

Implications for Field Applications. The results presented here have a number of important implications for the application of thermally activated persulfate oxidation. The first is that thermal decomposition of persulfate follows well-behaved kinetics, which should allow the behavior of persulfate to be predicted based on straightforward laboratory feasibility tests using relevant materials. Second, the presence of soil increases the rate at which persulfate decomposes until the soil oxidant demand has been met. Third, once the soil oxidant demand has been met, persulfate continues to degrade via the first-order thermal decomposition reaction. Finally, and perhaps of greatest importance, the lifetime of persulfate (and therefore the availability of sulfate radical) is relatively short at elevated temperatures, which limits the distances over which diffusion of persulfate can be effective and which imposes design constraints on the in situ application of thermally activated persulfate.

### **SECTION 5. CONCLUSIONS AND IMPLICATIONS**

The laboratory experiments and numerical modeling presented here have identified a number of important conclusions regarding low-temperature electrical resistance heating (LTERH). Taken together, the implication is that LTERH has significant potential to improve remediation of DNAPL source zones, especially those for which advective groundwater flow is limited. This is particularly the case for pools of DNAPL, which frequently occur at the tops of low-permeability media and which occur in topographic low points. It also occurs in "diffusion zones" which resulted within low-permeability layers as the result of long-term contact with high-concentration sources. The ability to improve treatment in these zones is important because DNAPL source zones continue to control the timelines for site remediation and many Department of Defense sites.

The experiments and modeling demonstrate several strategies that may prove useful in regard to source zone treatment, and four of them are briefly summarized here:

• LTERH can increase local groundwater flow and, in particular, can substantially increase buoyancy-driven vertical flow

Taking advantage of buoyant flow is of particular importance in heterogeneous systems containing both high and low-permeability zones. Our results indicate that vertical flow across high/low K interfaces can be dramatically increase by heating to temperatures well below the boiling point of water. This can result in order-of-magnitude increases in mass transfer out of the source zone and into zones where groundwater flow rates are much higher.

 Targeted heating to azeotropic boiling temperatures can dramatically increase vertical migration into zones of increased groundwater flow without causing off-gas collection issues.

The ability to deliver heat at specific depths and, in particular, to deliver heat preferentially to lower-permeability zones (because they typically have higher electrical conductivity and because advective flow does not carry heat away from those zones) allows diffusion sources and DNAPL pools to be targeted.

• LTERH can be used to optimize naturally-occurring processes (e.g., bioremediation, dissolution)

Because ERH can be used to produce temperatures anywhere from ambient to  $\sim 100^{\circ}$ C (unlike thermal diffusion and steam that rely on heat sources at  $> 100^{\circ}$ C), LTERH systems can be controlled to optimize a range of processes. At the same time, the lower temperatures reduce infrastructure and energy requirements. For example, using this kind of an approach,

it should be possible to install all of the electrodes needed for LTERH using direct-push equipment and to rely on readily-available power sources (e.g., 3-phase, 220V electrical services) for heating. The hardware and software to control the heating system can be as simple as a laptop PC and an inexpensive data acquisition board, and they allow autonomous operation (The control systems we used for laboratory measurements have the capability to deliver hundreds of amps of current, if needed.) As a result, the operation and maintenance costs for these systems can be very low. However, coupling LTERH with biological process may be problematic because most relevant organisms become significantly less effective at temperatures greater than 30-35°C, and it may be difficult to manage these temperatures using LTERH.

# Delivery of chemical oxidants/reductants to diffusion-limited source zones can be optimized by targeted LTERH

Diffusion-limited source zones typically require long remediation time frames because, by their nature, times required for diffusion of contaminants out of the source will be at least as long as they have existed as sources. For scenarios in which those timeframes are too long, it is possible to deliver reactants into the source by diffusion in order to degrade contaminants while they are still inside the source. Of course, delivery of reactants will also be controlled by diffusion. Here we examined the potential for a thermally-activated reactant (persulfate) to be delivered to a source zone at a temperature that maximized the depth to which the reactant would be effective. In practice, the optimization process is straightforward, because both the reaction rate and the diffusion process can be accurately modeled. One complicating factor in this regard is the consumption of reactant by the aquifer materials. However, our data suggest that, with straightforward laboratory experiments, this process can also be modeled in a predictive fashion.

None of these strategies comes without complicating factors, and the most relevant of these are summarized in Table 5.1. For example, increased subsurface temperatures can lead to increased mobility of DNAPL. This has been observed in numerous physical model experiments, including the ones reported here. However, since most of the applications discussed here involve subsurface temperatures that are well below 100°C, the problem is expected to be less severe than for higher-temperature thermal applications.

The same may not be true for bubble formation and reduction in water permeability. This process can be predicted, at least in a conceptual sense, but additional work on this topic should be an important future research activity.

Tracer tests proved crucial for understanding processes at the laboratory scale, and the argument can be made that this should be true at the field scale as well. In this context, flux measurements at down-gradient wells made before, during and after the heating process should

be considered an essential part of performance assessment for all of the applications discussed above.

Table 5.1. Summary of opportunities and concerns regarding the coupling of LTERH with other in situ remediation processes.

Process/		Lab Test/ Modeling/	Comments on Lab Testing,
<b>Bottom Line</b>	Comments on Process	Data	Modeling and Data
Azeotropic boiling  Bottom Line: Mass removal of DNAPLs with low-boiling azeotropes (e.g., <70oC) can be significantly enhanced with LTERH.	Literature values can be used to determine if azeotropic boiling is practical. In general, if the azeotrope temperature is >85°C, it will be difficult to constrain the boiling zone to where the DNAPL is present. In addition, increasing temperature typically leads to decreased DNAPL viscosity, which can facilitate unintended migration of the DNAPL. So, these concerns should be evaluated based on the amount and distribution of the DNAPL present at the site and the site stratigraphy.	Modeling the heating process; Development of an accurate site conceptual model.	Vapor movement is very complicated to model but it should be possible to estimate the maximum extent of vapor movement based on temperature measurement and modeling. An accurate conceptual model of the site will be important for successful application of azeotropic boiling without an off-gas collection system.
Dissolution  Bottom Line: Generally has a minor effect.	Increases in solubility due to heating are generally not large (e.g., <2X). In this context, increased dissolution may come mostly from increased flow due to density and viscosity changes in the water.	Literature data on solubility.	Data are available for solubility as a function of temperature and, as a result, laboratory measurements are generally not required. The greatest uncertainty in the context of dissolution is the degree of contact between the flowing water and DNAPL. As a first approximation, however, it can be assumed that dissolved concentrations will increase in proportion to the increase in solubility.

Process	Comments on Process	Lab Test/ Modeling/ Data	Comments on Lab Testing,  Modeling and Data
Biodegradation  Bottom Line: Generally limited to <35°C.  Difficult to implement with LTERH.	Biodegradation can increase rapidly when temperatures are raised from 10 to ~35°C. However, beyond this range biodegradation rates frequently drop rapidly. As a consequence, using LTERH to increase biodegradation rates will, in general, be more difficult than for abiotic reactions. Alternate heating approaches (e.g., hot water injection) may be better suited to thermal enhancement of biodegradation.		Difficult to implement with LTERH.
Enhanced flow  Bottom Line: Heating can enhance dissolution from DNAPL pools. Not beneficial for diffusion sources.	Water viscosity and density decrease significantly with heating. As a consequence, heating localized around a source zone can significantly increase local flow within the higher-permeability portions of the source. However, if diffusion-limited zones represent an important component of the source, the effects of increased temperature on flow may be minimal. (In addition, while diffusion coefficients increase with increasing temperature, those increases are also generally small).	Modeling of heating and groundwater flow; Estimation of the role of entrapped vapor	Modeling of enhanced flow during heating can be successfully modeled with SEAWAT. Successful modeling will depend on accurate information on both the hydraulic conductivity structure of the aquifer and the distribution of the DNAPL. In some media, bubble formation can inhibit water flow (e.g., when stratification entraps significant volumes of vapor) and this can have an inhibitory effect on water flow. An accurate conceptual model for the site is important in this context.
In situ chemical reaction  Bottom Line: Heating enhances rates but can shorten reactant lifetime.	For many chemical reactions, including those commonly used for in situ remediation, reaction rates double with every 10°C increase in temperature. Unlike biodegradation, however, rates continue to increase even as boiling temperatures are approached. However, this increase in reaction rate may be accompanied by a decrease in reactant lifetime, which may limit its delivery in the subsurface.	Laboratory reactant demand measurements	Aquifer solids can vary significantly in their ability to consume injected reactants. In addition, depending on the reactant, the rate at which the reactant is consumed can vary significantly with temperature. As a consequence, laboratory testing of reactant demand for the solids/reactant combination is recommended. This is discussed in Section 4 of this report.

Table 5.1. (cont)

#### **SECTION 6 REFERENCES**

- ASTM. (2007). Standard Test Method for Estimating the Permanganate Natural Oxidant Demand of Soil and Aquifer Solids.
- Anderson, M. R. R., Johnson, R. L., & Pankow, J. F. (1992). Dissolution of Dense Chlorinated Solvents into Ground Water: 1. Dissolution from a Well-Defined Residual Source. *Ground Water*, 30(2), 250-256. Wiley Online Library.
- Anipsitakis, G. P., Dionysiou, D. D., & Gonzalez, M. a. (2006). Cobalt-mediated activation of peroxymonosulfate and sulfate radical attack on phenolic compounds. implications of chloride ions. *Environmental science & technology*, 40(3), 1000-7.
- Archie, G. (1942). The electrical resistivity log as an aid in determining some reservoir characteristics. *Trans. Am. Inst. Min. Metall. Pet. Eng.*, *146*, 54–62.
- Arps, J. (1953). The effect of temperature on the density and electrical resistivity of sodium chloride solutions. *Trans. AIME*, *198*, 327–330.
- Bachu, S. (1995). Flow of variable-density formation water in deep sloping aquifers: review of methods of representation with case studies. *Journal of Hydrology*, *164*(1-4), 19–38. Elsevier.
- Baker, R. S., & Hiester, U. (2009). Large-Scale Physical Models of Thermal Remediation of DNAPL Source Zones in Aquitards. SERDP Project ER-1423.
- Banerjee, M., & Konar, R. S. (1984). Comment on the paper "polymerization of acrylonitrile initiated by K2S2O8-Fe(II) redox system." *Journal of Polymer Science: Polymer Chemistry Edition*, 22(5), 1193-1195. doi:10.1002/pol.1984.170220519
- Beyke, G., & Fleming, D. (2005). In situ thermal remediation of DNAPL and LNAPL using electrical resistance heating. *Remediation Journal*, 15(3), 5–22. Wiley Online Library.
- Block, P. A., Brown, R. A., & Robinson, D. (2004). Novel activation technologies for sodium persulfate in situ chemical oxidation. *Proceedings of the 4th International Conference on the Remediation of Chlorinated and Recalcitrant Compounds* (p. 2A-05).
- Boulding, J. R., & Ginn, J. S. (2004). *Practical Handbook of Soil, Vadose Zone and Ground-Water Contamination, Assessment, Prevention, and Remediation*. A.F. Lewis, New York.

- Brooks, M. C., Wise, W. R., & Annable, M. D. (1999). Fundamental Changes in In Situ Air Sparging How Patterns. *Ground Water Monitoring & Remediation*, 19(2), 105–113. Wiley Online Library.
- Brown, R. A., Robinson, David, Skladany, G., & Loeper, J. (2004). Response to naturally occurring organic material: permanganate versus persulfate. *Proceedings of the Fourth International Conference of Remediation of Chlorinated and Recalcitrant Compounds (Monterey, CA, May 24-27, 2004), (Gavaskar, AR, and Chen, ASC, Eds.), Battelle Press, Columbus, Ohio.*
- Buettner, H. M., & Daily, W. D. (1995). Cleaning contaminated soil using electrical heating and air stripping. *Journal of Environmental Engineering*, 121, 580.
- Butler, D. D. B., & Knight, R. J. (1998). Electrical conductivity of steam-flooded, clay-bearing geologic materials. *Geophysics*, 63(4), 1137-1149. Society of Exploration Geophysicists.
- Canonica, S., & Tratnyek, Paul G. (2003). Quantitative Structure–Activity Relationships for Oxidation Reactions of Organic Chemicals in Water. *Environmental Toxicology and Chemistry*, 22(8), 1743. doi:10.1897/01-237
- Carrigan, C., & Nitao, J. (2000). Predictive and diagnostic simulation of in situ electrical heating in contaminated, low-permeability soils. *Environmental science & technology*, *34*(22), 4835–4841. ACS Publications.
- Chandra Singh, U. (1976). Decomposition of peroxodisulphate in aqueous alkaline solution. *Journal of Inorganic and Nuclear Chemistry*, 38(3), 541-543. doi:10.1016/0022-1902(76)80300-4
- Chawla, O. P., & Fessenden, R. W. (1975). Electron spin resonance and pulse radiolysis studies of some reactions of SO4. *J. Phys. Chem*, 79(24), 2693–2700.
- Chiang, W. H. (2005). 3D-groundwater modeling with PMWIN, Second Edition. Springer.
- Costanza, J. (2005). Degradation of tetrachloroethylene and trichloroethylene under thermal remediation conditions. Georgia Institute of Technology.
- Costanza, Jed, Davis, Eva L, Mulholland, J. a, & Pennell, Kurt D. (2005). Abiotic degradation of trichloroethylene under thermal remediation conditions. *Environmental science & technology*, *39*(17), 6825-30.
- Costanza, Jed, Otaño, G., Callaghan, J., & Pennell, Kurt D. (2010). PCE oxidation by sodium persulfate in the presence of solids. *Environmental science & technology*, 44(24), 9445-50. doi:10.1021/es100997a
- Couttenye, R. A., Huang, K. C., Hoag, G. E., & Suib, S. L. (2002). Evidence of sulfate free radical (SO4-•) formation under heat-assisted persulfate oxidation of MTBE. *Proceedings*

- of the 19th Petroleum Hydrocarbons and Organic Chemicals in Ground Water: Prevention, Assessment, and Remediation, 345–350.
- Czapski, G., Lymar, S. V., & Schwarz, H. a. (1999). Acidity of the Carbonate Radical. *The Journal of Physical Chemistry A*, 103(18), 3447-3450. doi:10.1021/jp984769y
- Dahmani, M. A., Huang, K., & Hoag, G. E. (2006). Sodium persulfate oxidation for the remediation of chlorinated solvents (USEPA superfund innovative technology evaluation program). *Water, Air, & Soil Pollution: Focus, 6*(1), 127–141. Springer. doi:10.1007/s11267-005-9002-5
- Davies, M. J., & Gilbert, B. C. (1984). Electron spin resonance studies. Part 68. Addition versus overall one-electron abstraction in the oxidation of alkenes and dienes by SO 4–<sup>-</sup>, Cl 2–<sup>-</sup>, and OH in acidic aqueous solution. *J. Chem. Soc.*, *Perkin Trans.* 2, (11), 1809–1815. The Royal Society of Chemistry.
- Davis, E.L. (1997). How heat can enhance in-situ soil and aquifer remediation: Important chemical properties and guidance on choosing the appropriate technique. United States Environmental Protection Agency, Office of Research and Development, Office of Solid Waste and Emergency Response: Superfund Technology Support Center for Ground Water, National Risk Management Research Laboratory, Subsurface Protection and.
- Davis, E.L. (1998). *Steam injection for soil and aquifer remediation*. Superfund Technology Support Center for Ground Water, Robert S. Kerr Environmental Research Laboratory.
- Dekker, T., & Abriola, L. M. (2000). The influence of field-scale heterogeneity on the surfactant-enhanced remediation of entrapped nonaqueous phase liquids. *Journal of Contaminant Hydrology*, 42(2-4), 219-251. doi:10.1016/S0169-7722(99)00091-1
- Diersch, H. J. G., & Kolditz, O. (2002). Variable-density flow and transport in porous media: approaches and challenges. *Advances in water resources*, 25(8-12), 899–944. Elsevier.
- ESTCP. (2011). Application of Nucleic Acid-Based Tools for Monitoring Monitored Natural Attenuation (MNA), Biostimulation and Bioaugmentation at Chlorinated Solvent Sites. ESTCP ER-200518.
- Fletcher, K. E., Costanza, Jed, Cruz-Garcia, C., Ramaswamy, N. S., Pennell, Kurt D, & Löffler, F. E. (2011). Effects of elevated temperature on Dehalococcoides dechlorination performance and DNA and RNA biomarker abundance. *Environmental science & technology*, 45(2), 712-8. doi:10.1021/es1023477
- Fountain, J. C. (1998). Technologies for dense nonaqueous phase liquid source zone remediation. *Technology Evaluation Report TE-98-02. Pittsburgh, PA: Ground-Water Remediation Technologies Analysis Center*, 15238(December). Citeseer.

- Frenzel, H. (1995). A field generator based on Mejia's algorithm. *Institut fr Umweltphysik, University of Heidelberg, Germany*.
- Friedman, S. P. (2005). Soil properties influencing apparent electrical conductivity: A review. *Computers and electronics in agriculture*, 46(1-3), 45–70. Elsevier.
- Frigerio, N. A. (1963). An Iodometric Method for the Macro-and Microdetermination of Peroxydisulfate. *Analytical Chemistry*, *35*(3), 412–413. ACS Publications.
- Friis, A. K., Edwards, E., Albrechtsen, H.-J. H. J., Udell, K. S., Duhamel, M., Bjerg, P. L. L., & Friis, K. (2007). Dechlorination after thermal treatment of a TCE-contaminated aquifer: laboratory experiments. *Chemosphere*, 67(4), 816–825. Elsevier. doi:10.1016/j.chemosphere.2006.10.012
- Friis, A. K., Heron, G., Albrechtsen, H. J., Udell, K., & Bjerg, P. L. (2006). Anaerobic dechlorination and redox activities after full-scale Electrical Resistance Heating (ERH) of a TCE-contaminated aquifer. *Journal of contaminant hydrology*, 88(3-4), 219–234. Elsevier.
- Frind, E. O. (1982). Simulation of long-term transient density-dependent transport in groundwater. *Advances in Water Resources*, 5(2), 73–88. Elsevier.
- Fry, V. A., Selker, J., & Gorelick, S.M. (1997). Experimental investigations for trapping oxygen gas in saturated porous media for in situ bioremediation. *Water resources research*, *33*(12), 2687–2696. American Geophysical Union. doi:10.1029/97WR02428
- Gebhart, B., Yogesh, J., Roop, L. M., & Bahgat, S. (1988). *Buoyancy-Induced Flows and Transport*. Hemisphere, New York.
- Gerhard, J., & Kueper, B. (2003). Capillary pressure characteristics necessary for simulating DNAPL infiltration, redistribution, and immobilization in saturated porous media. *Water resources research*, 39(8), 1212. American Geophysical Union.
- Glass, R. J., Conrad, S. H., & Yarrington, L. (2001). Gravity-destabilized nonwetting phase invasion in macroheterogeneous porous media: near-pore-scale macro modified invasion percolation simulation of experiments. *Water resources research*, *37*(5), 1197–1207. American Geophysical Union.
- Gmehling, J., Onken, U., & Arlt, W. (1977). *Vapor-Liquid Equilibrium Data Collection: Aqueous-Organic Systems* (Vol. 1). Dechema.
- Gori, F., Marino, C., & Pietrafesa, M. (2001). Experimental measurements and theoretical predictions of the thermal conductivity of two phases glass beads. *International communications in heat and mass transfer*, 28(8), 1091–1102. Elsevier.
- Gossett, J. M. (1987). Measurement of Henry's law constants for C1 and C2 chlorinated hydrocarbons. *Environmental Science & Technology*, 21(2), 202–208. ACS Publications.

- Goulden, P., & Anthony, D. (1978). Kinetics of uncatalyzed peroxydisulfate oxidation of organic material in fresh water. *Analytical Chemistry*, *50*(7), 953–958. ACS Publications.
- Haselow, J. S., Siegrist, R. L., Crimi, M. L., & Jarosch, T. (2003). Estimating the total oxidant demand for in situ chemical oxidation design. *Remediation Journal*, *13*(4), 5–16. Wiley Online Library. doi:10.1002/rem.10080
- Henry, P. (1997). Relationship between porosity, electrical conductivity, and cation exchange capacity in Barbados wedge sediments. *Proceedings of the Ocean Drilling Program. Scientific results* (Vol. 156, pp. 137–149). Ocean Drilling Program.
- Heron, G., Carroll, S., & Nielsen, S. G. (2005). Full-Scale Removal of DNAPL Constituents Using Steam-Enhanced Extraction and Electrical Resistance Heating. *Ground Water Monitoring & Remediation*, 25(4), 92–107. Wiley Online Library. doi:10.1111/j.1745-6592.2005.00060.x
- Hiebert, A. D. (1987). Numerical simulation of the electric pre-heat and steam drive bitumen recovery process for the Athabasca oil sands. Ph.D. Dissertation. Univ. Alberta, Canada.
- Hiebert, A., Vermeulen, F., & Chute, F. (1989). Application of numerical modelling to the simulation of the electric-preheat steam-drive (EPSD) process in Athabasca oil sands. *Journal of Canadian Petroleum Technology*, 28(5). Society of Petroleum Engineers.
- Hiebert, AD, Vermeulen, FE, Chute, FS, & Capjack, C. (1986). Numerical simulation results for the electrical heating of athabasca oil-sand formations. *SPE Reservoir Engineering*, *1*(1), 76–84. Society of Petroleum Engineers.
- House, D. A. (1962). Kinetics and Mechanism of Oxidations by Peroxydisulfate. *Chemical Reviews*, 62(3), 185-203. doi:10.1021/cr60217a001
- Huang, K. C., Hoag, G. E., Chheda, P., Woody, B. A., & Dobbs, G. M. (2001). Oxidation of chlorinated ethenes by potassium permanganate: A kinetics study. *Journal of hazardous materials*, 87(1-3), 155–169. Elsevier.
- Huang, K. C., Zhao, Z., Hoag, G. E., Dahmani, A., & Block, P. A. (2005). Degradation of volatile organic compounds with thermally activated persulfate oxidation. *Chemosphere*, 61(4), 551–560. Elsevier.
- Huie, R. E., & Clifton, C. L. (1993). Kinetics of the self-reaction of hydroxymethylperoxyl radicals. *Chemical physics letters*, 205(2-3), 163–167. Elsevier.
- ITRC. (2005). Technical and Regulatory Guidance for in Situ Chemical Oxidation of Contaminated Soil and Groundwater. Second Edition.

- Jeffers, P. M., Ward, L. M., Woytowitch, L. M., & Wolfe, N. L. (1989). Homogeneous hydrolysis rate constants for selected chlorinated methanes, ethanes, ethenes, and propanes. *Environmental science & technology*, 23(8), 965–969. ACS Publications.
- Jiang, P. Y., Katsumura, Y., Nagaishi, R., Domae, M., Ishikawa, K., Ishigure, K., & Yoshida, Y. (1992). Pulse radiolysis study of concentrated sulfuric acid solutions. Formation mechanism, yield and reactivity of sulfate radicals. *J. Chem. Soc.*, *Faraday Trans.*, 88(12), 1653–1658. The Royal Society of Chemistry.
- Johnson, P., Dahlen, P., Triplett, J., Foote, E., & Williams, S. (2009). Critical Evaluation of State-of-the-Art In Situ Thermal Treatment Technologies for DNAPL Source Zone Treatment. ESTCP Project ER-0314. Technology.
- Johnson, R. L., & Pankow, J. F. (1992). Dissolution of dense chlorinated solvents into groundwater. 2. Source functions for pools of solvent. *Environmental science & technology*, 26(5), 896–901. ACS Publications.
- Johnson, R. L., Tratnyek, P.G., & Johnson, R. O. (2008). Persulfate persistence under thermal activation conditions. *Environmental science & technology*, 42(24), 9350–9356. ACS Publications.
- Jones, L., Xu, X., Thomson, N., Waldemer, R., & Tratnyek, P. (2006). The impact of permanganate NOD kinetics on treatment efficiency. *Proceedings of the 5 th International Conference on Remediation of Chlorinated and Recalcitrant Compounds, Monterey, CA, May* (pp. 22–25).
- Jussel, P., Stauffer, F., & Dracos, T. (1994). Transport modeling in heterogeneous aquifers: 1. Statistical description and numerical generation of gravel deposits. *Water resources research*, 30(6), 1803–1817. American Geophysical Union.
- Kiva, V., Hilmen, E., & Skogestad, S. (2003). Azeotropic phase equilibrium diagrams: a survey. *Chemical Engineering Science*, *58*(10), 1903–1953. Elsevier.
- Knauss, K. G., Dibley, M. J., Leif, R. N., Mew, D. A., & Aines, R. D. (2000). The aqueous solubility of trichloroethene (TCE) and tetrachloroethene (PCE) as a function of temperature. *Applied geochemistry*, *15*(4), 501–512. Elsevier.
- Kolthoff, I., & Miller, I. (1951). The Chemistry of Persulfate. I. The Kinetics and Mechanism of the Decomposition of the Persulfate Ion in Aqueous Medium1. *Journal of the American Chemical Society*, 73(7), 3055–3059. ACS Publications.
- Koltzenburg, G., Behrens, G., & Schulte-Frohlinde, D. (1982). Fast hydrolysis of alkyl radicals with leaving groups in the position. *Journal of the American Chemical Society*, 104(25), 7311–7312. ACS Publications.

- Konz, M., Younes, A., Ackerer, P., Fahs, M., Huggenberger, P., & Zechner, E. (2009). Variable-density flow in heterogeneous porous media–Laboratory experiments and numerical simulations. *Journal of contaminant hydrology*, *108*(3-4), 168–175. Elsevier.
- Kozdon, J., Gerritsen, M., & Christie, M. (2008). Grid Orientation Revisited: Near-well, Early-time Effects and Solution Coupling Methods. *Transport in Porous Media*, 73(3), 255–277. Springer.
- Krol, M. M., Sleep, B. E., & Johnson, R. L. (2011). Impact of low-temperature electrical resistance heating on subsurface flow and transport. *Water Resources Research*, 47(5). doi:10.1029/2010WR009675
- Krol, M.M., Mumford, K.G., Johnson, R. L., & Sleep, B.E. (2011). Modeling discrete gas bubble formation and mobilization during subsurface heating of contaminated zones. *Advances in Water Resources*, *34*(4), 537-549. Elsevier. doi:10.1016/j.advwatres.2011.01.010.
- Kueper, B. (1990). The behaviour of dense, non-aqueous phase liquid contaminants in heterogeneous porous media. Ph.D. Dissertation. University of Waterloo.
- Kueper, B. H., & Frind, E. O. (1988). An overview of immiscible fingering in porous media. *Journal of contaminant Hydrology*, 2(2), 95–110. Elsevier.
- Kueper, B. H., & McWhorter, D. B. (1992). The use of macroscopic percolation theory to construct large-scale capillary pressure curves. *Water resources research*, 28(9), 2425–2436. American Geophysical Union.
- Kulongoski, J. T., Belitz, K., & Dawson, B. J. (2006). Ground-Water Quality Data in the North San Francisco Bay Hydrologic Provinces, California, 2004: Results from the California Ground-Water Ambient Monitoring and Assessment (GAMA) Program. Assessment.
- Langevin, C. D. C. D., & Guo, W. (2006). MODFLOW/MT3DMS-based simulation of variable-density ground water flow and transport. *Ground water*, 44(3), 339-51. doi:10.1111/j.1745-6584.2005.00156.x
- Leverett, M. (1940). Capillary behavior in porous solids. *Transactions AIME*, petroleum division, 142(October), 152-169.
- Li, X., & Yortsos, Y. (1995). Theory of multiple bubble growth in porous media by solute diffusion. *Chemical engineering science*, 50(8), 1247–1271. Elsevier.
- Liang, C. J., Bruell, C. J., & Marley, M. C. (2003). Thermally activated persulfate oxidation of trichloroethylene (TCE) and 1, 1, 1-trichloroethane (TCA) in aqueous systems and soil slurries. *Soil and Sediment*, *12*(2), 207-228. doi:10.1080/713610970

- Liang, C., Bruell, C., Marley, M., & Sperry, K. L. (2004a). Persulfate oxidation for in situ remediation of TCE. II. Activated by chelated ferrous ion. *Chemosphere*, *55*(9), 1225-33. doi:10.1016/j.chemosphere.2004.01.030
- Liang, C., Bruell, C., Marley, M., & Sperry, K. L. (2004b). Persulfate oxidation for in situ remediation of TCE. I. Activated by ferrous ion with and without a persulfate-thiosulfate redox couple. *Chemosphere*, *55*(9), 1213-23. doi:10.1016/j.chemosphere.2004.01.029
- Lide, D. R. (2006). CRC handbook of chemistry and physics: a ready-reference book of chemical and physical data. CRC Press.
- Logan, B. E. (1999). Environmental transport processes. New York. Wiley-Interscience.
- Looney, B. B., & Falta, R. W. (2002). *Vadose Zone Science and Technology Solutions. Vadose Zone Journal* (Vol. 1, p. 199). Battelle, Columbus, OH.
- Markle, J. M., Schincariol, R. A., Sass, J. H., & Molson, J. W. (2006). Characterizing the two-dimensional thermal conductivity distribution in a sand and gravel aquifer. *Soil Science Society of America Journal*, 70(4), 1281–1294. Citeseer.
- Matthess, G. (1982). *The Properties of Groundwater. EOS Transactions* (Vol. 64). Wiley: New York,.
- McElroy, W., & Waygood, S. J. (1990). Kinetics of the Reactions of the. *J. Chem. Soc., Faraday Trans.*, 86(14), 2557-2564.
- McGee, B., & Vermeulen, F. (2007). The mechanisms of electrical heating for the recovery of bitumen from oil sands. *Journal of Canadian Petroleum Technology*, 46(1). Society of Petroleum Engineers.
- McNeill, J. (1980). Electrical conductivity of soils and rocks. Tech. note TN-5. Geonics Ltd., Mississauga, ON, Canada.
- Mejia, J. M., & Rodriguez-Iturbe, I. (1974). On the synthesis of random field sampling from the spectrum: an application to the generation of hydrologic spatial processes. *Water Resources Research*, 10(4), 705–711. American Geophysical Union.
- Michaeli, W. (2003). Extrusion dies for plastics and rubber: design and engineering computations. Hanser Gardner Publications.
- Minisci, F., Citterio, A., & Giordano, C. (1983). Electron-transfer processes: peroxydisulfate, a useful and versatile reagent in organic chemistry. *Accounts of Chemical Research*, *16*(1), 27-32. ACS Publications.

- Molson, J. W., Frind, E. O., & Palmer, C. D. (1992). Thermal energy storage in an unconfined aquifer: 2. Model development, validation, and application. *Water Resources Research*, 28(10), 2857–2867. American Geophysical Union.
- Morel-Seytoux, H. J., Meyer, P. D., Nachabe, M., Tourna, J., van Genuchten, M. T., & Lenhard, R. J. (1996). Parameter Equivalence for the Brooks-Corey and Van Genuchten Soil Characteristics: Preserving the Effective Capillary Drive. *Water Resources Research*, 32(5), 1251. doi:10.1029/96WR00069
- Mumford, Kevin G, Thomson, N. R. N. R., & Allen-King, R. M. (2005). Bench-scale investigation of permanganate natural oxidant demand kinetics. *Environmental science & technology*, 39(8), 2835-40.
- Mumford, K., Thomson, N., & Allen-King, R. (2003). Investigating the kinetic nature of natural oxidant demand during ISCO. *Third International Conference on Remediation of Chlorinated and Recalcitrant Compounds (Monterey, CA; May 2002). ISBN 1-57477-132-9, published by Battelle Press, Columbus, OH* (p. 2002).
- Mumford, K.G., Dickson, S. E., & Smith, J. E. (2009). Slow gas expansion in saturated natural porous media by gas injection and partitioning with non-aqueous phase liquids. *Advances in Water Resources*, 32(1), 29–40. Elsevier.
- Mumford, K.G., Smith, J. E., & Dickson, S. E. (2009). New observations of gas-phase expansion above a dense nonaqueous phase liquid pool. *Vadose Zone Journal*, 8(2), 404. Soil Sci Soc America.
- Mumford, K.G., Smith, J. E., & Dickson, S. E. (2010). The effect of spontaneous gas expansion and mobilization on the aqueous-phase concentrations above a dense non-aqueous phase liquid pool. *Advances in Water Resources*, *33*(4), 504–513. Elsevier.
- Munson, B. R. (2002). Fundamentals of Fluid Mechanics. John Wiley, New York.
- National Research Council. (2005). *Contaminants in the Subsurface: Source Zone Assessment and Remediation*. National Academies.
- Neta, P., Madhavan, V., Zemel, H., & Fessenden, R. W. (1977). Rate constants and mechanism of reaction of sulfate radical anion with aromatic compounds. *Journal of the American Chemical Society*, 99(1), 163–164. ACS Publications.
- Ogata, A. (1970). Theory of dispersion in a granular medium. USGS Professional Paper 34.
- O'Carroll, D.M., & Sleep, B.E. (2007). Hot water flushing for immiscible displacement of a viscous NAPL. *Journal of contaminant hydrology*, 91(3-4), 247–266. Elsevier.

- O'Carroll, Denis M, & Sleep, B.E. (2009). Role of NAPL Thermal Properties in the Effectiveness of Hot Water Flooding. *Transport in porous media*, 79(3), 393–405. Springer. doi:10.1007/s11242-008-9329-2
- Pankow, J. F., & Johnson, R. L. (1996). Physical and chemical properties of dense non-aqueous phase liquid. *Dense chlorinated solvents and other DNAPLs in groundwater*. (pp. 507-512).
- Pennell, K.D., Löffler, F. E., Costanza, Jed, Fletcher, K. E., Ramaswamy, N. S., Otano, G., & Callaghan, J. (2009). *Investigation of Chemical Reactivity, Mass Recovery and Biological Activity During Thermal Treatment of DNAPL Source Zones. Distribution.*
- Peyton, G. R. (1993). The free-radical chemistry of persulfate-based total organic carbon analyzers. *Marine chemistry*, 41(1-3), 91–103. Elsevier. doi:10.1016/0304-4203(93)90108-Z
- Peyton, G. R., LeFaivre, M. H., & Smith, M. A. (1988). In Situ Aquifer Reclamation by Chemical Means: A Feasibility Study.
- Poling, B. E., Prausnitz, J. M., & O'Connell, J. P. (2001). The properties of gases and liquids. McGraw Hill Book Co., New York, NY.
- Reid, R. C., Prausnitz, J. M., & Poling, B. E. (1987). *The properties of gases and liquids*. McGraw Hill Book Co., New York, NY.
- Richardson, R., James, C., Bhupathiraju, V., & Alvarez-Cohen, L. (2002). Microbial activity in soils following steam treatment. *Biodegradation*, 13, 285–295.
- Robinson, David, Brown, R., Dablow, J., & Rowland, K. (2004). Chemical oxidation of MGP residuals and dicyclopentadiene at a former MGP site. *Proceedings of the Fourth International Conference on the Remediation of Chlorinated and Recalcitrant Compounds, Monterey, Calif.*
- Rossman, A. J., Hayden, N. J., & Rizzo, D. M. (2006). Low-temperature soil heating using renewable energy. *Journal of Environmental Engineering*, 132, 537.
- SERDP/ESTCP. (2001). SERDP/ESTCP Expert Panel Workshop on Research and Development Needs for Cleanup of Chlorinated Solvent Sites.
- Selker, J. S., Niemet, M., Mcduffie, N. G., Gorelick, Steven M., & Parlange, J.-Y. (2006). The Local Geometry of Gas Injection into Saturated Homogeneous Porous Media. *Transport in Porous Media*, 68(1), 107-127. doi:10.1007/s11242-006-0005-0
- Sen, P. N. (1992). Influence of temperature on electrical conductivity on shaly sands. *Geophysics*, 57(1), 89. doi:10.1190/1.1443191

- Sen, P. N., Goode, P. A., & Sibbit, A. (1988). Electrical conduction in clay bearing sandstones at low and high salinities. *Journal of Applied Physics*, 63(10), 4832. doi:10.1063/1.340476
- Seol, Y., Zhang, H., & Schwartz, F. W. (2003). A Review of In Situ Chemical Oxidation and Heterogeneity. *Environmental and Engineering Geoscience*, 9(1), 37. Assoc Eng Geologists.
- Siegrist, R. L., Urynowicz, M. A., West, O. R., Crimi, M. L., & Lowe, K. S. (2001). *Principles and practices of in situ chemical oxidation using permanganate* (Vol. 505). Battelle Press Columbus, OH.
- Sleep, B., & Sykes, J. (1989). Modeling the transport of volatile organics in variably saturated media. *Water Resources Research*, 25(1), 81–92. American Geophysical Union.
- Stroo, H. F., Unger, M., Ward, C., Kavanaugh, M., & Vogel, C. (2003). Remediating chlorinated solvent source zones. *Environ. Sci. Technol*, *37*, 225A-230A.
- Sudicky, E. A. (1986). A natural gradient experiment on solute transport in a sand aquifer: Spatial variability of hydraulic conductivity and its role in the dispersion process. *Water Resources Research*, 22(13), 2069–2082. American Geophysical Union.
- U.S. EPA. (2004). In Situ Thermal Treatment of Chlorinated Solvents: Fundamentals and Field Applications. Environmental Protection.
- Urynowicz, M., Balu, B., & Udayasankar, U. (2008). Kinetics of natural oxidant demand by permanganate in aquifer solids. *Journal of contaminant hydrology*, *96*(1-4), 187-94. doi:10.1016/j.jconhyd.2007.11.001
- Vinsome, K., W. McGee, B., Vermeulen, F., & Chute, F. (1994). Electrical Heating. *Journal of Canadian Petroleum Technology*, 33(4). doi:10.2118/94-04-04
- Wagner, G., Meakin, P., Feder, J., & J\kussang, T. (1997). Buoyancy-driven invasion percolation with migration and fragmentation. *Physica A: Statistical and Theoretical Physics*, 245(3-4), 217–230. Elsevier.
- Waldemer, Rachel H, Tratnyek, P.G., Johnson, R. L., & Nurmi, J. T. (2007). Oxidation of chlorinated ethenes by heat-activated persulfate: kinetics and products. *Environmental science & technology*, 41(3), 1010-5.
- Waldemer, R.H., & Tratnyek, P.G. (2006). Kinetics of contaminant degradation by permanganate. *Environmental science & technology*, 40(3), 1055–1061. ACS Publications.
- Watts, R. J., & Teel, A. L. (2006). Treatment of contaminated soils and groundwater using ISCO. *Practice Periodical of Hazardous, Toxic, and Radioactive Waste Management, 10, 2.*

- Waxman, M., & Smits, L. (2003). Electrical conductivities in oil-bearing shaly sands. *SPE REPRINT SERIES*, 107–122. THE SOCIETY OF PETROLEUM ENGINEERS.
- Wilmarth, W. K., & Haim, A. (1962). Mechanisms of oxidation by peroxydisulfate ion. In E. Edwards, J. O. (Ed.), *Peroxide Reaction Mechanisms*. John Wiley & Sons.
- Woodbury, A. D., & Sudicky, E. (1991). The geostatistical characteristics of the Borden aquifer. *Water Resources Research*, 27(4), 533–546. American Geophysical Union.
- Xheng, C., Wang, P. P., & Zheng, C. (1999). MT3DMS: A modular three-dimensional multispecies transport model for simulation of advection, dispersion, and chemical reactions of contaminants in groundwater systems; Documentation and user's guide. Contract Report SERDP-99-1. Citeseer.
- Yang, J., & Edwards, R. (2000). Predicted groundwater circulation in fractured and unfractured anisotropic porous media driven by nuclear fuel waste heatgeneration. *Canadian Journal of Earth Sciences/Revue Canadienne des Sciences de la Terre*, 37(9), 1301–1308.
- Yaws, C., & Yang, H. (1989). To estimate vapor pressure easily. antoine coefficients relate vapor pressure to temperature for almost 700 major organic compounds. *Hydrocarbon Processing*, 68(10), 65-8.
- Ye, S., Sleep, Brent E, & Chien, C. (2009). The impact of methanogenesis on flow and transport in coarse sand. *Journal of contaminant hydrology*, *103*(1-2), 48-57. Elsevier. doi:10.1016/j.jconhyd.2008.09.004

## APPENDIX A. PEER REVIEWED PUBLICATIONS FROM THIS WORK

- Johnson, R. L., Tratnyek, P.G., & Johnson, R. O. (2008). Persulfate persistence under thermal activation conditions. *Environmental science & technology*, 42(24), 9350–9356. ACS Publications.
- Krol, M. M., Sleep, B. E., & Johnson, R. L. (2011). Impact of low-temperature electrical resistance heating on subsurface flow and transport. *Water Resources Research*, 47(5). doi:10.1029/2010WR009675
- Krol, M.M., Mumford, K.G., Johnson, R. L., & Sleep, B.E. (2011). Modeling discrete gas bubble formation and mobilization during subsurface heating of contaminated zones. *Advances in Water Resources*, *34*(4), 537-549. Elsevier. doi:10.1016/j.advwatres.2011.01.010.
- Waldemer, Rachel H, Tratnyek, P.G., Johnson, R. L., & Nurmi, J. T. (2007). Oxidation of chlorinated ethenes by heat-activated persulfate: kinetics and products. *Environmental science & technology*, 41(3), 1010-5.